5-2008

Fundamental Deformation Micromechanics in a Zircaloy-4 Alloy and the Hydrogen Effects on its Microstructure, Internal Stresses, and Fatigue Behavior

Elena Garlea
University of Tennessee - Knoxville

To the Graduate Council:

I am submitting herewith a dissertation written by Elena Garlea entitled "Fundamental Deformation Micromechanics in a Zircaloy-4 Alloy and the Hydrogen Effects on its Microstructure, Internal Stresses, and Fatigue Behavior." I have examined the final electronic copy of this dissertation for form and content and recommend that it be accepted in partial fulfillment of the requirements for the degree of Doctor of Philosophy, with a major in Materials Science and Engineering.

Hahn Choo, Major Professor

We have read this dissertation and recommend its acceptance:

Peter K. Liaw, Yanfei Gao, David C. Joy

Accepted for the Council:
Dixie L. Thompson

Vice Provost and Dean of the Graduate School

(Original signatures are on file with official student records.)

To the Graduate Council:

I am submitting herewith a thesis written by Elena Garlea entitled "Fundamental Deformation Micromechanics in a Zircaloy-4 Alloy and the Hydrogen Effects on its Microstructure, Internal Stresses, and Fatigue Behavior". I have examined the final electronic copy of this dissertation for the form and content and recommend that it be accepted in partial fulfillment of the requirements for the degree of Doctor of Philosophy, with a major in Material Science and Engineering.

_____

Hahn Choo
Major Professor

We have read this dissertation and recommend its acceptance:

_____

Peter K. Liaw

_____

Yanfei Gao

_____

David C. Joy

Accepted for the Council:

_____

Carolyn R. Hodges, Vice Provost and
Dean of the Graduate School

(Original signatures are on file with official student records.)

Fundamental Deformation Micromechanics in a Zircaloy-4 Alloy and the Hydrogen Effects on its Microstructure, Internal Stresses, and Fatigue Behavior

A Dissertation Presented for the
Doctoral of Philosophy Degree
The University of Tennessee, Knoxville
Adviser: Prof. Hahn Choo

Elena Garlea
May 2008

Dedication

I dedicate this Doctoral dissertation to my husband Ovidiu, for his unconditional love, support, and encouragement, which helped me reach this goal. I am also dedicating this accomplishment to Didi, for all the joy and great time brought during the stressful times. This is also dedicated to my family, especially my mother for her love and support.

Acknowledgement

I would like to thank all those who helped me complete the Doctoral degree in Materials Science and Engineering.

I am grateful to my advisor Prof. Choo and co-advisor Prof. Liaw, for their guidance and efforts to make me familiar with the concepts of Neutron Diffraction, Mechanical Behavior, and Hydrogen Charging. I greatly appreciate their generosity on offering me opportunities to develop as young scientist. I am thankful to Drs. Gao and Joy, who kindly agreed to be on my dissertation committee.

I would also like to thank Dr. Hubbard of the Oak Ridge National Laboratory for his assistance on the NRSF 2 instrument, and for his valuable ideas through the research process. I am appreciative to Drs. Clausen and Brown of the Los Alamos National Laboratory, for sharing with me their worldwide-recognized expertise on neutron diffraction for strain measurement and theoretical modeling. The things that I learned during our collaboration are invaluable to me.

I would like to extend my thanks to Dr. Rack and his group, and Dr. G. Y. Wang for the help with samples preparation. Many thanks to my colleagues and friends at UT: Zhenzhen Yu, Tim Wilson, Julia Sun, Chuck Woo, Migri Stoica, Matt Freels, E-Wen Huang, and Michael Benson.

Special thanks to Andrei Savici for the help with editing this dissertation.

I would like to acknowledge the National Science Foundation (NSF) International Materials Institutes (IMI) Program (DMR-0231320), managed by Dr. C. Huber and Tennessee Advanced Materials Laboratory (TAML) Fellowship Program, with Prof. W.

Plummer as the Program Director for financial support. Most of this work has benefited from the use of the Lujan Neutron Scattering Center at Los Alamos Neutron Science Center (LANSCE), which is funded by the Office of Basic Energy Sciences at Department of Energy (DOE). Los Alamos National Laboratory is operated by Los Alamos National Security LLC under DOE Contract DE AC52 06NA25396. This work also benefited from the use of High Temperature Materials Laboratory (HTML) User Program, Oak Ridge National Laboratory (ORNL), sponsored by the Assistant Secretary for Energy Efficiency and Renewable Energy, Office of FreedomCAR and Vehicle Technologies. Some of the research had been conducted at High Flux Isotope Reactor (HFIR) at ORNL through Ames Laboratory. HFIR is supported by the DOE's Office of Basic Energy Sciences Materials Sciences Division (DE-AC05-000R22725) with UT-Battelle, LLC. User Program Ames Laboratory is operated by Iowa State University for the U.S. DOE, under Contract No. W-7405- ENG-82.

Lastly, I would like to thank my family and friends, whose suggestions and encouragement made this work possible.

Abstract

Zircaloy-4 alloys, polycrystalline zirconium alloys, are extensively used in the nuclear industry. During the service in the reactor, these alloys absorb hydrogen, leading to formation of zirconium hydrides, which may be enhanced by the stress field around a crack tip. In order to investigate these phenomena in a Zircaloy-4 alloy, the effect of internal stresses on the hydride precipitation and the subsequent influence on the fatigue behavior has been studied.

Firstly, the deformation systems responsible for the polycrystalline plasticity at the grain level, in a hexagonal-close-packed, coarse-grained, and random-textured Zircaloy-4 alloy are considered. The evolution of internal strains was measured in-situ, using neutron diffraction, during uniaxial tensile loading up to 7% strain. The macroscopic stress-strain curve and the intergranular (hkil-specific) strain development, parallel and perpendicular to the loading direction, are measured. Then, a new elasto-plastic self-consistent (EPSC) modeling scheme is employed to simulate the experimental results. The model shows a good agreement with the measured data.

Secondly, the hydride phase formation and its influence on fatigue crack growth in Zircaloy-4 alloy are investigated. The microstructure and fatigue behavior of the Zircaloy alloy in the as-received condition is shown. Then, the formation and distribution of hydride phase in the alloy, and its effect on microstructure and the fatigue crack propagation rates is discussed. The residual lattice strain profile ahead of a fatigue crack has been also measured using neutron diffraction. The combined effect of residual strain

and hydride precipitation on the fatigue behavior is presented and discussed. In addition, the zirconium lattice strains evolution under applied loads of 900, 1,800, and 2,700 N in the presence of hydrides is studied, and compared with the as-received condition.

Finally, we report the experimental results from neutron incoherent scattering and neutron radiography studies on hydrogen charged Zircaloy-4 specimens.

Future work is planned to study the kinetics of hydride formation under applied load, using neutron diffraction and in-situ hydrogen charging.

Table of Contents

List of Tables

List of Figures

List of Figures (Continued)

List of Figures (Continued)

List of Figures (Continued)

List of Figures (Continued)

List of Figures (Continued)

List of Figures (Continued)

List of Figures (Continued)

List of Figures (Continued)

List of Figures (Continued)

List of Figures (Continued)

List of Figures (Continued)

List of Figures (Continued)

List of Figures (Continued)

List of Figures (Continued)

List of Figures (Continued)

List of Figures (Continued)

List of Figures (Continued)

List of Figures (Continued)

CHAPTER 1

INTRODUCTION

1. INTRODUCTION

1.1 Zirconium Alloys in Nuclear Reactor

Zirconium alloys were developed for use as nuclear fuel cladding (among other nuclear reactor components) in the early 1950s [1]. Zirconium was chosen for use in the cores of water-cooled nuclear reactors because of its low thermal neutron capture cross-section, reasonable mechanical properties, and adequate corrosion resistance in high-temperature water. It was initially thought that the poor corrosion resistance of some batches of unalloyed zirconium was a result of random impurities. However, it was found that improving the purity did not eliminate these problems [1]. The oxidation rate of zirconium was found to vary considerably with grain orientation during the growth of thin, interference-colored, oxide films [2]. This problem was solved by the addition of transition metals (Cr and either, Fe or Ni) that are insoluble in the zirconium matrix and appeared as small particles of intermetallic phases; and Sn, which is soluble in zirconium [3-5]. The main advantage of the alloying additions appeared to be the development of a more uniform protective thick oxide film, and the new alloys were named Zircaloy-2 (Ni-alloy) and Zircaloy-4 (Fe-alloy) [5]. Zircaloy–4 (Zr-4) alloys are currently used in the development of new cladding tubes for Pressurized Water Reactors (PWRs), due to the zirconium's high transparency to thermal neutrons, coupled with excellent corrosion resistance and good mechanical properties. On the other hand, zirconium-based cladding alloys absorb hydrogen during their service in a nuclear-reactor environment leading to formation of zirconium hydrides. As a result, hydride formation becomes one of the main degradation sources of zirconium alloys in nuclear-reactor environments.

Therefore, the main reason for choosing Zr-4 alloy for the current research was that this alloy serves as a model material system for the study of hydrogen embrittlement through the hydride formation. Furthermore, Zr-4 was selected for this study because: (1) the material permits deep penetration for neutron diffraction; (2) material has significant structural applications; and (3) some fundamental material properties are available.

1.2 Neutron Diffraction as a Main Tool for Strain Measurements and Hydrogen Distribution Studies

The deep penetration capability of neutrons into most metallic materials makes neutron diffraction a unique and powerful tool for the studies of their structures and properties [6]. In particular, spatially-resolved neutron-diffraction study of internal strains is based on the volume-averaged measurement of interplanar spacings (*d*-spacings) in various crystallographic and geometric orientations. A drawing of a neutron diffraction experimental setup is shown in Fig. 1.1*. One measures the *d*-spacing of a crystalline material, based on the Bragg's law: $\lambda = 2d\sin\theta$, where λ is the wavelength, d is the interplanar spacing (d-spacing), and 2θ is the angle between the incident and diffracted beam. The lattice strain, ε, is defined as the relative change of the d-spacing from its stress-free state:

$$\varepsilon = (d - d_o) / d_o \qquad (1.1)$$

where d is the distance between diffracting planes under stress, and d_o is the stress-free spacing.

*All figures are in Appendix

Thus, the lattice strain can be measured using the expansion or contraction of the lattice of a material in a particular orientation.

Furthermore, neutron diffraction measures the incoherent scattering given by the hydrogen (H) present in the material's bulk. The large incoherent cross-section of H (σ_H^{incoh} = 79.9 barn) compared to that of zirconium (σ_{Zr}^{incoh} = 0.02 barn) [10] gives rise to a significant and uniform increase in background of the diffraction spectra. By measuring the changes in the background signal, which is proportional to the H content, even small concentrations of H (e.g., 2-5 μg/g) can be analyzed [11-14]. In addition, the neutron tomography can be a powerful nondestructive imaging technique useful for hydrogen distribution studies, taking advantages of the significant difference in the total cross sections of Zr σ_{scatt} = 6.46 barn and H σ_{scatt} = 82.06 barn [10], which gives different effect on the beam attenuation, and thus creating an imaging contrast. Therefore, the neutron scattering measurements, combined with detailed numerical analyses, could enable a non-destructive estimation of the hydrogen (and hydride) distributions within the bulk of engineering materials and components.

Finally, in-situ neutron diffraction studies, under applied mechanical loading, allowed us to investigate the evolution of internal strains and texture. Although it is not part of this dissertation, it is feasible to study the hydride formation in Zr-4 by in-situ neutron diffraction.

1.3 Motivation of the Research, Scientific Issues, Tasks, and Expected Results

Studies of the interactions between fuel cladding materials and coolants (e.g. zirconium alloys and water) have provided some insight to zirconium embrittlement

phenomena. For example, when a free surface of Zircaloy-4 is immersed in water under pressurized water reactor conditions (high temperature, high steam pressure), two layers of oxides are formed, namely the α- and β-zirconia. Advancement of the oxidation layer is accompanied by the penetration of hydrogen in the first metal layers, followed by the nucleation and precipitation of zirconium hydrides, which embrittle the material [15]. In addition to the presence of hydrides and oxides, another factor that affects cladding failure is the stress state associated with in-service loading, which increases the severity of the hydrogen embrittlement [16]. The redistribution of stresses in the material, accompanied by irradiation and changes in temperature, leads to subsequent changes in bulk physical and mechanical properties. Figure 1.2 shows the microstructure formed during in-reactor operation of a Zircaloy-4 cladding tube, irradiated to 67 GWd/t, which exhibits a solid hydride layer with a depth of ~ 50 μm under a thick oxide layer, as well as the presence of a concentration of discrete, circumferential hydride precipitates [17].

Over the years, several theories have been developed regarding the mechanisms of the formation of metal hydrides. The critical issues include the diffusion of H to high-stress regions, nucleation and growth of hydride in such regions, reorientation of hydrides under external stress, and subsequently the fracture of hydrides. For example, under a cyclic loading condition, the crack propagates rapidly through the hydrides that can lead to crack growth and catastrophic failure of the nuclear component [18-21].

In this dissertation work, two main issues are investigated: (a) the deformation mechanisms of the polycrystalline Zr-4 and (b) the formation and distribution hydrides in Zr-4 alloy and their influence on the fatigue behavior.

First, we ask which are the fundamental mechanisms responsible for the plastic deformation in the hcp polycrystalline Zr-4? Materials with hcp crystal structures are prone to develop intergranular strains as they can exhibit highly anisotropic properties at the grain level. Typically, coefficients of thermal expansion, in any hcp polycrystal, are different in the *c* and *a* directions, resulting in development of thermal intergranular stresses upon cooling from the processing temperatures. Moreover, the multitude of slip systems, combined sometimes with twinning, causes considerable plastic anisotropy, which generates intergranular stresses during plastic deformation. The elastic response from each family of grains is measured directly, using neutron diffraction, while the plastic strain component is investigated via theoretical models. The theoretical simulations, which consider the thermal and elastic-plastic mechanical anisotropy of the polycrystal, are known as the elasto-plastic self-consistent models. In this study, the micromechanical plastic deformation mechanisms of the as-received Zr-4 are investigated using both in-situ neutron diffraction mechanical testing and a self-consistent deformation-modeling scheme.

Next, we are interested in what the mechanism of hydride formation in zircaloy alloys is and what the subsequent effect on the fatigue behavior is. What is the role played by residual strains at a crack tip on hydride formation? What is the lattice strain evolution in the presence of hydrides under the applied load? Zirconium alloys suffer from hydrogen embrittlement due to the presence of zirconium hydrides, which form from the dissolved hydrogen during the service in the nuclear reactor. The nature and locations of zirconium hydride precipitates is associated with the alloy microstructure and processing history. Hydrogen embrittlement is a complex mechanism that can cause

changes in the bulk physical and mechanical properties, such as diminution of ductility, decrease of fracture toughness, and shortening of the fatigue life. Moreover, understanding the crack propagation behavior, and the H intake, requires knowledge of residual stresses near the crack tip, associated with the prior plastic deformation. Zirconium hydrides could precipitate preferentially at existing crack tips, due to the high stress concentration field, leading to a brittle failure. At the lattice level, under applied load and in the presence of hydrides, the anisotropic Zr is expected to exhibit a redistribution of stresses. Thus, neutron diffraction studies of the zirconium lattice strains around a fatigue crack, when hydrides precipitates exist, can help understand the effect of hydrides on zirconium lattice dilation and on the crack propagation under cyclic loading condition.

Consequently, the key scientific issues and the defined tasks addressed in this dissertation are schematically presented in Fig. 1.3. Several experimental tools and techniques were employed such as: optical microscopy with polarized light, SEM, x-ray diffraction, neutron incoherent scattering, and neutron imaging for the microstructure analyses and phase formation identification. In addition, neutron diffraction technique was used for spatially-resolved measurements of the internal strain within the bulk of the material and around the fatigue cracks. Experimental data was analyzed using peak refinement analysis and self-consistent modeling.

The expected results from this dissertation and scientific impacts are also presented in Fig. 1.3

REFERENCES

1. B. Lustman, J. of Nucl. Mater., 100 (1981): pp. 72-77.

2. R. A. Ploc, J. Nucl. Mater., 28 (1968): pp. 48-60.

3. S. Kass, J. Electrochem. Soc., 107 (7) (1960): pp. 594-597.

4. B. Cox and H. I. Sheikh, J. of Nucl. Mater., 249 (1997): pp. 17-32.

5. B. Cox, J. of Nucl. Mater., 336 (2005): pp. 331-368.

6. H. J. Stone, P. J. Withers, T. M. Holden, S. M. Roberts, R. C. Reed, Metall Mater. Trans. A, 30 (7) (1999): pp. 1797-1808.

7. X-L Wang, C. M. Hoffman, C. H. Heueh, G. Sarma, C. R. Hubbard, J. R. Keiser, Appl. Phys. Let., 75 (21) (1999): pp. 32943296.

8. H. Choo, M. A. M. Bourke, M. R. Daymond, Composites Sci. Tech. 61 (12) (2001): pp. 1757-1772.

9. J. W. L. Pang, T. M. Holden, T. E. Mason, Acta Mater 46 (5) (1998): pp. 1503-1518.

10. A. D. Krawitz, "*Introduction to Diffraction in Materials Science and Engineering"*, (2001): pp. 389.

11. Y. N. Choi, H. S. Oh, V. T. Em, V. A. Somenkov, C.-H. Lee, and S. D. Park, Appl. Phys. A, 74 (2002): pp. 1710-1712.

12. F. Couvreur and G. Andre, "*In-Situ Neutron Scattering Study of Hydrogen-Containing Zircaloy-4 Alloys",* in LLB Scientific Report (1997-1998): pp.723

13. V. V. Kvardakov, H. H. Chen-Mayer, and D.F. R. Mildner, J. Appl. Phys., 83, 7 (1998): pp. 3876-3879.

14. E. Garlea, V. O. Garlea, H. Choo, C. R. Hubbard, and P. K. Liaw, Mat. Sci. Forum, vols. 539-543 (2007) pp. 1443-1448.

15. G. Lelievre, D. Fruchart, P. Convert, and F. Lefevre-Joud, J. All. Comp. 347 (2002): pp. 288–294.

16. F. Yunchang and D.A. Koss, Metall. Trans. A 16A (4) (1985): pp. 675- 681.

17. O.N. Pierron, D.A. Koss, A.T. Motta, K.S. Chan, J. Nucl. Mater. 322 (2003): pp. 21–35.

18. J. Lufrano, P. Sofronis, and H. K. Birnbaum, J. Mech. Phys. Solids, 46 (1998): pp. 1497-1520.

19. M. L. Grossbeck and H. K. Birnbaum, Acta Metall., 25 (1977): pp.135-147.

20. S. Sagat, S. Q. Shi, and M. P. Puls, Mater. Sci. and Eng. A, 176 (1994): pp. 237-247.

21. R. Dutton, K. Nuttall, M. P. Puls, and L. A. Simpson, Metal. Trans. A, 8A (1977): pp. 1553 - 1562.

APPENDIX

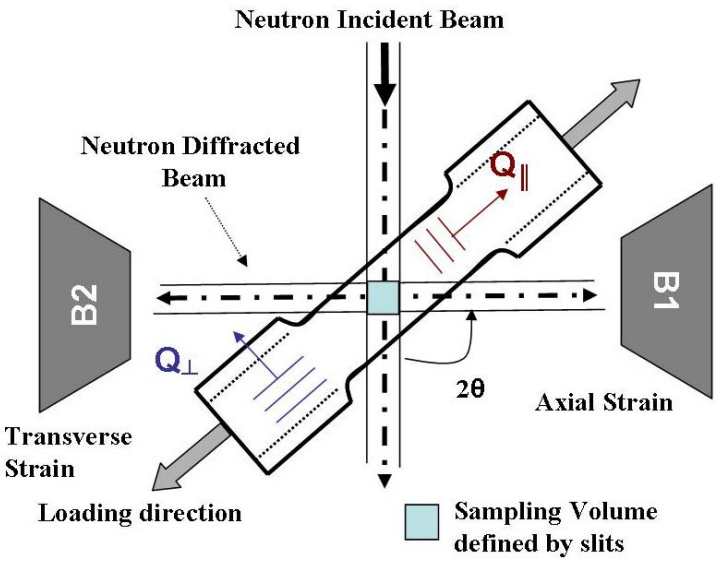

Figure 1.1 Schematic representation of the strain measurement by neutron diffraction in two different directions: axial (in-plane) and transverse (through-thickness) of specimen.

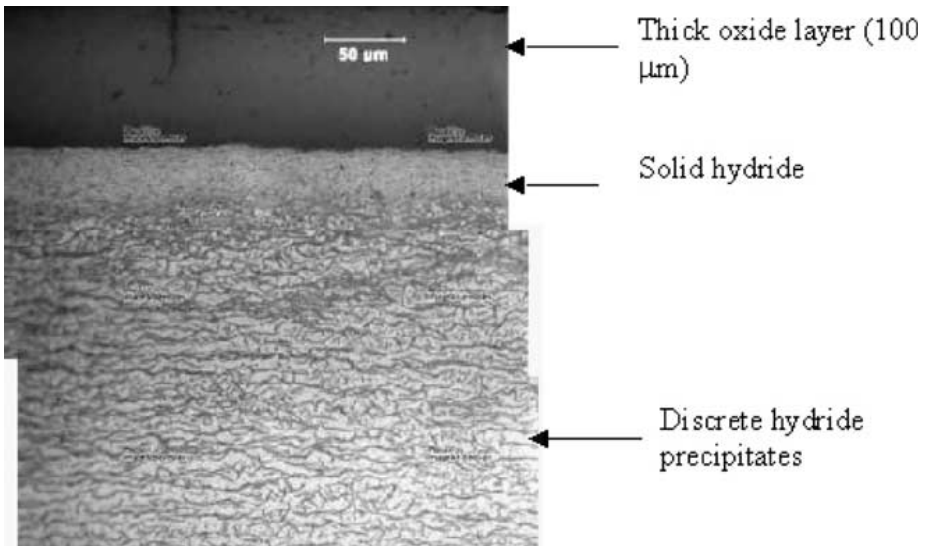

Figure 1.2 A light micrograph showing a hydride layer and associated hydrides in the substrate beneath the layer in irradiated Zircaloy-4 cladding [17].

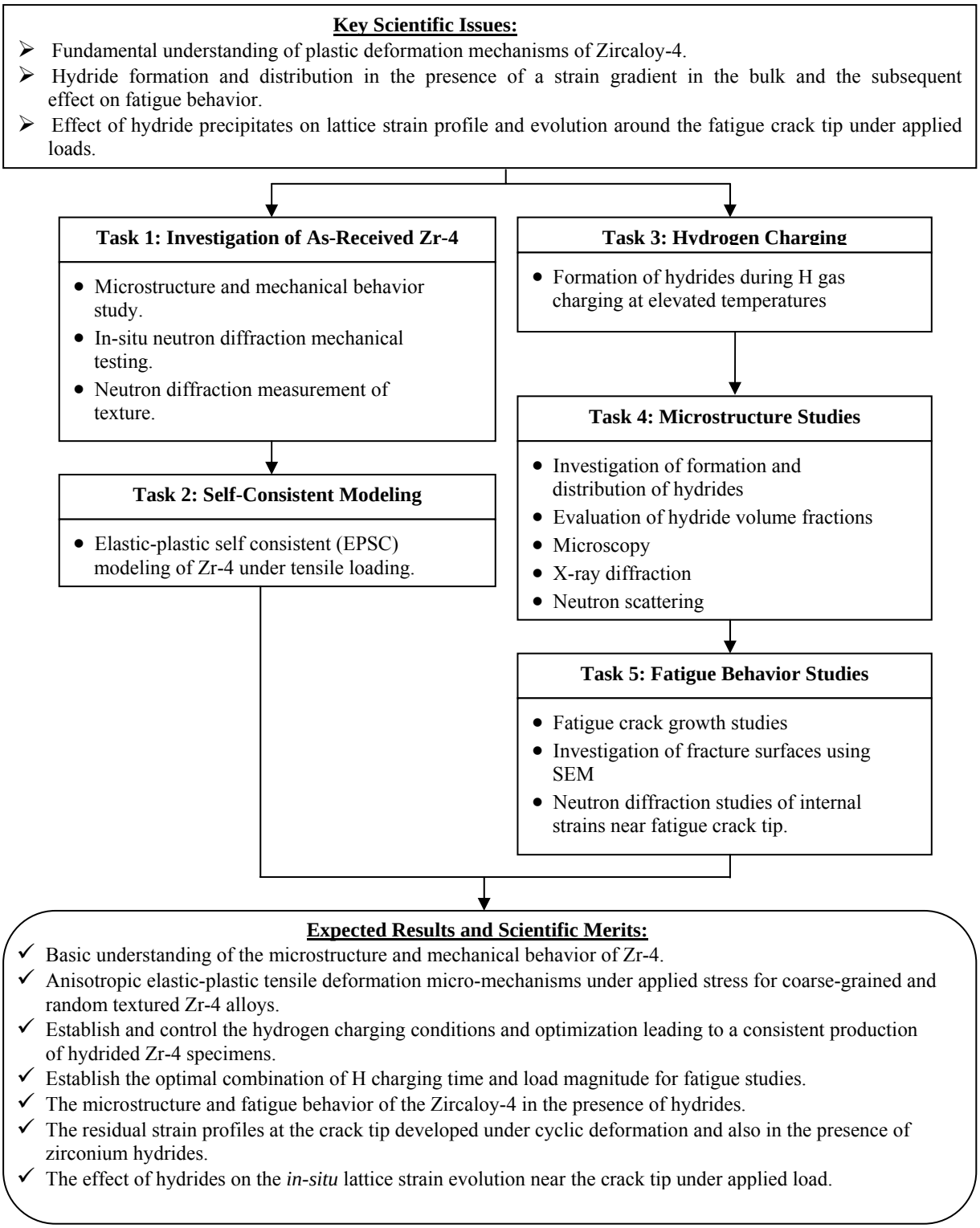

Figure 1.3 Scientific issues, defined tasks, and expected results of the current dissertation.

CHAPTER 2

LITERATURE REVIEW

2. LITERATURE REVIEW

Abstract

This chapter summarizes critical issues related to the internal strains evolution under applied stress, and the effect of hydrogen on mechanical-behavior of zirconium alloys. It starts with a general overview of the neutron scattering techniques employed to study the lattice strains and the texture, the hydrogen incoherent scattering, and the radiography/tomography imaging of hydrogen in the bulk. Then, the plastic deformation systems in hcp metals and the self-consistent modeling schemes used to simulate these mechanisms are reviewed. Finally, the effects of hydrogen and hydrides on mechanical properties of Zr-alloys under the nuclear reactor conditions are summarized.

2.1 Overview of Neutron Scattering Technique

2.1.1 Neutron diffraction measurement of strain

Neutron diffraction is a powerful tool that allows the non-destructive determination of internal strains in crystalline materials. Positions of the neutron scattering peaks are given by the interplanar distances within the grains contributing to diffraction. Linear shifts of the peaks are direct measures of the elastic strains in the structural component to be studied [1, 2]. The plastic deformation manifests itself by non-linearity in the elastic strain development with the applied load.

The diffraction methods for stress studies use the measurement of lattice spacing, d, for the (hkl) plane of the crystal via Bragg's law,

$$\lambda = 2d\sin\theta \tag{2.1}$$

where λ is the known neutron wavelength and 2θ is the angle of diffraction. The elastic strain, ε, is given by the equation:

$$\varepsilon = (d - d_0) / d_0 \tag{2.2}$$

where d_0 is an appropriate stress-free lattice spacing [1]. An example of such measurement, carried out on a ferritic steel sample, is shown in Fig. 2.1(a) in the form of lattice strain versus the applied load [1]. The lattice strain for the (110) and (002) reflections of the body centered cubic (bcc) structure are shown. The appropriate diffraction elastic constants can be obtained from the slop of the lines in the figure. One can also investigate the lattice parameter and the subsequent strain evolution by using the equation:

$$\varepsilon = (a - a_0) / a_0 \tag{2.3}$$

where a_0 is an appropriate stress-free lattice constant. Fig. 2.1(b) shows the evolution of lattice parameter *a* for six different <10.1> directions in the basal plane as a function of temperature for a Zircaloy-2 alloy highly textured. From the results, one can observe that the thermal residual strains, developed during processing, disappear as the temperature increases.

2.1.2 Neutron diffraction measurement of texture

Diffraction is a well-suited technique to characterize the crystallographic orientation of the constituent grains, thus the texture. Texture usually develops via two mechanisms, namely deformation texture and annealing texture. The deformation texture forms due to the plastic deformation, which leads to an anisotropic arrangement of the

grain orientations in the polycrystal. When a textured material is plastically deforming, the grains are prone to rotate in such a way as to maximize the shear on the slip planes. Annealing texture forms from the nucleation and growth of the grains and phases. The combination of the thermal treatment and cold-work processes produces the recrystallization of stress-free grains. However, the planes with the lowest surface energy tend to grow first which leads to the formation of preferred orientation. Additionally, the formation of a second phase occur only in particular crystallographic orientations relative to the primary phase [2].

Neutron diffraction can be used to study the orientation of the grains. If there are preferred orientations for the grains, i.e. texture, the peak intensity, measured by diffraction, will directly reflect this by showing higher or lower peak intensity with respect to a random texture. Whether the measured intensity is higher or lower than for a random texture depends on the specific hkl reflection and the orientation of the scattering vector with respect to the texture [2].

The characterization of texture is performed by recording the variation of the intensity of family of planes or poles. One can examine the intensity variation of one family of planes as a function of sample orientation, resulting in the full pole figure, or of several families of grains in a fixed sample orientation, resulting in the inverse pole figure [2]. Examples of the pole figures obtained on a commercial extruded magnesium plate are shown in Fig. 2.2. The figure shows typical rolling and extruded textures with two major texture components of the basal poles perpendicular to the plate normal (ND) and one parallel to the transverse direction (TD). Also the figure contains a scale, which indicates the relative direction intensity, where 1.0 means random [3].

2.1.3 Incoherent neutron scattering measurement of hydrogen

Due to the large incoherent cross-section of hydrogen, (i.e., σ_H^{incoh} = 80.27 barn while σ_{Zr}^{incoh} =0.02 barn) [4], a unique advantage of using neutron scattering techniques is the possibility to perform non-destructive measurements of the total hydrogen content in an alloy, and also to characterize the hydrides. The incoherent cross-section gives rise to a continuous background in diffraction spectra, which is proportional to the hydrogen content, and is (nearly) independent of scattering angle. (The coherent cross-section contributes significantly to the structure factor of the hydride phase, i.e. to the intensity of its diffraction peaks.) Thus, by measuring the change of the background signal due to incoherent scattering, one can analyze even a very small amount of hydrogen, 2-5 μg/g [5]. For example, Couvreur et al. [6] determined, non-destructively, the total amount of incorporated hydrogen with a very good sensitivity and precision (< 20 ppm weight), Fig. 2.3. The neutron-diffraction measurements were carried out in-situ, at various temperatures (between 20 and 500 °C), under secondary vacuum, on a section of Zr-4 cladding tube containing 642 ppm weight hydrogen (length of the sample: 50 mm, diameter: 9.5 mm). One observes the increase of background with the hydrogen content, and the weak diffraction lines of δ-ZrH_2 hydride and a Laves phase [6]. In addition to the total hydrogen content, it was possible to simultaneously obtain the hydrogen content in the hydride form, and the crystallographic characterization of the $Zr(Fe, Cr)_2$ and ZrH_2 precipitates, and the solubility of hydrogen. Information about the dissolution of hydrides, Fig. 2.4(a), and the influence of hydrogen on the thermal expansion of Zr-4, Fig. 2.4(b) was also obtained. Figure 2.4(a) shows the proportion of hydrogen content in

the hydride form (δ-phase) versus temperature for a sample containing 642 ppm weight hydrogen. This quantity decreases with increasing temperature. According to the phase diagram shown in the inset, dissolution of the hydrides is complete above 500 °C and the sample is a single-phase α-Zr-based alloy solid solution. Figure 2.4(b) shows the temperature dependence of the lattice parameter *a* of Zr-4 (sample containing 642 ppm weight hydrogen). A similar curve was found for the lattice parameter *c*. The increase of slope above 350°C was attributed to the dissolution of hydrides, which introduces interstitial hydrogen atoms in the α-Zircaloy matrix and a supplementary swelling. This explanation is confirmed by the observed decrease in lattice parameter during an isothermal annealing at 500°C due to hydrogen desorption out of the sample [6].

2.1.4 Neutron imaging of hydrogen

The use of neutron imaging is a powerful way to investigate the hydrogen presence and distribution in the bulk, without destruction of samples. This technique takes advantages of the significant differences in the total cross sections of Zr σ_{scatt} = 6.46 barn and H σ_{scatt} = 82.06 barn [4], which give different neutron beam attenuations, and thus creating an imaging contrast. A complete 3-D tomography image of the object's composition can be obtained by rotating the object 180 degrees, and taking neutron radiographs at defined angular positions. Using a 2-D neutron detector, the neutron radiographs are obtained as neutron shadows of objects placed in the beam. The image captured is a gray level image, where the gray level of each pixel (i, j) is proportional to the number of neutrons that made it through the object, which is determined from the attenuation law, known as Beer's Law:

$$I(i,j) = I_0(i,j) \exp(-\mu t) \quad (2.4)$$

The measured neutron intensity is related to the amount of scattering and absorption of neutrons, by the material in the beam, where μ is the attenuation length of the material. A large μ means that a material will strongly scatter or absorb neutrons. One can measure μ in a separate experiment and thus obtain the material thickness, t, in a pixel. The transmission image allows one to quantify the amount of material in the beam and to do numerical analysis with the images. By dividing the image, during operation, by a reference image (the beam without the sample), one arrives at the transmission image [7].

2.2 Overview of Internal Strains in Materials with Hexagonal-Close-Packed Structure

2.2.1 Generalities

Typically, the internal stresses can be grouped into three different categories, depending of the length scale over which they vary, namely: Type I (macrostresses), Type II, and Type III (both microstresses) [8]. Type I stress with the length scale l_{0I}, Fig. 2.5, is comparable to the macroscopic dimension of the structure. These stresses are a consequence of macroscopic plastic deformations, and are assumed continuous from grain to grain, and even from phase to phase. Type II stresses, with length scale l_{0II}, Fig 2.6, are comparable in size to the grain, usually a few tens of microns. Type II stresses can be different from grain to grain and are also known as intergranular stresses. Type III stresses, with the length scale l_{0III}, Fig 2.6, are smaller than the characteristic size of the grain. These stresses could vary within a specific grain, as in the case of crystal defects.

When measured using neutron diffraction, type II and III stresses generally give rise to diffraction peaks broadening [8].

2.2.2 Internal strains in zirconium alloy

Zircaloy-4 alloys are extensively used in the nuclear industry because of the high-performance in severe pressure and temperature conditions, coupled with high transparency to thermal neutrons. Zircaloy-4 (Zr-4) alloys are polycrystalline zirconium (Zr) alloys, with hexagonal-close-packed (hcp) crystalline structure at room temperature. Low symmetry materials, like hcp structures, are prone to develop intergranular strains, as they can exhibit highly anisotropic properties at the grain level. Typically, in any hcp polycrystal, coefficients of thermal expansion (CTE) are different in the <c> direction compared to the <a> or <b> direction, resulting in development of thermal intergranular stresses upon cooling during processing. Moreover, the multitude of slip and twinning systems causes considerable plastic anisotropy, which generates intergranular stresses during plastic deformation [8, 9].

Further, for hcp materials, the polycrystal plasticity depends on the c/a ratio, which orders the active deformation modes. The c/a ratio varies from metal to metal and can be smaller or larger than the ideal sphere packing (c/a = 1.633). When c/a is above normal (e.g. Cd, Zn), the basal slip is more favorable to be activated, while for c/a below normal (e.g. Mg), prism slip system along the <a> direction is most favorable, followed by basal slip [10]. For Zr alloys with c/a = 1.593 the prism slip along the <a> direction is the most dominant slip system. Deformation with <c> components has been explained by first or second-order pyramidal slip in <c+a> direction and/or twinning on the first and

second-order pyramidal planes [8-11]. Figure 2.8 shows schematic of the possible deformation system, in particular the $(10\bar{1}0) < 1\bar{2}0 >$ prism slip, $(10\bar{1}2) < 10\bar{1}1 >$ tensile twinning, $(10\bar{1}1) < 10\bar{1}2 >$ compressive twinning, $(11\bar{2}2) < 11\bar{2}3 >$ pyramidal slip <c+a>, and $(0001) < 11\bar{2}0 >$ basal slip. The activity of these deformation systems depends mostly on the combined effect of temperature, stress level, and bulk texture. Additionally, slips on the basal plane were observed at temperatures of 577 ºC (850 K) [12] or 400 ºC [13], when its activity was associated with an increase in the impurities of the alloy, in particular oxygen and nitrogen content. On the other hand, the models used to simulate deformation in Zr-2 alloys at room temperature, showed improvement in agreement with the experiments, when the activity from the basal slip was considered [14, 15]. Pyramidal <a> was reported to be sometimes possible and its activity increases with temperature [16].

Slip and twinning often occur simultaneously, and their interaction is very complicated and less investigated for zirconium alloys. Therefore, a combination of experimental and theoretical methods needs to be employed in attempting to understand the alloy polycrystalline plasticity, and its implication for the material performance.

The theoretical simulations that consider the thermal and elastic-plastic mechanical anisotropy of the polycrystal are known as the elasto-plastic self-consistent models. Turner and Tomé [17] have developed an elasto-plastic self-consistent (EPSC) model based on a modeling scheme implemented by Hutchinson for face-centered- cubic (fcc) non-textured polycrystals [18]. This model, which accounts for the elastic-plastic grain-to-grain interaction, was first used to predict the internal stresses in Zircaloy-2 (Zr-

2) with rod texture. In addition, the thermal dilatation effects were included in the code with the scope of predicting the measured thermal residual strains in Zr-2, reported in Ref. [19]. It was experimentally shown that while Zr single crystals are stress free during cooling or heating in a temperature range of 300-900 K, the polycrystalline alloys can develop thermal residual strains of the order of 100 MPa due the anisotropic thermal coefficients of the a- and c-axes [19]. Figure 2.9 shows the measured and predicted thermal residual strains for the prism and basal planes, as a function of the temperature for the Zr-2 alloy with rod texture [17]. Both planes are perpendicular to the rod axis. The experimental data in this figure, reported first in Ref. [19], was measured by neutron diffraction on a sample annealed at 923 K and cooled in steps of 50 K from 900 to 300 K. The theoretical data was obtained using the self-consistent model considering the stress-free temperature of 998 K [17]. The model was in good agreement with the measured basal and prism thermal residual strains. Further, the thermo-mechanical scheme was employed to predict the response during uniaxial tension and compression tests of the Zr-2 rod [17]. Figure 2.10(a) shows the experimental stress–strain curves for the annealed Zr-2 rod, deformed in uniaxial tension and compression along the rod axis. From the experimental curves, the yield stress of 200 MPa in tension and 325 MPa in compression were found, while the Young modulus was 95 GPa. The calculated profiles for the tension and compression tests are presented in Figures 2.10(b-c), predicting the yield stress of 195 MPa in tension, Fig. 2.10(b), 320 MPa in compression, Fig. 2.10(c), and a Young modulus of 96.8 GPa, close to the experiment. The good agreement indicates as active systems the prism slip, <c+a> pyramidal slip, and twinning, which however, was treated as a regular slip system. Also in the Figs. 2.10(b-c) the AVACS are shown as a

function of the deformation, to provide extra information about the role played by the microstructure in the macroscopic response of the bulk. This represents the AVerage number of ACtive Systems in each orientation (10 total used to represent the texture), weighted by the volume fraction associated with the orientation. For example, in Fig. 2.10(b), AVACS are equal to 2 between 0.3% and 1.75% strain, which means that the plastic deformation is accommodated only by the prism slip. Beyond 1.75 % strain, the AVACS increase to 3.25 suggesting that the pyramidal slip is also participating to the deformation. For the prediction of the compression test, Fig. 2.10(c), the onset of plastic deformation was through prism slip, similar with the tensile profile. However, the elasto-plastic transition is shortened by the activation of twining, at about 0.3 % strain and 350 MPa. The achieved accord, and in particular the absence of the "plateau" observed for the compressive experiment, was explained by the fact that the model accounts only for the contribution of twins to the plastic deformation, and does not include the stress relaxation associated with twinning [17].

Next, the same self-consistent modeling scheme, with the magnitude of critical resolved shear stress (CRSS) for prismatic system modified, was applied to predict the effect of internal stresses and texture in rolled Zr-2 under tensile and compressive mechanical loading, at room temperature, up to 2% strain [20]. Figures 2.11(a) and (b) show the measured and predicted stress-strain curves for tension and compression deformation along the rolling direction, respectively. The simulation reproduced the features of the experimental stress-strain curve and it was concluded that the mechanical response is strongly dependent on the residual stresses and the texture of the material.

Specifically, the texture influences the plastic anisotropy, while the internal stresses play an essential role on the yield stress and on the elasto-plastic transition [20].

Later, a similar EPSC scheme was employed to predict the intergranular stresses from the measured intergranular strains in Zr-2 with rod texture [14]. Two similar specimens were used, and the strains parallel and perpendicular to the rod axis were measured using neutron diffraction. The average total strain response of the two samples was plotted as a function of the applied load, for the experiment and the model, Fig. 2.12. The simulated macroscopic stress-strain curve showed an improved agreement after the basal slip was added to the active prism and pyramidal slip systems. Additionally, the corresponding values for CRSS and hardening coefficients reported in Ref [17] were changed. Further, the model was used to predict the elastic lattice strain evolution. However, due to the alloy's rod texture, only a few Zr reflections were obtained during the neutron diffraction experiment. For example, Fig. 2.13 shows the Zr (0004) and Zr $(20\bar{2}0)$ lattice strain response in the transverse direction, as a function of the applied stress. The calculation exhibited a good agreement with the measured linear elastic behavior [14]. Moreover, using the formula $\sigma_i = c_{ij}\varepsilon_j$, the stress states of the grains in the sample were calculated. The c_{ij} are the elastic constants for the Zr single crystal, and ε_{11}, ε_{33}, and ε_{13} are obtained from the experiment while the ε_{12} and ε_{23} were assumed to be zero. The uncertainties of the components of the stress tensor are on the order of 20 MPa. Figure 2.14 represents the principal lattice stress components σ_{11}, σ_{22}, and σ_{33}, relative to the applied stress. With the employed EPSC scheme, the evolution of lattice stresses σ_{11}, σ_{22}, and σ_{33} as the applied load increases was calculated and it is shown in Fig. 2.15. The prediction was consistent with the measurements within the experimental errors [14].

More recently, Clausen et al. [21] has developed a new EPSC modeling scheme that was validated on a magnesium alloy. The novelty of this new code is the account for the effect of twinning and texture development under applied load. Nominally, it considers the twin activation, twin reorientation, and specific stress relaxation associated with twinning. The in-situ measurements of internal stress evolution during compression test along the rod axis are presented in Figs. 2.16(a) and (b), for the longitudinal and transverse directions, respectively. Both the neutron diffraction data and the simulation are shown in the figure. The profiles showed a highly non-linear response, with signs of stress inversion in some orientations, which was correlated with twinning. Further, the texture measured and predicted by the model due to twinning at 0%, 5%, and 10% total strain for the basal and prism planes are shown in Fig. 2.17. The model considered the creation and growth of new twin grains with strain, while the parent grain's volume fraction concomitantly decreases. This, in turn, allowed the correct prediction of the evolution of yield stress, texture, and twin volume fraction with strain. However, the model assumptions were not able to accurately predict the lattice strains for the prism planes in the transverse direction. This was explained by the lack of direct interaction between the parent and twin grains subsequent to twin formation.

The latest model scheme will be used for this study, and it is further discussed in the following chapters.

2.3 Overview of Hydrogen Effects on Mechanical Behavior

2.3.1 Generalities

Hydrogen can react with metallic alloys in detrimental of the mechanical properties. Hydrogen diffuses with a high mobility in most metals, occupying the interstitial site. In the case of bcc metals, the activation energies for hydrogen diffusion are typically on the order of 1-5 kcal/mol [22, 23]. For fcc and hcp metals the mobility of hydrogen is less than in bcc metals and the activation energies are on the order of 5-15 kcal/mol. This is because of the larger interstices and close packing of the host atoms. Additionally, during the diffusion process in the metal, H can encounter an interaction with defects, leading to H trapping, which can significantly lower the effective diffusivity at lower temperatures [24, 25].

The interaction of hydrogen with defect-traps is universally observed in metal-hydrogen systems [24, 26], and even the relatively weak interactions can have significant effect on material properties at lower temperatures [27]. The hydrogen dissolved in the crystal lattice produces effects generally classified as hydrogen embrittlement. The major form of hydrogen embrittlement is hydrogen-induced cracking (HIC) of various high-strength alloys (ferrous and nonferrous), under sustained tensile loads, in the presence of hydrogen or hydrogen-bearing environments. Hydrogen embrittlement is a complex phenomenon, and it is believed that there is more than one mechanism responsible for it [28]. To explain the hydrogen-related failure many theories have been proposed [29-35]. One of the most recognized mechanism was the hydrogen-enhanced localized plasticity (HELP) mechanism, and theoretical and experimental evidence were provided [30, 31].

The evidence of plasticity on hydrogen-induced fracture surfaces has been a common observation for many years [32-34]. Generally, this plasticity was dismissed as an occurrence during, or following, hydrogen embrittlement, rather than a cause of it. This trend may be attributed in part to the resolution at which the fracture surfaces were examined. At low resolutions, the effects of the localization of the ductility to regions of high hydrogen concentration would not be discernible, giving fracture surfaces a brittle appearance. Based on detailed fractography study of hydrogen-embrittled steels, Beachem [34] was the first to propose that the failure occurred by ductile processes and that hydrogen enhanced and not retarded the mobility of dislocations. The Beachem's mechanism was further considered. Using a transmission electron microscope equipped with an environmental cell, a direct observation of the dislocation-velocity enhancement due to hydrogen by deforming materials in-situ was conducted [30]. The experimental observations, combined with numerical/analytical results, provided the explanation for the hydrogen-enhanced localized plasticity mechanism of hydrogen embritlement [31].

On the other hand, in the case of hydride-forming materials, (e.g. some of the transitional metals), the mechanisms responsible for H embrittlement are different. They relate to the diffusion of hydrogen to high-stress region, nucleation and growth of hydride in such region, reorientation of hydrides under external stress, and, subsequently, the fracture of hydrides. Under a cyclic loading, the crack propagates through the hydrides, which can lead to a fast crack growth and catastrophic failure of the structural component [35-38]. The metals form hydrides with the absorbed hydrogen, which can be supplied by an environment that contains or generates hydrogen. This trend can take place during the production, processing, and/or the service of the metal.

2.3.2 Hydride formation in Zircaloy alloys and its effect on mechanical behavior

Many transitional metals (including zirconium) and their alloys react with hydrogen at elevated temperatures, to form metallic hydrides. Zirconium, titanium, and hafnium (the metals in Group IV B in the Periodic Table of the Elements), possess α-hcp crystal structures at room temperature, which transform to bcc β–allotropic modifications at 882 °C, 870 °C, and 782 °C, respectively. The zirconium-hydrogen phase diagram [39] is shown in Fig. 2.18. The β-solid solution decomposes into an α-solid solution in equilibrium with the δ-hydride, ZrH_{2-x} at the eutectoid temperature of 550 ˚C (823 K). As more hydrogen is absorbed, a first-order phase transition transforms the fluorite δ-hydride to the body-centered-tetragonal ε-hydride (ZrH_2). At room temperature and above, there are three known crystallographic phases of zirconium hydride [40]: a face-centered tetragonal gamma (γ) phase, a face-centered cubic delta (δ) phase, and another face-centered tetragonal epsilon (ε) phase. It is worth noting that the stable hydride phase at room temperature is the delta phase [41]. Further, the hydride phase is less dense (hydride density = 5600 kg x m^{-3}) than the matrix it replaces (zirconium density = 6511 kg x m^{-3}) producing a volume dilation of approximately 17 %, which needs to be accommodated by the matrix [41]. It was suggested that due to the anisotropic properties of zirconium, as δ-ZrH_2 is crystallography isotropic with an fcc structure, the volumetric misfit accompanying the precipitation of hydrides is also anisotropic [42]. In addition, because the habit plane for hydrides is close to the basal plane or within 20 degrees of (0001) [41], the anisotropic misfit causes the highest strain to be along any directions normal to (0001).

Zirconium alloys are used extensively in the nuclear industry. During service in a nuclear reactor, these alloys undergo a series of simultaneous processes, including the redistribution of stresses, irradiation, changes in temperature, hydrogen diffusion, and precipitation of hydrides, which can lead to hydride-induced embrittlement [35-38, 43]. Hydrogen embrittlement in Zr-alloy can produce changes in the bulk physical and mechanical properties, such as reduction of ductility, decrease of fracture toughness, and shortening of the fatigue life [35-38, 43]. For example, studies of fracture toughness of a Zr-4 commercial alloy showed that temperature, hydrogen content, and hydrides orientation play an essential role [44]. It was observed that hydrogen charging in a temperature range of 293–473 K produced the formation of δ-hydride platelet precipitates, oriented in planes parallel to the rolling direction. When hydrides were normal to the crack path, higher toughness values and fracture mechanisms with more plastic deformation were obtained than for the case of hydrides parallel to it.

A specific issue of the hydrogen embrittlement, that occurs mostly during the reactor shutdowns, is the crack propagation [45]. It was observed, during the Pickering pressure tube cracking experience [45], that the cracking was induced by high residual stresses in the inner wall of the cladding tube, which attracted the hydrogen present in the tubes. Subsequently, at some defect sites, when the stress intensity factor (K) was high enough, the crack initiation occurred. The crack propagation manifested by the fracture of the hydride precipitates aligned perpendicular to the tensile stress. It was emphasized that at operational coolant temperatures, the hydrogen was in a solid solution and the crack could not extend. However, below this temperature, the precipitation of hydrides occurred at the crack tip, followed by the growth of the crack. It was concluded that the

time to failure increases with decreasing the stress intensity factor range (ΔK). This indicates that there is a certain value for the stress intensity factor, above which the crack velocity appears independent of it, also known as the stage II crack growth. At lower values of ΔK, or stage I, the crack velocity decreases rapidly with decreasing the stress intensity factor, suggesting the existence of a stress intensity threshold for the crack to initiate. At temperatures between 350 K and 420 K, the stress intensity threshold was found to be about 5 MPa√m [45] or 6 MPa√m independent of temperature [41]. The crack initiation is controlled by a critical combination of hydrogen concentration and stress level, which need to compensate for each other [46]. This is similar with Le Chatelier's principle [47], which states that if a dynamic equilibrium is disturbed by a change in the conditions, the position of equilibrium moves to reduce the change. Furthermore, ref. [38] reports on the fatigue behavior of Zr-2.5% Nb in the presence of zirconium hydrides. Figuree 2.19(a-d) shows the crack velocity (m/s) as a function of the stress intensity factor range (MPa√m) at different temperatures. The stage II crack growth exhibits negative stress dependence while velocity decreases [38]. Similar behavior was observed on steel [48]. However, a different result was reported later on Zr-4 [49]. Figure 2.20(a-c) displays the crack velocity (m/s) as a function of the stress intensity factor range (MPa√m), at three different temperatures and hydrides concentrations. It shows that during region II, the crack velocity increases with ΔK, and the trend is enhanced by the increase in temperature. An increase in the hydrides concentration shortens the stage II and decreases the critical stress intensity factor. Stage III crack growth occurs at high ΔK values, when crack becomes unstable, and the fracture toughness is approached, causing catastrophic failure. This stage is not well understood, however, because the

crack propagates very fast, it is believed that it is not strongly affected by the environment [50].

Furthermore, the formation of hydrides could induce the stress relaxation and plastic strain enhancement in the region in front of the crack-tip. It was observed in Nb alloys that, in the presence of hydrides, a 23 % reduction in the peak normal stress in front of the crack tip occurred [35]. Hence, the precipitated hydrides may mechanically influence the crack tip stress in addition to the material degradation, which results from the hydride's extremely brittle nature.

Moreover, understanding the crack propagation behavior also requires knowledge of residual stress near the crack. In the case of fatigue cyclic loaded specimens, these residual stresses develop in the material when the load is released. During unloading, crack faces can reach a premature contact in the awake of the crack, leading to plastic deformations [51, 52]. Plastic deformation can influence the crack-propagation rate. In general, tensile residual stresses enhance crack propagation and reduce fracture toughness, whereas compressive stresses have an opposite effect [53]. It was suggested that the leaking from the pressurized tube at the Pickering reactor was due to the high tensile residual stresses induced by improper rolling, whereas a theoretical model showed that the compressive residual stresses could have accepted very high hydrogen content without damaging the part’s properties [45].

The knowledge on the nature of pre-existing residual stresses near the crack tip, their effect on H diffusion, and hydride formation and distribution can help predict crack growth behavior in hydrogen-rich environments. The residual stresses at the crack tip regions can be directly measured by neutron diffraction, which provides an excellent non-

destructive technique to measure the elastic lattice strain response to external factors (e.g. stresses and environments) [8, 51, 52].

REFERENCES

1. T. M. Holden, J. H. Root, R. A. Holt, and M. Hayashi, Physica B, 213&214, (1995): pp. 793-796.

2. A. D. Krawitz, "*Introduction to Diffraction in Materials Science and Engineering"*, (2001).

3. L. Wu, A. Jain, D. W. Brown, G. M. Stoica, S. R. Agnew, B. Clausen, D. E. Fielden, and P. K. Liaw, Acta Mater. 56 (2008): pp. 688-695.

4. Insitute Laue-Langevin, Neutron Data Booklet, 2nd Ed.

5. Y. N. Choi, H. S. Oh, V. T. Em, V. A. Somenkov, C.-H. Lee, and S. D. Park, Appl. Phys. A, 74 (2002): pp. 1710-1712.

6. F. Couvreur and G. Andre, "*In-Situ Neutron Scattering Study of Hydrogen-Containing Zircaloy-4 Alloy*", in LLB Scientific Report (1997-1998): pp.723.

7. http://physics.nist.gov/MajResFac/NIF/radiography.html

8. M. T. Hutchings, P. J. Withers, T. M. Holden, and T. Lorentzen, *"Introduction to the Characterization of Residual Stress by Neutron Diffraction"*, (2005).

9. U. F. Knock, C.N. Tomé, and H. –R. Wenk, "*Texture and Anisotropy, Preferred Orientations in Polycrystals and their Effect on Materials Properties*", (1998).

10. E. Tenckhoff, "*Deformation Mechanisms, Texture, and Anisotropy in Zirconium and Zircaloy*", (1988).

11. E. Tenckhoff, Metall. Trans. A, 9A, (1978): pp. 1401-1412.

12. A. Akhatar, Acta Metall., 21, (1973): pp. 1-11.

13. J. E. Bailey, J. of Nucl. Mater., 7, no. 3 (1962): pp. 300-310.

14. J. W. L. Pang, T. M. Holden, P. A. Turner, and T. E. Mason, Acta Mater., 47, no. 2 (1999): pp. 373-383.

15. F. Xu, R.A. Holt, and M.R. Daymond, J. of Nucl. Mater. 373 (2008): pp. 217–225

16. G. Monnet, B. Devincre, L. P. Kubin, Acta Mater., 52 (2004): pp. 4317-4328.

17. P. A. Turner and C. N. Tomé, Acta Metall. Mater. 42, no. 12 (1994): pp. 4143-4153.

18. J. W. Hutchinson, Proc. R. Soc. Lond. A 319, (1970): pp. 247-272.

19. S. R. MacEwen, C. N. Tomé, and J. Faber, Acta Metall., 37, (1989): pp. 979-989.

20. P. A. Turner, N. Christodoulou, and C. N. Tomé, Inter. J. of Plast., 11, no. 3 (1995): pp. 251-265.

21. B. Clausen, C. N. Tomé, D. W. Brown, and S. R. Agnew, "*Reorientation and Stress Relaxation due to Twinning: Modeling and Experimental Characterization for Mg* ", Submitted to Acta Mater, (2007).

22. C. A. Wert, J. Phys. Chem Solids, 31 (1970): pp. 1771.

23. H. K. Birnbaum and C. A. Wert, In Proc. Internat. Meeting "*Hydrogen In Metals*". Julich, Jul-Conf-6, II (1972): pp. 626.

24. E. E. Fletcher and A. R. Elsa, *"Hydrogen Movement in Steel-Entry, Diffusion, and Elimination".* DMIC Report, Battele Memorial Institute, Columbus, OH, 219 (1965).

25. W. R. Heller, Acta Met., 9 (1961): pp. 600.

26. R. A. Oriani, "Hydrogen in Metals". (1967): pp. 32.

27. R. Gibala, Proc. Internat. Symp. "*Stress Corrosion Cracking and Hydrogen Embrittlement of Iron Base Alloys*", France, (1973): pp. 244-245.

28. H. K. Birnbaum, I. M. Robertson, P. Sofronis, and D.Teter, *"Proceedings of the Conference on Corrosion Deformation Interactions"*. Edited by T. Magnin (London: Institute of Materials), Nice, France (1997): pp. 172-195.

29. J. P. Hirth, Met. Trans. A, 11 (1980): pp. 861.

30. D. S. Shih, I. M. Robertson, and H. K. Birnbaum, Acta metal., 36, (1) (1988): pp. 111-124.

31. H. K. Birnbaum and P. Sofronis, Mater. Sci. and Eng. A 176 (1994): pp. 191-202.

32. R. A. Oriani and P. H. Josephic, Acta Met., 22, (1974): pp. 1065.

33. R. A. Oriani and P. H. Josephic, Acta Met., 25 (1977): pp. 979.

34. C. D. Beachem, Metall. Trans. A, 3 (1972): pp. 437.

35. J. Lufrano, P. Sofronis, and H. K. Birnbaum, J. Mech. Phys. Solids, 46 (1998): pp. 1497 1520.

36. L. A. Simpson and M. P. Puls, Met. Trans. A, 10 A (1979): pp. 1093-1105.

37. S. Sagat, S. Q. Shi, and M. P. Puls, Mater. Sci. and Eng. A, 176 (1994): pp. 237-247.

38. R. Dutton, K. Nuttall, M. P. Puls, and L. A. Simpson, Metal. Trans. A, 8A (1977): pp. 1553 - 1562.

39. K. G. Barraclough and C. J. Beevers, J. of Nucl. Mater., 33 (1969): pp. 296-301.

40. K. G. Barraclough and C. J. Beevers, J. of Mater. Science, 4 (1969): pp. 518-525.

41. M. P. Puls, Acta Metall., 1981. 29: pp. 1961 - 1968.

42. G. J. Carpenter, J. of Nucl. Mater., 1973. 48: pp. 264 - 266

43. C. E. Ells, J. of Nucl. Mater., 28 (1968): pp. 129-151

44. G. Bertolino, G. Meyer, and J. P. Ipina, J. of Nucl. Mater., 322 (2003): pp. 57-65.

45. E. C. W. Perryman, J. of the British Nuclear Energy Society 17, (2) (1978): pp. 95-105.

46. R. Troiano, Transactions of the ASM, vol. 52 (1960): pp. 54-80.

47. D. R. Gaskell, *"Introduction to the thermodynamics of Materials"*, 3rd Edition (1995).

48. W. W. Gerberich, Y. T. Chen, and C. StJohn, Metal. Trans. A, 6, (8) (1975): pp: 1485 -1498.

49. J. -H. Huang and C. -S Ho, Materials Chemistry and Physics, 47 (1997): pp. 184-192.

50. S. Suresh, "Fatigue of Materials", 2nd Edition, (1998).

51. Y. Sun, H. Choo, P. K. Liaw, Y. Lu, B. Yang, D. W. Brown, and M. A. M. Bourke, Scripta Mater., 53 (2005): pp. 971-975.

52. T. M. Holden, J. H. Root, R. A. Holt, and P. A. Turner, J. of Nucl. Mater., 304 (2002): pp. 73-82.

53. J. D. Almer, J. B. Cohen, and R. A. Winholtz, Metal. and Mater. Trans. A, 29A (1998): pp. 2127-2136.

APPENDIX

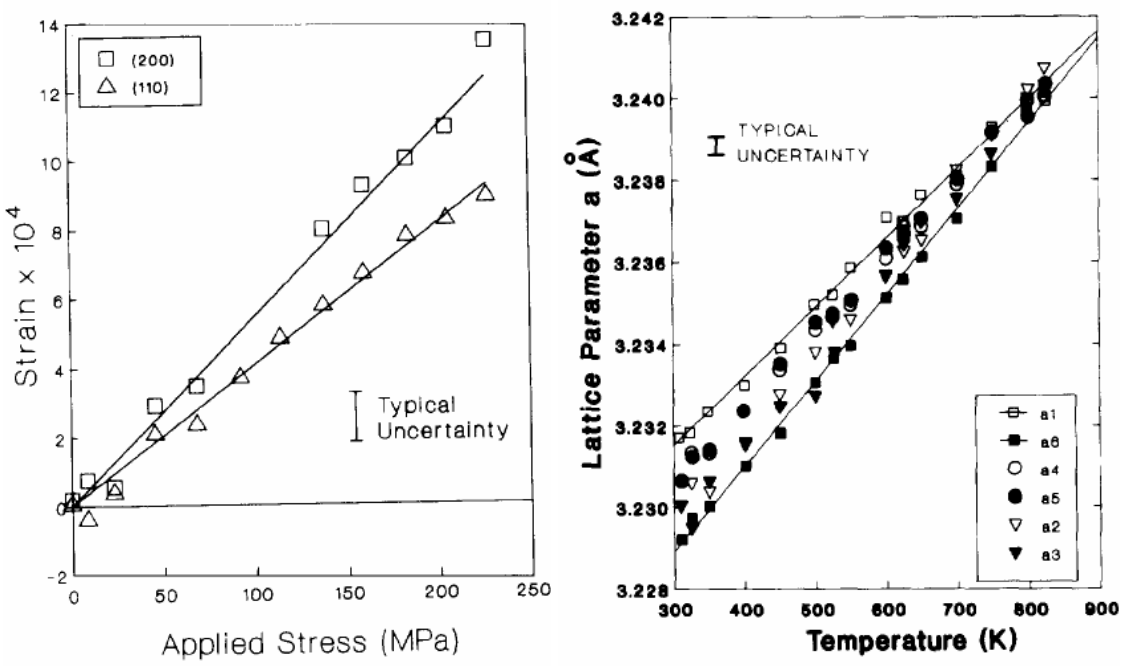

(a) (b)

Figure 2.1 Examples of neutron diffraction results from reference [1]: (a) lattice strain versus applied stress in ferritic steel for both the (110) and (002) reflections of the BCC structure. The appropriate diffraction elastic constants can be obtained from the slopes of the lines. (b) The lattice parameter *a* for six different <10.1> directions in the basal plane of a highly textured HCP Zircaloy-2 sample as a function of temperature.

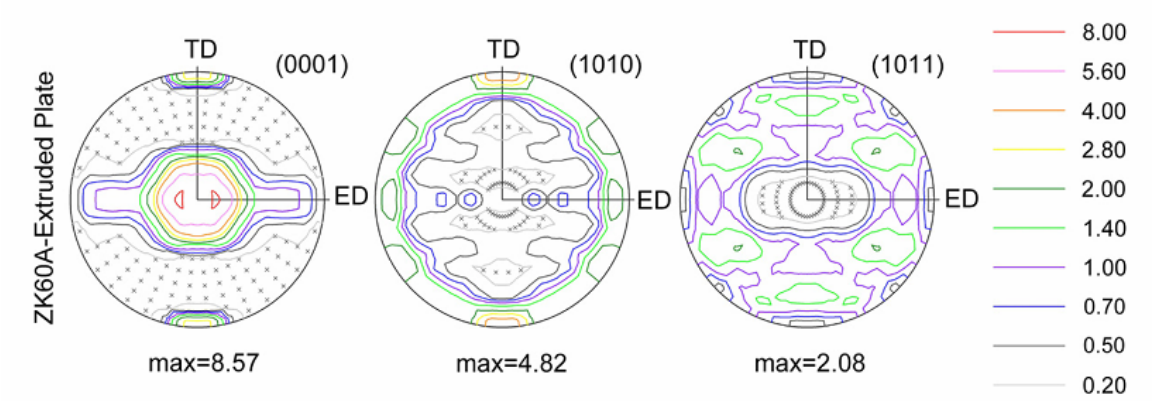

Figure 2.2 Initial texture of a commercial extruded magnesium plate. The scale at right indicates the relative direction intensity (1.0 = random). It shows the typical rolling and extruded textures with two major texture components of the basal poles perpendicular to the plate normal (ND) and one parallel to the transverse direction (TD). ED = extrusion direction [3].

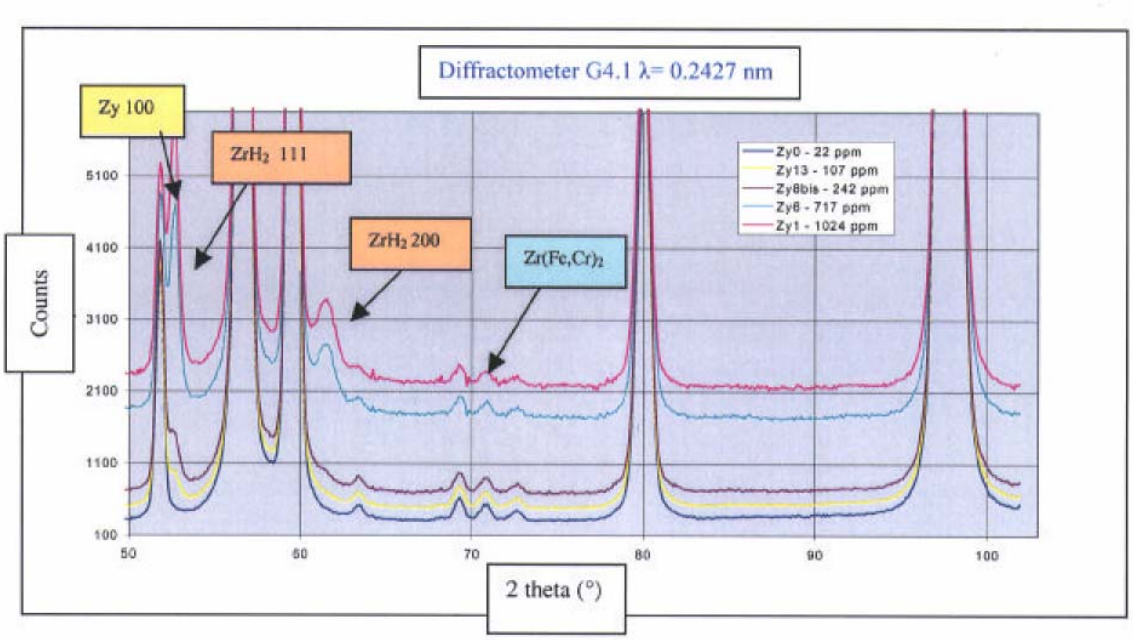

Figure 2.3 Powder diffraction diagrams measured for several Zircaloy samples [6].

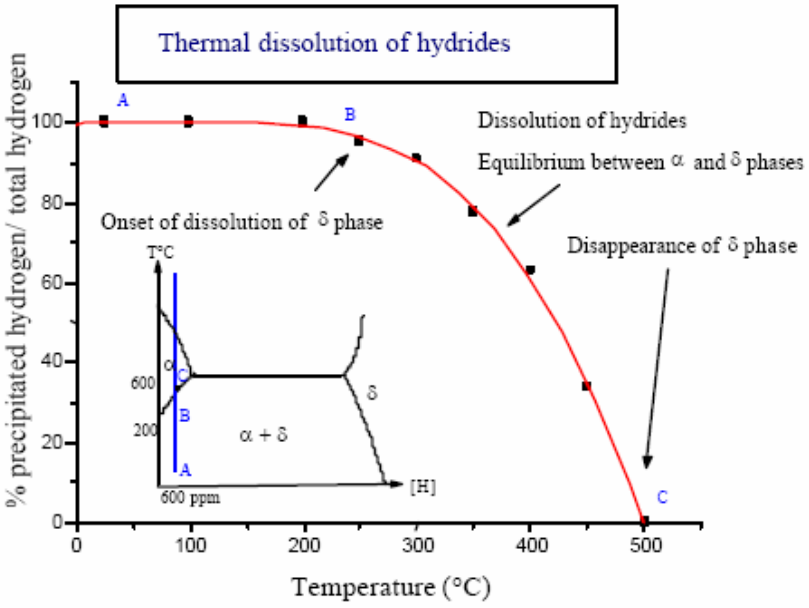

(a)

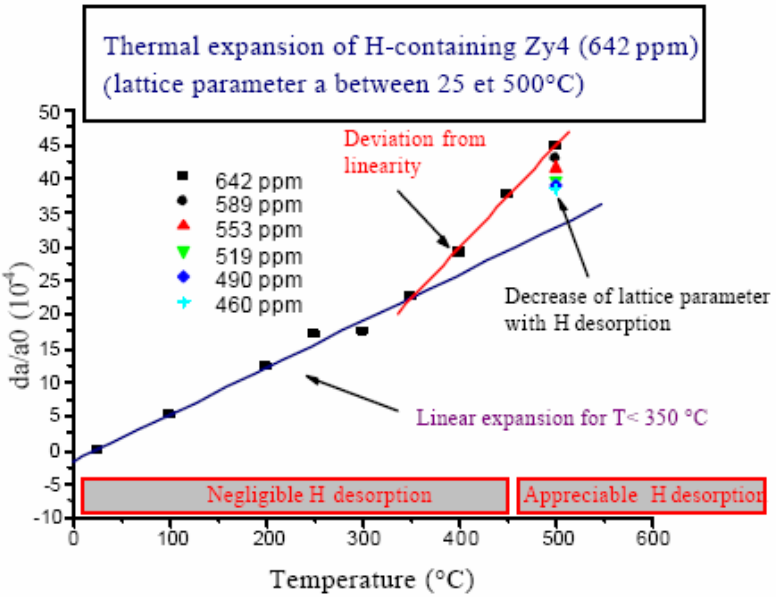

(b)

Figure 2.4 Hydrogen effect on a Zircaloy-4 alloy (a) proportion of hydrogen content in hydride form (δ-phase) versus temperature for a sample containing 642 ppm weight hydrogen. (b) Temperature dependence of the lattice parameter *a* of the Zr-4 (sample containing 642 ppm weight hydrogen) [6].

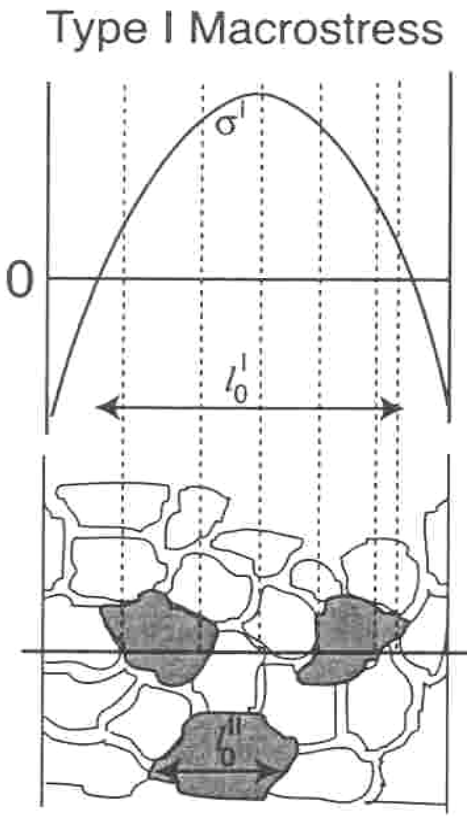

Figure 2.5 Type I stress varies on a length scale l_{0I}, which is considered continuous across grains [8].

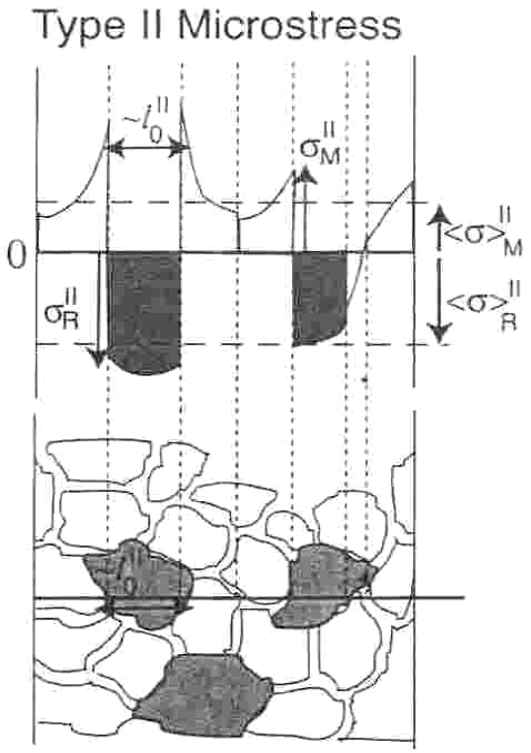

Figure 2.6 Type II stress varies on a length scale l_{0II}, which is on the order of the grain size [8].

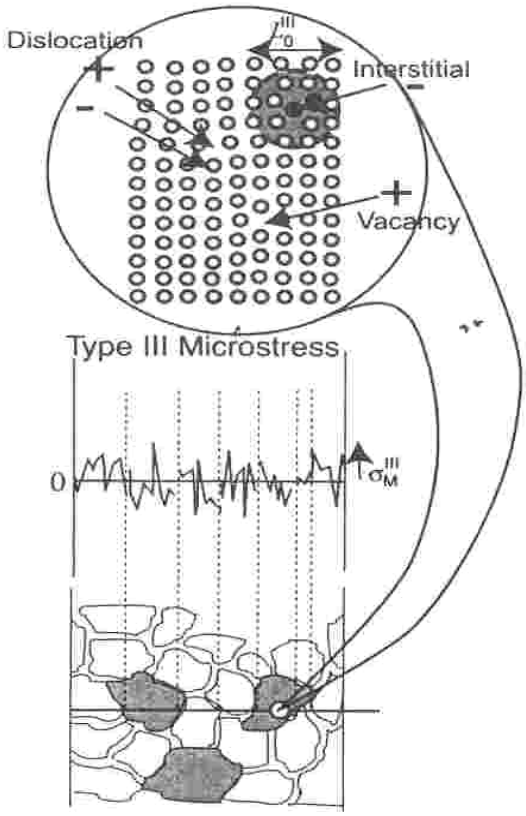

Figure 2.7 Type III stress varies on a subgrain scale l_{0III}, which is smaller than the grain size [8].

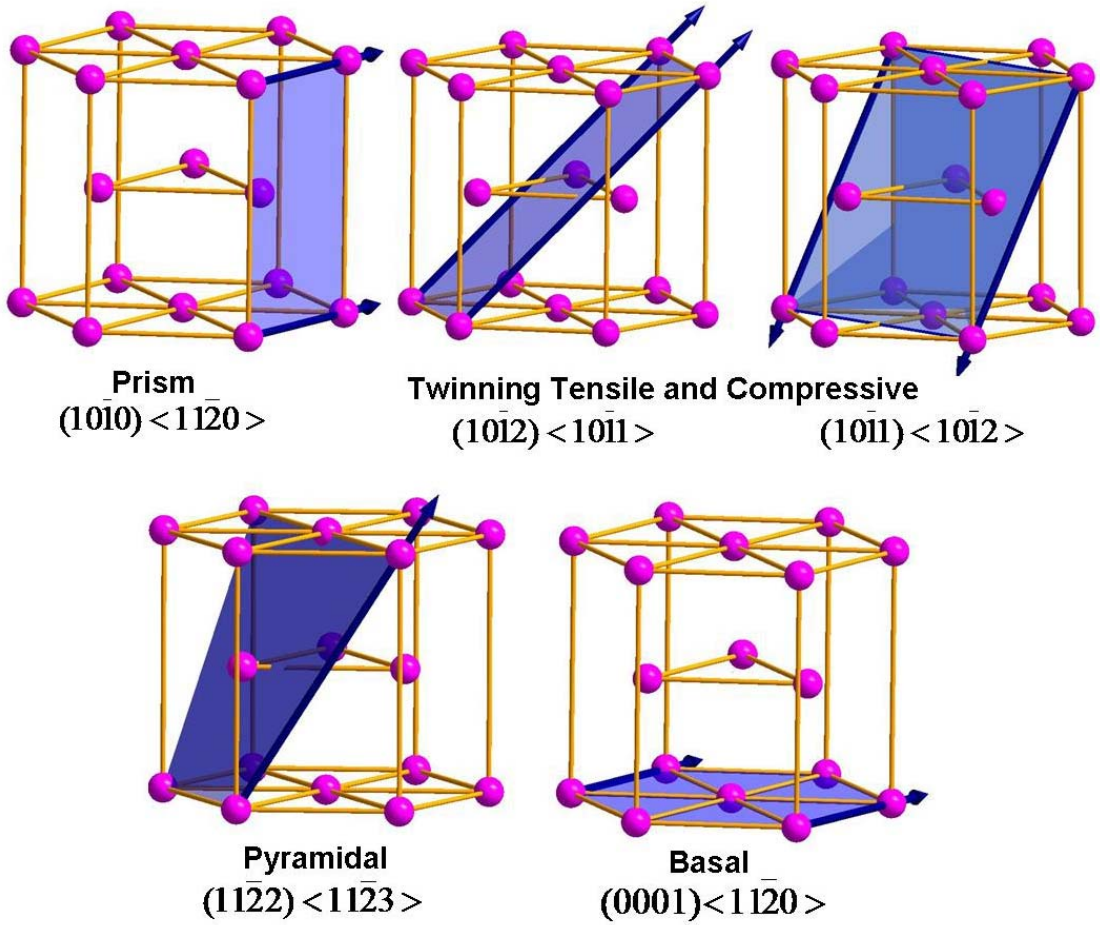

Figure 2.8 Schematic of the possible deformation systems in Zirconium alloys.

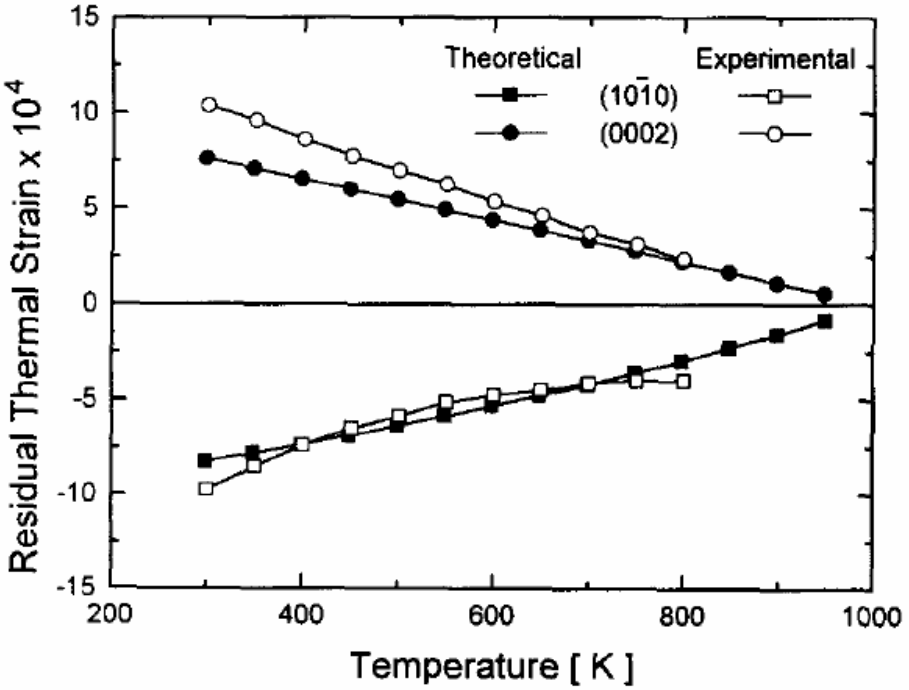

Figure 2.9 Thermal residual strains in prism and basal planes as a function of the temperature for a Zircaloy- 2 alloy with rod texture [17]. The basal and prism planes are perpendicular to the road axis. The experimental data was obtained by neutron diffraction on the sample annealed at 923 K and cooled in steps of 50 K from 900 to 300 K [19]. The theoretical data was obtained using a self-consistent model, which considered the stress-free temperature of 998 K [17].

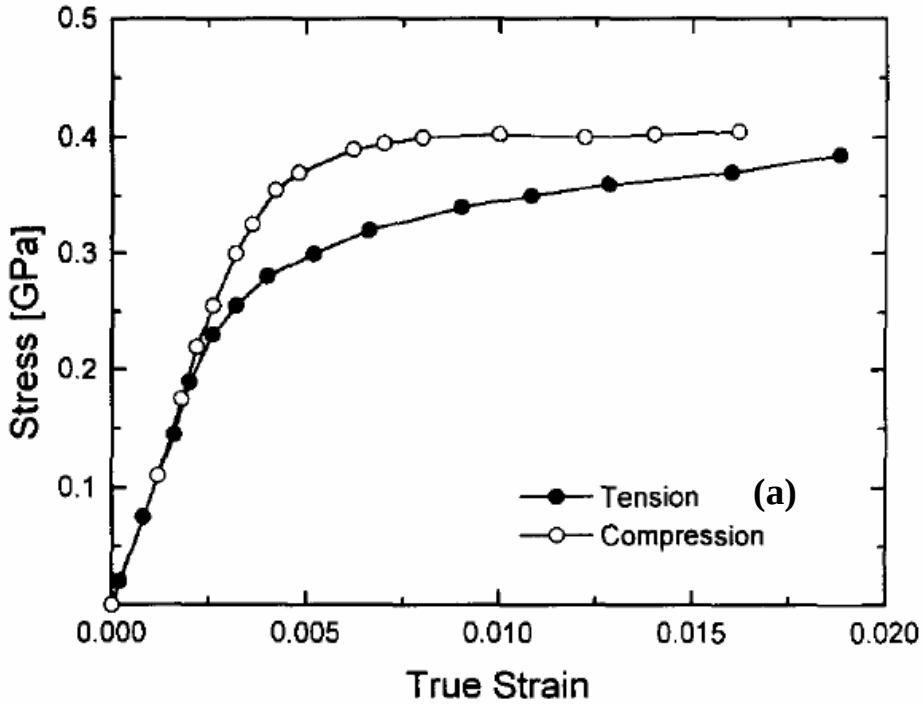

Figure 2.10 A Zircaloy-2 alloy with rod texture. (a) Measured stress-strain curves for tension and compression tests [17].

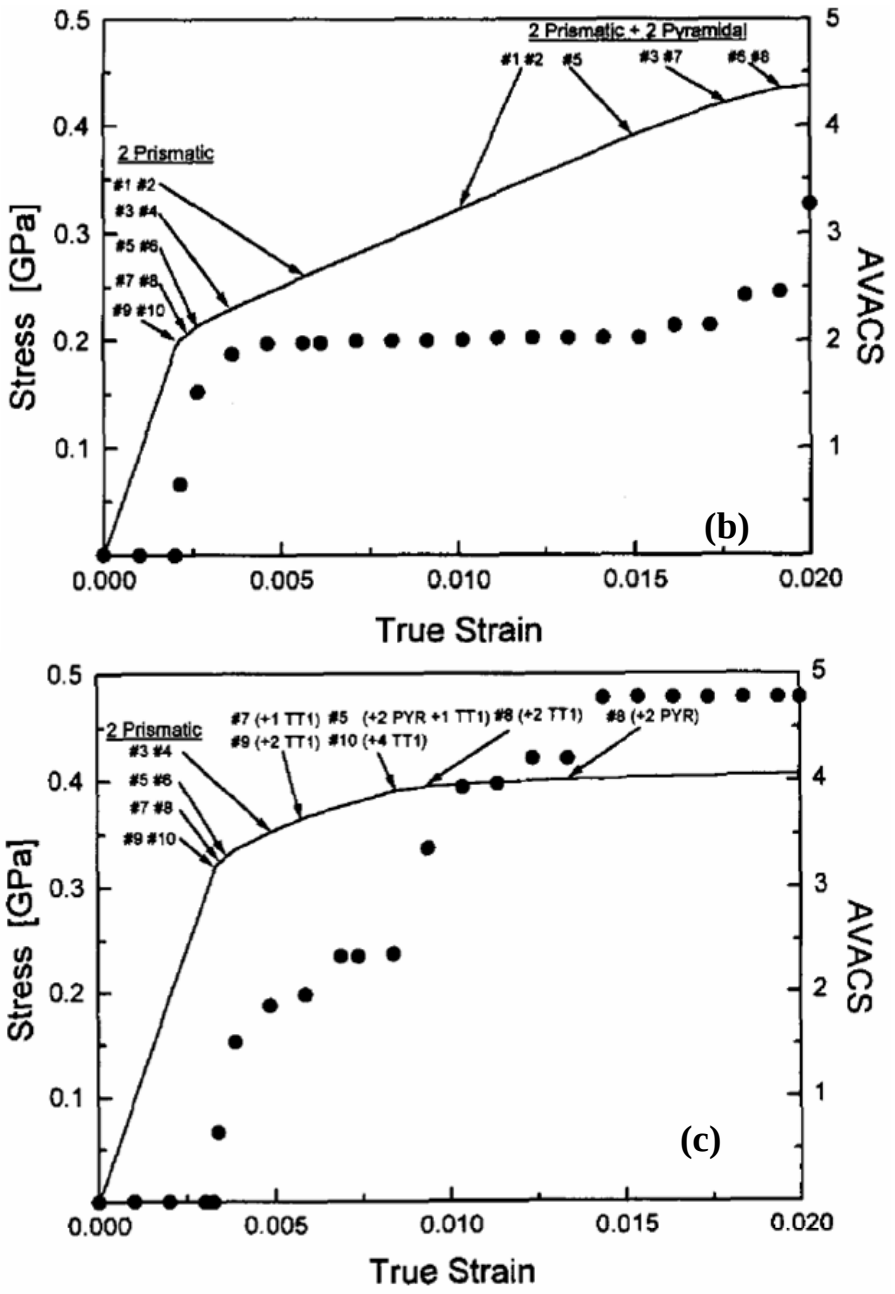

Figure 2.10 (continued) Predicted stress-strain response for (b) tension and (c) compression loading, along the rod axis. Also indicated is the Average Number of Active Systems per grain (AVACS) as a function of deformation [17].

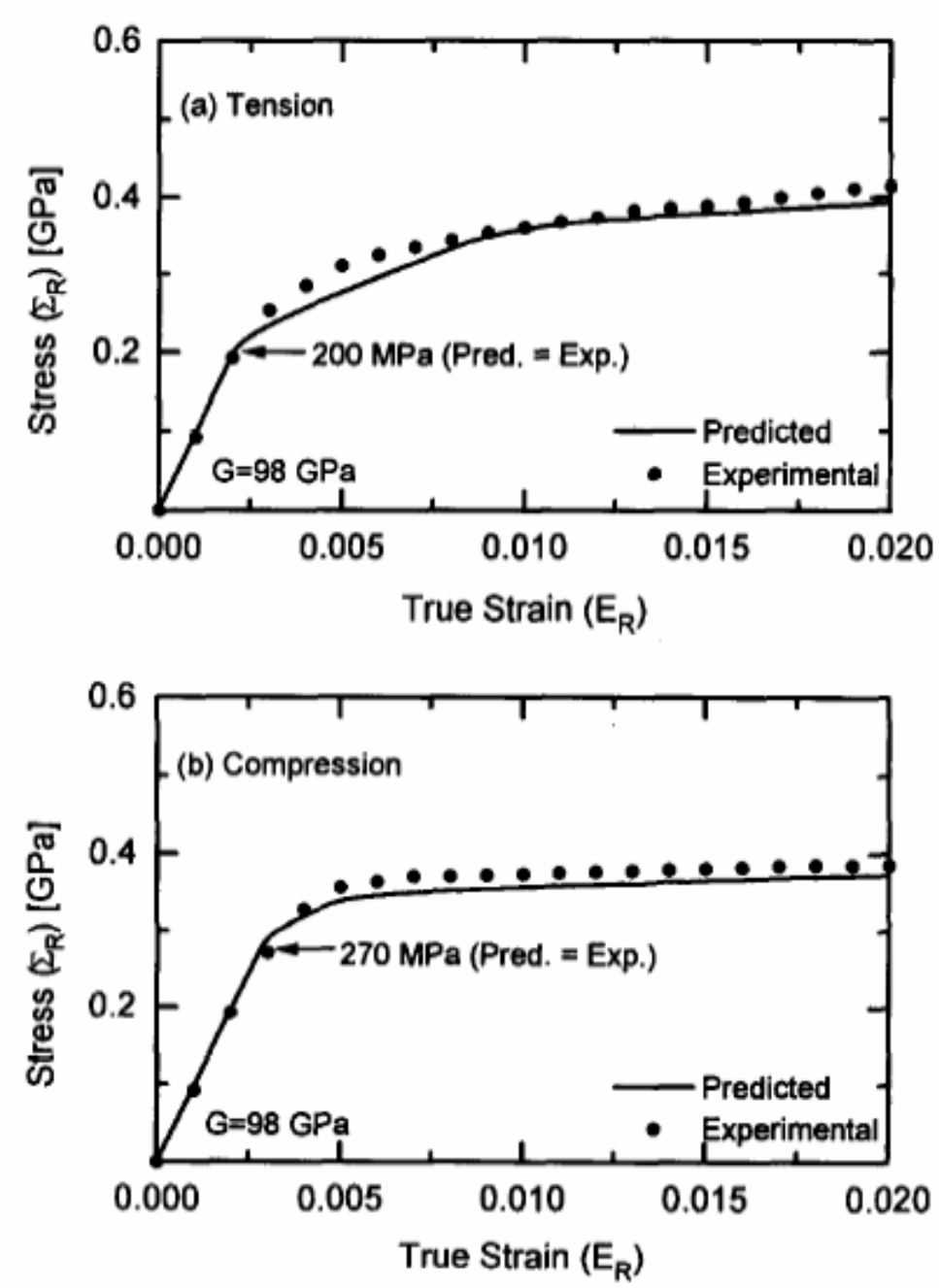

Figure 2.11 Predicted and measured stress-strain response for uniaxial loading along the rolling direction of the sheet for a Zircoloy-2 alloy: (a) Tension and (b) Compression [20].

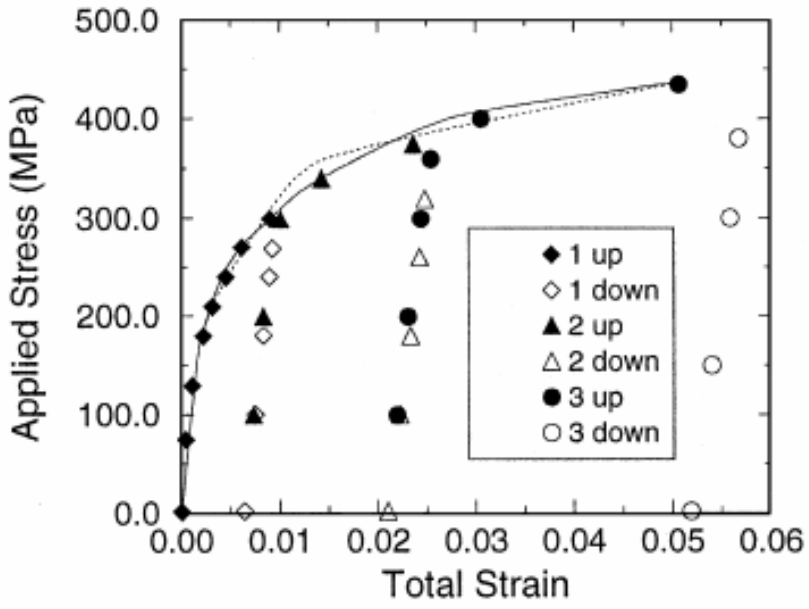

Figure 2.12 True stress-strain response of two test samples of Zr-2 of rod texture, under compression loading parallel and perpendicular to the rod axis.. The solid line indicates the simulated loading curves by the EPSC model with including basal slip as one of the slip modes, while the dotted line indicates the case without basal slip [14].

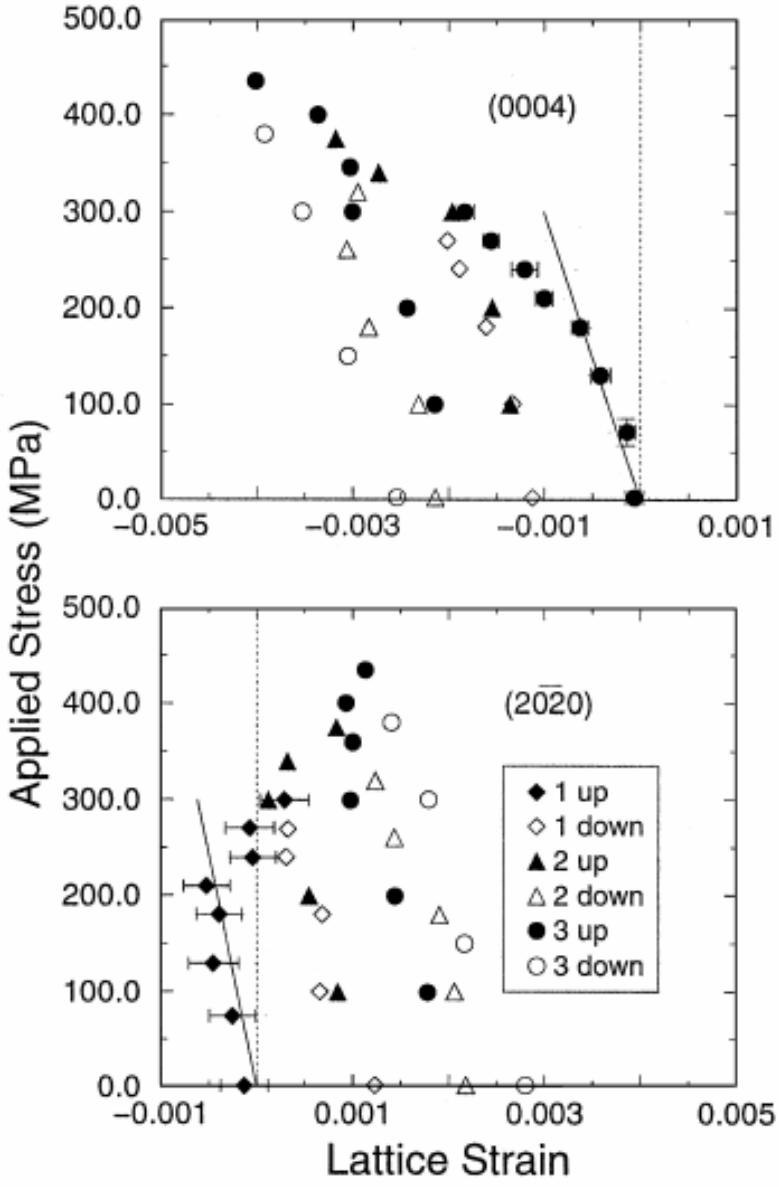

Figure 2.13 Transverse lattice strain response, as a function of applied stress for the (0004) and $(20\bar{2}0)$ reflections. The straight lines through the data at the beginning of the first loading path are the predicted linear elastic response to the applied stress from the EPSC model [14].

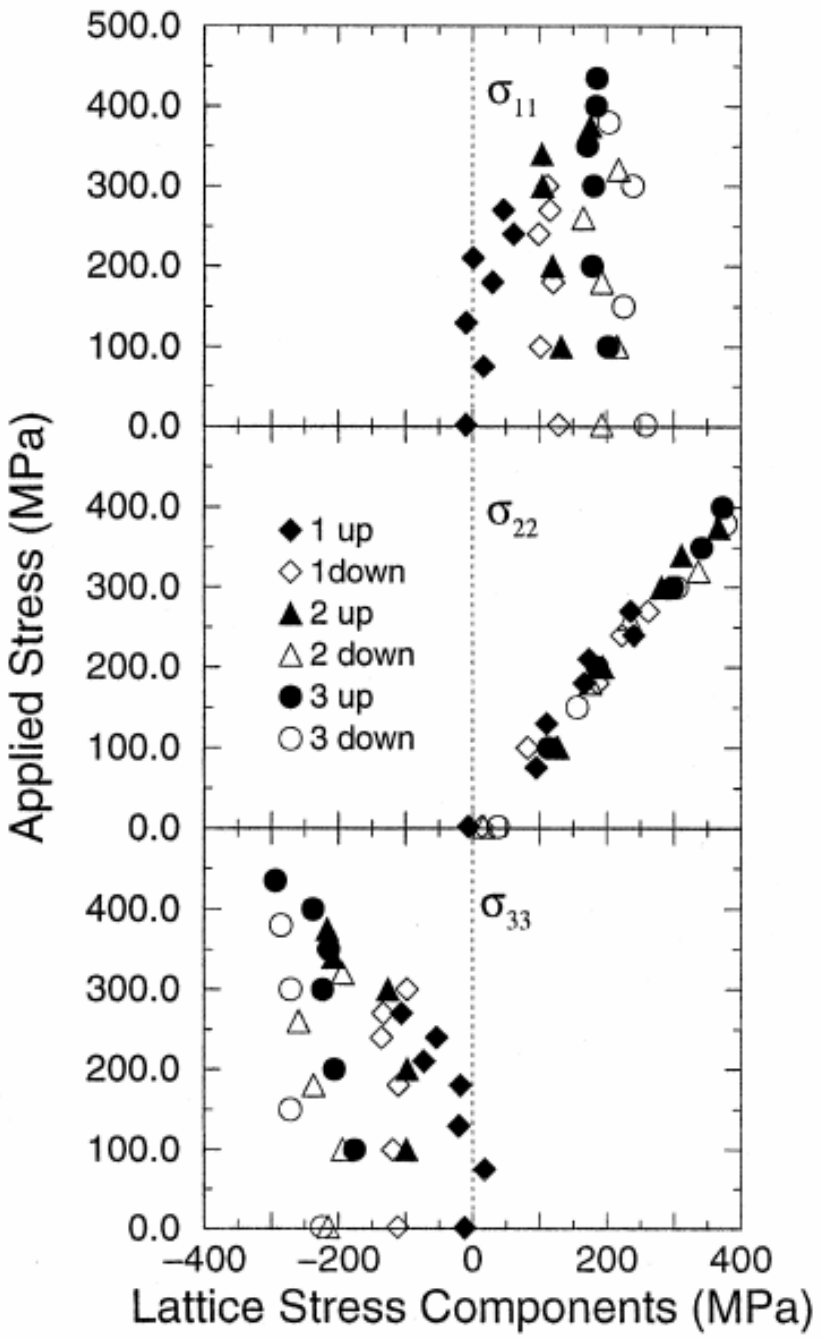

Figure 2.14 The principle lattice stress components σ_{11}, σ_{22}, and σ_{33} plotted as a function of applied stress. Uncertainties in the stresses are on the order of 20 MPa [14].

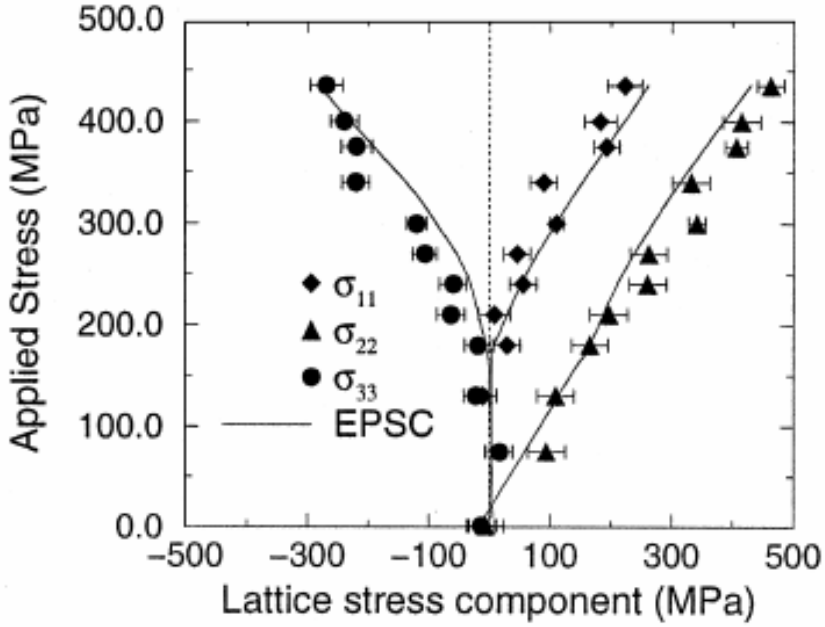

Figure 2.15 Simulations of the lattice stress components generated by 5% uniaxial deformation of Zr-2 with the EPSC model with prismatic, pyramidal, and basal slip systems considered in the calculation. The model calculation is shown by the solid curves and is compared directly with experiment [14].

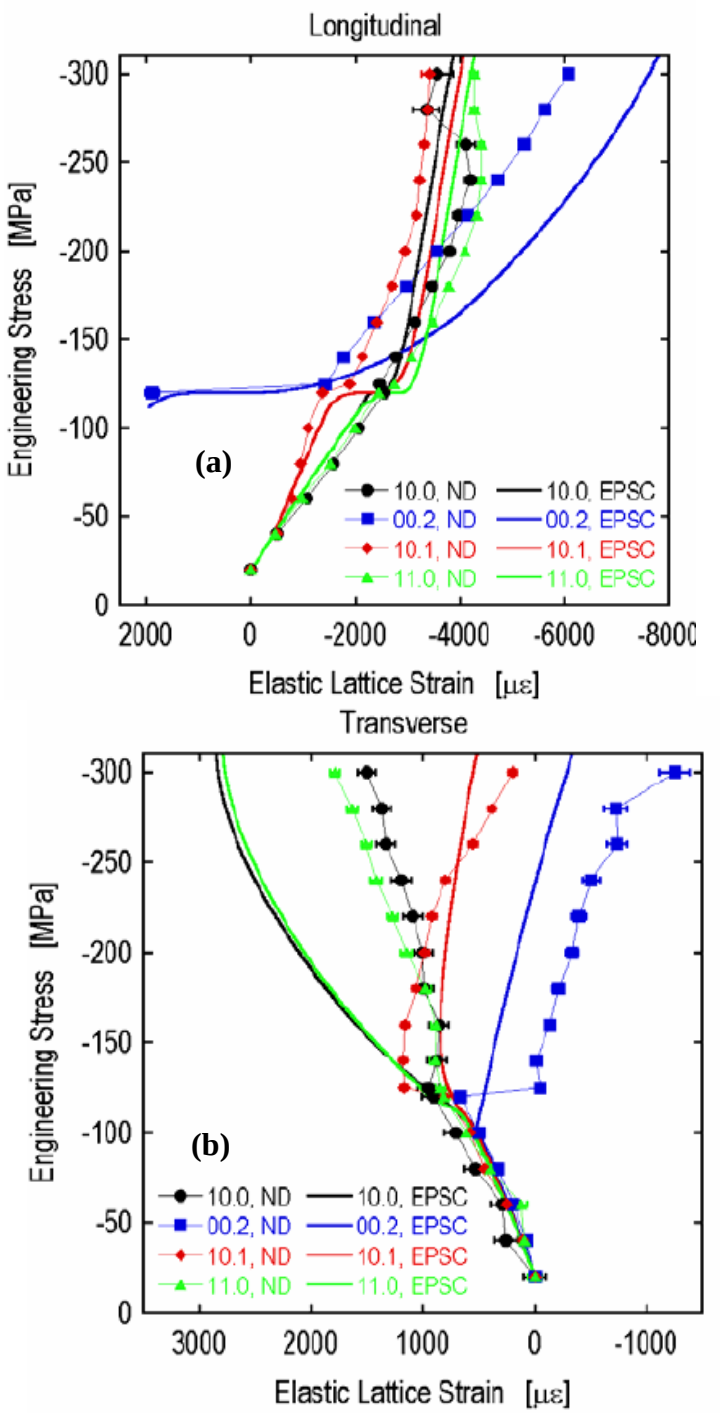

Figure 2.16 Measured (line and symbol) and predicted (thick line) elastic lattice strains a) parallel to the loading axis and b) perpendicular to the compressive loading axis [18].

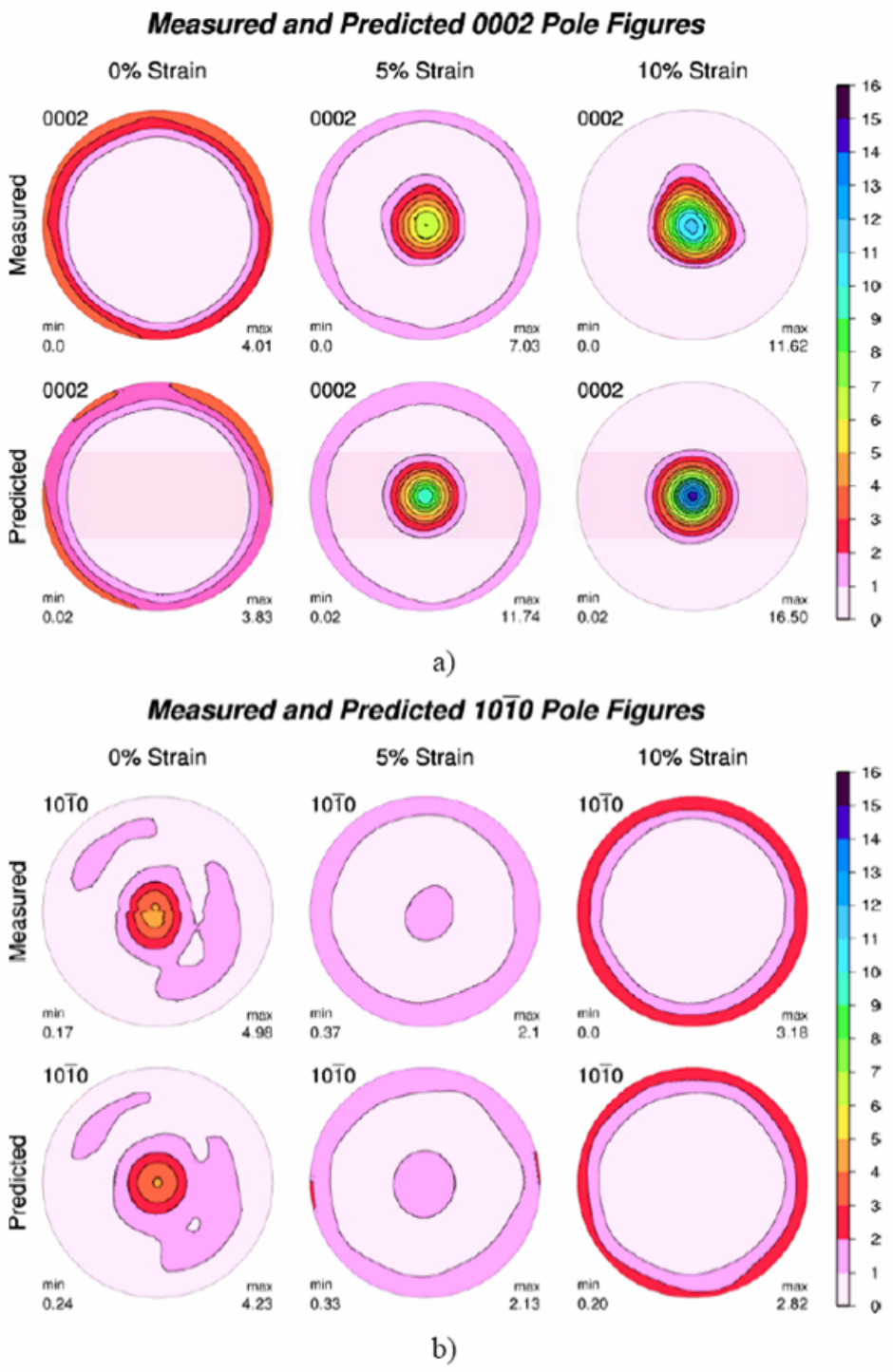

Figure 2.17 Texture measured using neutron diffraction and texture predicted by the self-consistent model due to the development of twining [18].

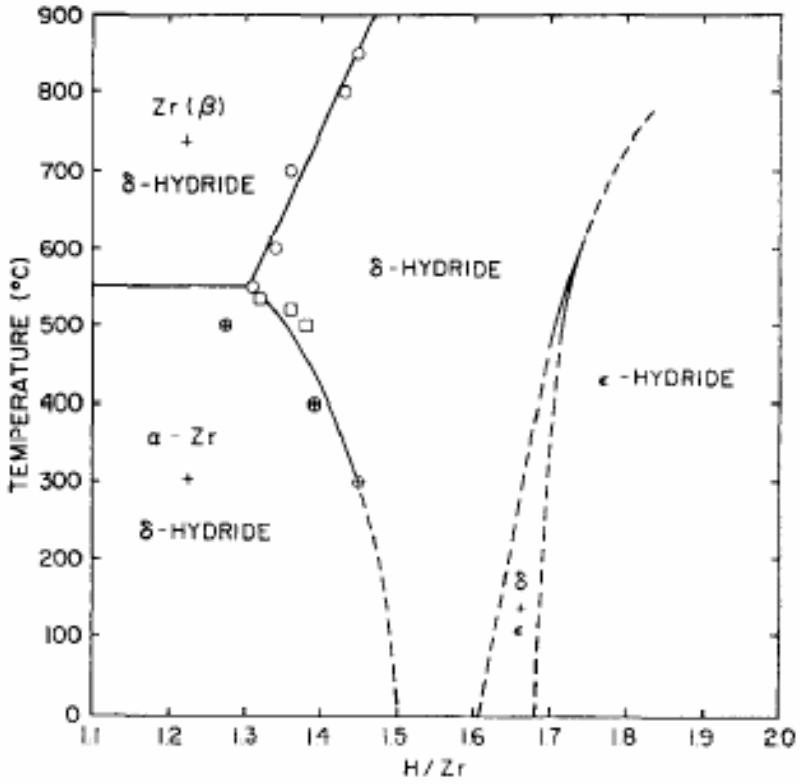

Figure 2.18 The zirconium-hydrogen phase diagram [39].

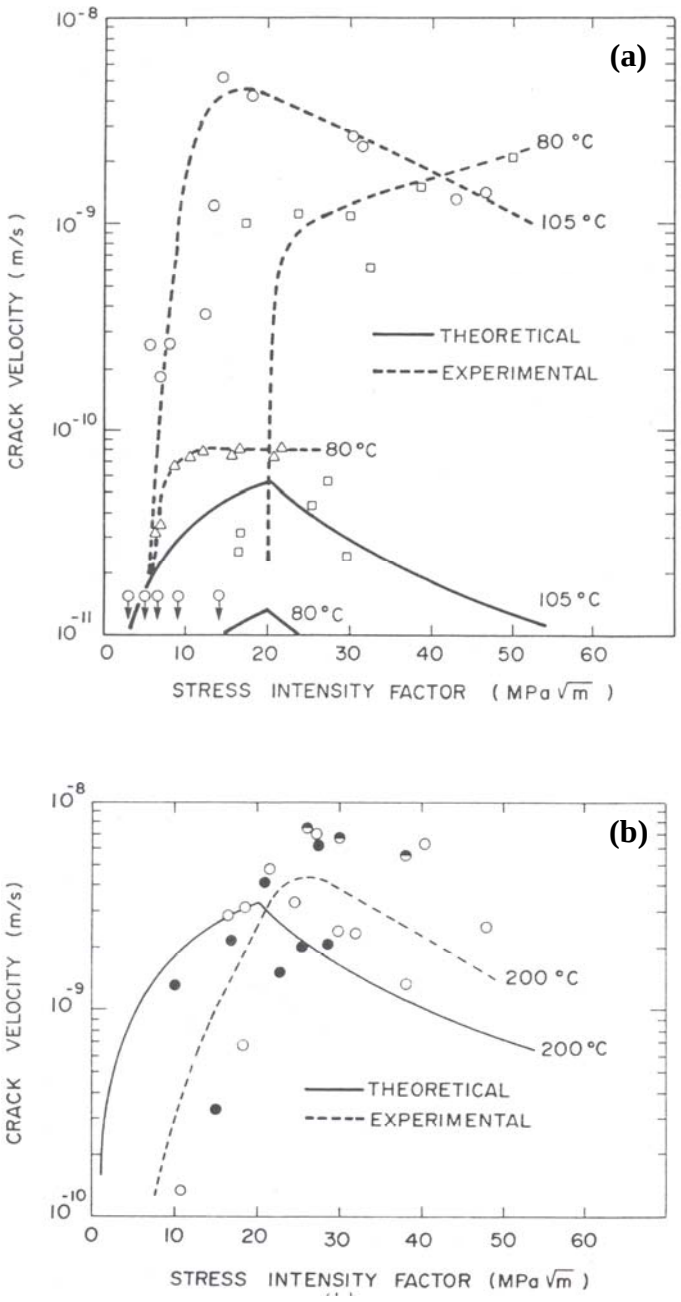

Figure 2.19 Theoretical and experimental plots of crack velocity as a function of the stress intensity factor range for cold worked Zr 2.5% Nb in the presence of Zirconium hydrides at different temperatures (a) 80 ˚C and 105 ˚C and (b) 200˚C [38].

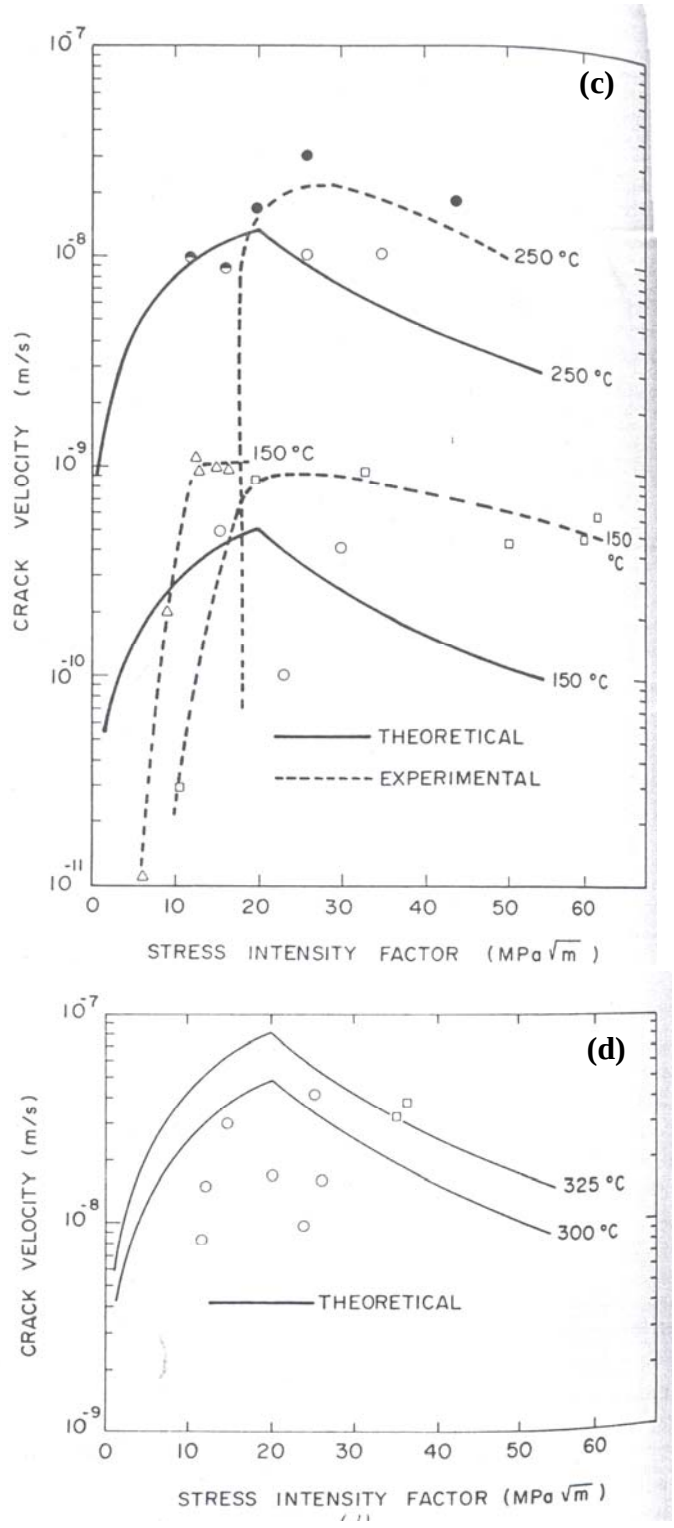

Figure 2.19 (Continued) (c) 150 ˚C and 250˚C, and (d) 300 ˚C and 325 ˚C [38].

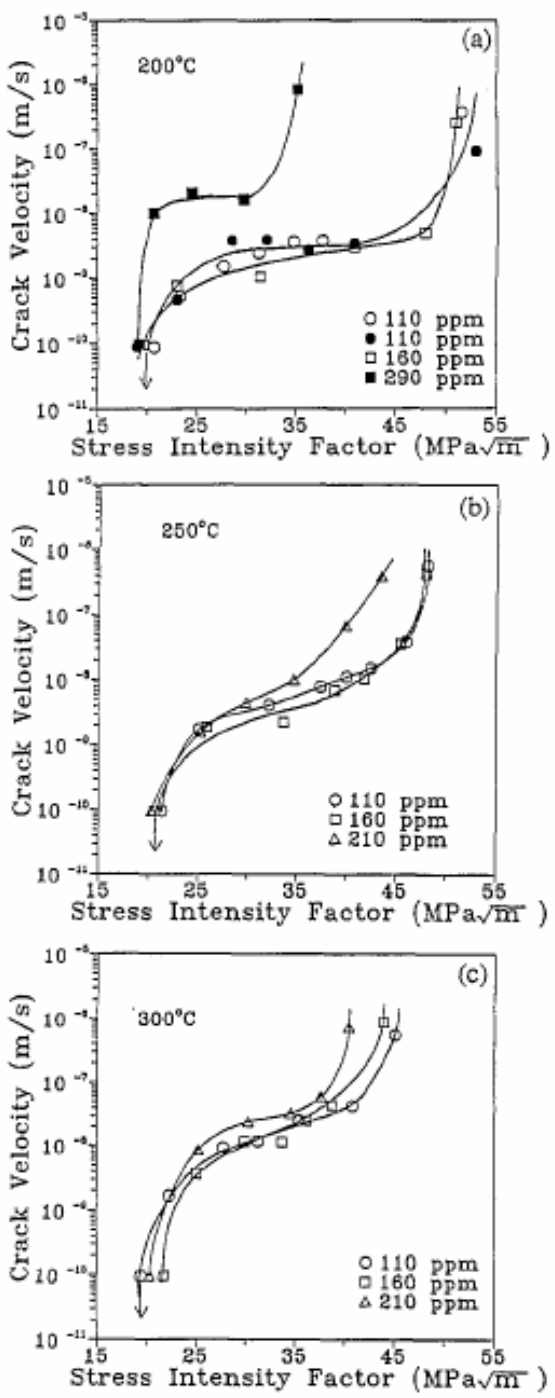

Figure 2.20 Crack growth rate in a Zircaloy-4 with various hydrogen contents tested at (a) 200 °C, (b) 250 °C, and (c) 300 °C under constant load [49].

CHAPTER 3

EXPERIMENTAL DETAILS, RESULTS, AND DISCUSSION

3. EXPERIMENTAL DETAILS, RESULTS, AND DISCUSSION

Abstract

Zircaloy-4 alloys are extensively used in nuclear industry because of the high-performance under severe pressure and temperature conditions coupled with high transparency to thermal neutrons. Zircaloy-4 alloys are polycrystalline zirconium alloys with a hexagonal-closed-packed (hcp) crystalline structure. During the service in the reactor, these alloys absorb hydrogen leading to formation of zirconium hydrides. As a result, hydride formation becomes one of the main degradation sources for zirconium alloys. Hydride formation is believed to be enhanced by the presence of residual or applied stresses. Therefore, the presence of the stress field ahead of a crack tip may promote precipitation of additional hydrides. In order to investigate these phenomena, the effect of internal stresses on the zirconium-hydride precipitates formation, and their subsequent influence on the fatigue behavior in a Zircaloy-4 alloy is investigated.

Firstly, the deformation systems responsible for the polycrystalline plasticity at the grain level, in a hexagonal-close-packed, coarse-grained, and random-textured Zircaloy-4 alloy are investigated. The evolution of internal strains was measured in-situ, using neutron diffraction by applying a series of uniaxial tensile loads to a round-bar tensile specimen up to 7% strain. The macroscopic stress-strain curve and the intergranular (hkil-specific) strain development, parallel and perpendicular to the loading direction, are studied. Then, a new elasto-plastic self-consistent (EPSC) modeling scheme are employed to simulate the experimental results. The model accounts for the anisotropic thermal, elastic-plastic properties of the constituent grains, and for the first

time activation, reorientation, and stress relaxation associated with twining. The fundamental understanding of the deformation mechanisms activated by the applied load in the elastic-plastic anisotropic Zircaloy-4 alloy is discussed. The model is in a good agreement with the measured data. The corresponding critical resolved shear stresses (CRSS) and the hardening coefficients are also provided.

Secondly, the hydride phase formation and its influence on fatigue crack growth in Zircaloy-4 alloy are investigated. The microstructure and fatigue behavior of the Zircaloy alloy in the as-received condition will be shown. Then, the formation and distribution of hydride phase and its effect on microstructure and the fatigue crack propagation rates will be discussed. Furthermore, the influence of a pre-existing fatigue crack on the subsequent hydride formation and distribution will be discussed. The residual lattice strain profile ahead of a fatigue crack was also measured using neutron diffraction and the combined effect of residual strain and hydride precipitation on the fatigue behavior is presented and discussed. In addition, the zirconium lattice strains evolution under applied loads of 900, 1,800, and 2,700 N in the presence of hydrides is studied and compared to the as-received condition.

Finally, we report the experimental results from a neutron incoherent scattering study and neutron radiography on Zircaloy-4 specimens charged with hydrogen. The estimation of total amount of hydrogen in the bulk specimen will be presented as a function of the hydrogen gas-charging time. Evidence for a non-uniform distribution of H within the specimen will be discussed. Then, preliminary results obtained by neutron imaging of the crack area for the three cases studied will be presented.

3.1 Microstructure and Deformation Mechanisms of the As-received Zircaloy-4 Alloy

3.1.1 Material and Microstructure

For this study, a commercial zirconium alloy, Zircaloy-4 (Zr-4) was used. The nominal chemical composition (weight percent, wt. %) of the starting Zr-4 is 1.5 Sn, 0.22 Fe, 0.12 Cr, 0.13 O, and balance Zr [1]. The specimens for optical microscopy investigation were mechanically polished up to 800 grit size followed by immersion in an etching solution of 45 ml nitric acid (HNO_3), 45 ml hydrogen peroxide (H_2O_2), and 10 ml hydrofluoric acid (HF) [2]. The microstructure of the Zr-4 is presented in Figs. 3.1, showing the Basketweave Widmanstätten type structure which forms during the transformation from the β (bcc) to α (hcp) phase, during cooling from 998˚C to room temperature. The former β–Zr grains have a mean diameter of 700 μm, Fig. 3.1(a), and each grain contains multiple α-Zr plates with different orientation, as seen in Fig. 3.1(b). Also typical for Zircaloy is the presence of the second phase precipitates, which appear as white spheroids under polarized light, Fig. 3.1 (b). These precipitates are insoluble in β-phase and their size and abundance can act as nucleation sites for the Basketweave structure by initiating the formation of α-Zr plates [3]. The orientation of α-Zr plates was investigated by Electron Back-Scattering Diffraction (EBSD). Fig 3.1(c) shows an EBSD image, which represents the [0001] inverse pole figure of the surface normal, via the color-coded stereographic triangle. The dark regions in the EBSD image are due to distorted lattices. Also showed in Fig. 3.1(c) is the [0001] pole figure relative to x - y axes of the specimen.

The texture for the starting Zr-4 alloy was measured using the High-Pressure Preferred Orientation (HIPPO) instrument, at Los Alamos National Lab [4]. Details of the instrument and the technique for determining the texture are described elsewhere [5, 6]. Fig. 3.2 shows six pole figures created for two prism planes Zr (10.0) and Zr (11.0), the basal plane Zr (00.2), and three pyramidal planes Zr (10.1), Zr (10.2), and Zr (10.3). None of the pole figures show intensity variation above 1.5 or below 0.5 multiples of random distribution (m.r.d), indicating an almost ideally random texture in the material prior to loading.

3.1.2 Intergranular strain and texture measurements during uniaxial tensile testing

The strain and texture measurements were conducted on a cylindrical tensile specimen with the total length of 101.6 mm, gage length of 19.05 mm, and gage diameter of 6.35 mm, using Spectrometer for Materials Research at Temperature and Stress (SMARTS) instrument [7] and the HIPPO instrument [4], respectively, at the Lujan Center, Los Alamos National Laboratory. Using the SMARTS instrument, *in-situ* uniaxial tensile loads were applied to the Zr-4 tensile specimen, and the internal strain evolution was measured using the setup schematically shown in Fig. 3.3(a). While bulk strain on the sample was monitored using an extensometer, the intergranular strains were obtained from neutron diffraction data collected at certain applied load intervals, Fig. 33(b). The diffraction gage volume employed for this study was defined by the incident beam width of 6 mm and height of 8 mm, and no collimation on the diffracted beam. The loading axis is horizontal at 45° to the incident beam, allowing simultaneous measurements of lattice-plane spacings (d-spacings) both parallel (longitudinal direction),

and perpendicular (transverse direction) to the loading direction, in the opposing 90° detector banks. The tensile test was carried out under strain control, and the lattice strain was measured to a total macroscopic (extensometer) strain of 7 %. The d-spacing for several individual reflections was obtained at each load by single peak fitting, using General Structure Analysis System (GSAS) [8] and the strain for these reflections, ε_{hkl}, was calculated using:

$$\varepsilon_{hkl} = (d_i - d_0) / d_0 \quad (3.1)$$

where d_i and d_0 are the d-spacing parameters of the strained and unstrained conditions, respectively. The first data point, before any load was applied, was considered the unstrained condition (d_0), and therefore it does not exclude the thermal residual strains existing in the specimen.

After the tensile test, the texture developed in the bulk was measured using the HIPPO instrument [4]. A schematic of the instrument is shown in Fig. 3.3(c). The initial and final textures were derived from a total of 98 neutron diffraction patterns, which were fitted simultaneously using Rietveld refinement [9], as implemented in GSAS [8]. The fitting program employs the spherical harmonic method [10] to describe the texture.

3.1.3 Elasto-plastic self-consistent (EPSC) modeling

For this study, we use the EPSC code implemented by Clausen *et al.* [11], which includes the texture development and stress relaxation due to twinning. In short, the model considers each grain an elastic-plastic ellipsoidal inclusion in a homogeneous effective medium (HEM) with the average properties of all the grains. The elastic stiffness and the thermal expansion coefficients of zirconium single crystal have been

used [12]. The initial texture was discretized into a set of 1944 grains that constitute the polycrystal within the calculations. The thermo-mechanical boundary conditions include a cooling cycle from the β phase at 998 ˚C to α phase at room temperature (20 ˚C), which accounts for the thermal residual stresses as they greatly influence the yield stress behavior. The macroscopic load is applied, and the boundary conditions are set for the grain interactions in a self-consistent manner, including the anisotropic elastic constants and slip mechanisms characteristic for the grains. The EPSC scheme includes an extended Voce hardening law for the evolution of CRSS, τ, with the total accumulated plastic shear within the grain, Γ:

$$\tau = \tau_0 + (\tau_1 + \theta_1\Gamma)\left(1 - \exp\left(-\frac{\theta_0\Gamma}{\tau_1}\right)\right) \tag{3.2}$$

where, τ_0 and θ_0 are the initial CRSS and hardening rate, respectively; θ_1 is the final hardening rate, and τ_1 is the transition range between initial and final hardening rate. These coefficients represent the fitting parameters that need to be introduced in the model to simulate the experimental data. The reported elastic strains for the reflections are given relative to the unloaded state at room temperature, for direct comparison with the neutron measurements. Also from the model, one obtains the relative activities for each system activated by the applied stress.

The current implementation of the model [11] also accounts for the texture development from twinning, with twins added as new grains. Additionally, the stress relaxation due to the twinning is taken into consideration by assuming a fixed initial size of the grains, which in turn determines the magnitude of back-stress generated in the twin and its parent. In the present case, an initial twin fraction of 2% was used. After the twin

grains are generated, they are not directly interacting with the parent grain, but interact with the HEM, in the same way as all the other grains. The texture development is realized by transferring weight fraction from the parent grain to the twin. This is governed by the incurred shear on the twin system in the parent grain. More details on the model are available in Ref [11].

3.1.4 Experimental results

The macroscopic stress-strain curve for uniaxial tension test, performed during the neutron experiment, for the hcp Zr-4 alloy is shown in Fig. 3.4. Note that, because the test was conducted under strain control, the macroscopic curve shows the time average stress versus the total strain. The tensile behavior indicates that the bulk elastic modulus (E), the elastic limit, and 0.2% yield stress (σ_y) are about 100 GPa, 190 MPA, and 318 MPa, respectively.

The measured in-situ elastic lattice-strain evolution for six zirconium reflections, in both longitudinal (plane normal is parallel to the tensile axis) and transverse (plane normal is perpendicular to the tensile axis) directions, is presented in Figs. 3.5(a) and (b), respectively. It is worth mentioning that data for many more reflections were obtained, however, for clarity, we are showing only six. The chosen reflections correspond to two prism planes Zr (10.0), Zr (11.0), the basal plane Zr (00.2), and three pyramidal planes Zr (10.1), Zr (10.2), Zr (10.3). Also in Figs. 3.5, the macroscopic elastic limit at 190 MPa and the 0.2 % yield stress at 318 MPa are marked. It can be observed that, during the elastic regime, the lattice strains exhibit isotropic behavior in both directions.

In the plastic regime, the internal strains manifest strongly anisotropic and non-linear behavior as the plastic strain component is starting to act. In particular, the longitudinal Zr (00.2) has a very abrupt tensile deviation from linearity, which suggests that mainly plastic deformation is accumulated.

The pole figures for the six reflections, measured at the end of the tensile test, are presented in Fig. 3.6, which show the development in the texture of the Zr-4 alloy under the tensile loading. For the [10.1] pole, there is an increase in pole density at center of the pole figure, whereas the [11.0] pole has its center depleted, with the higher density around it. The basal pole, [00.1] transforms from a four-fold symmetry at the edge, prior to the tensile test, to a six-fold symmetry after deformation.

3.1.5 Calculated results and discussion

Due to the complex deformation behavior of Zircaloys, we have explored a large number of possible deformation systems and hardening coefficients in the EPSC model, to better understand the neutron diffraction results. In particular, we are presenting three possible cases, Cases 1-3, which are the most reasonable scenarios based on the initial interpretation of the experimental data. For Case 1, a combination of slip systems are considered, while for Case 2 and Case 3 twinning is activated at different final volume fractions, in addition to slip systems.

Therefore, in the calculation for Case 1, it was assumed that the following deformation systems are active: the prism slip $<\bar{1}2\bar{1}0>\{10\bar{1}0\}$, the basal slip $<2\bar{1}\bar{1}0>\{0001\}$, the <a> pyramidal slip $<\bar{1}2\bar{1}0>\{10\bar{1}1\}$, the <c+a> first order

pyramidal slip $<\bar{1}\,\bar{1}\,23>\{10\bar{1}\,1\}$, and <c+a> second order pyramidal slip $<2\bar{1}\,\bar{1}\,\bar{3}>\{2\bar{1}\,\bar{1}\,2\}$. The CRSS values for these systems, and the corresponding hardening coefficients, are shown in Table 3.1, while the obtained curves are shown in Figs. 3.7. The calculated macroscopic stress-strain curve (line) exhibits a very good agreement with the experimental data (symbol), as seen in Fig. 3.7(a). The simulated lattice strains evolutions (lines) are plotted together with the experimental data (symbols), for both longitudinal and transverse directions, Fig. 3.7(b-e). The extreme behavior for longitudinal Zr (00.2), Fig. 3.7(b), has been quantitatively captured by the calculation, and so are the two prism planes. A very good fit was also obtained for these three planes in the transverse direction, Fig. 3.7(d).

Table 3.1 Case 1: The deformation slip systems, and the corresponding CRSS and hardening coefficients used for the Case 1- EPSC calculation, Fig. 3.7.

Deformation system	τ_0 (MPa)	τ_1 (MPa)	θ_0 (MPa)	θ_1 (MPa)
Prism	110	10	510	10
Basal	215	10	10	10
Pyramidal<a>	110	30	2,550	0
Pyramidal<c+a>	230	10	310	80
Pyramidal<c+a> 2nd order	220	10	310	310

The simulation for the elastic regime is in quantitative agreement with the measured profiles of intergranular strain behavior for the three pyramidal planes Zr (10.1), Zr (10.2), and Zr (10.3), in longitudinal direction, Fig. 3.7(c). However, upon entrance into the plastic regime, the calculated results of Zr (10.2) and Zr (10.3) do not quite agree with the neutron data quantitatively, while still capturing the qualitative behavior of the profile reasonably well. In particular, Zr (10.2) exhibits a slight decrease in slope, indicating that this grain orientation is predicted to behave elastically in the transition region. However, the model indicates that some plasticity is accumulated at loads greater than 350 MPa (upward inflection), which is qualitatively consistent with the measured data. In the transverse direction, Fig. 3.7(e), Zr (10.3) shows a quantitative match in both elastic and plastic regimes. The Zr (10.2) shows only qualitative agreement in the plastic regime, while Zr (10.1) exhibits an approximately vertical trend in the transition and plastic regions, and does not quite follow the significant slope reversal observed in the experimental data. The quality of the obtained agreement between the EPSC calculation and measured intergranular lattice strains is comparable with that reported on Magnesium alloys by Clausen *et al*. [11] and Agnew *et al*. [13].

The deformation systems acting under the applied load, and their relative activities, are presented in Fig. 3.7(f). It shows that prism, pyramidal <a>, and second order <c+a> pyramidal slip systems are acting first, followed by the first order <c+a> pyramidal, and then, the basal slip systems. The presence of prism and first order <c+a> pyramidal slip as deformation systems in zirconium alloy had been extensively observed [12, 14, 15, 16]. The contribution of the pyramidal <a> slip system was observed to have a direct impact on the profiles for the longitudinal pyramidal planes. In particular, the

(10.1) reflection exhibits significantly improved agreement with the measurement, after pyramidal <a> was added to the model. This is at odds with the results reported in Ref. [14], where a non-significant contribution has been suggested. The second order <c+a> pyramidal slip had a great influence on the abrupt profile of the strain evolution in Zr (00.2) grains, in longitudinal direction. Basal slip systems had been reported to improve the agreement between the experiment and the model [12, 14]. Due to the fact that only the slip systems were activated in this simulation, and no twinning systems, the texture cannot be predicted using the current modeling scheme. Note that, at this moment, this EPSC modeling scheme calculates texture developed due to twinning only.

Let's us examine now, in more detail, the measured texture that developed at the end of tensile test (7 % total strain). From the comparison of the prism poles with the basal pole, one can observe that they have a correlated behavior. This behavior seems to be consistent with a lattice rotation of about 85 degrees, which, in general, is associated with tensile twinning [17]. Therefore, the possibility of twinning has been explored and it is presented further on Case 2 and Case 3.

Case 2 calculation accounts for the activity of tensile twinning, in addition to the slip systems. Thus, the Case 2 consider the activity from the prism slip $<\bar{1}2\bar{1}0>\{10\bar{1}0\}$, the basal slip $<2\bar{1}\bar{1}0>\{0001\}$, the <a> pyramidal slip $<\bar{1}2\bar{1}0>\{10\bar{1}1\}$, the <c+a> first order pyramidal slip $<\bar{1}\bar{1}23>\{10\bar{1}1\}$, and tensile twinning $<\bar{1}011>\{10\bar{1}2\}$. The magnitude of CRSS and the corresponding hardening coefficients for each system are indicated in Table 3.2, and the obtained curves in Figs. 3.8(a-c). The agreement between the calculation and experiment is very similar with Case 1, Figs. 3.7. However, in

longitudinal direction, Zr (10.3), as well as Zr (10.2), experience a decrease in slope and deform plastically (upward inflection) above 350 MPa, Fig. 3.8(b). Also, the relative activity for each system is plotted as a function of the applied load in Fig. 3.8(d). The first inflection in the internal strain evolution occurs at around 200 MPa, when twinning is activated as the first active deformation system. Subsequently, Fig. 3.8(e), the twin volume fraction shows a significant increase, given by the prescribed 2 % minimum twin fraction. At the end of the tensile test, the final twin volume fraction is about 3 %. The tensile twinning is followed shortly by prism and pyramidal <a> slip. At loads close to 300 MPa, pyramidal <c+a> and basal slip systems start to play a role in the deformation. Another observation is that the child grains also exhibit plasticity through slip. At about 350 MPa, large slip activities are observed in the child grains, by prism and pyramidal <a> systems.

Table 3.2 Case 2: The deformation systems (slip and 3 % tensile twinning), and the corresponding CRSS and hardening coefficients used for the Case 2 - EPSC calculation, Fig. 3.8.

Deformation system	τ_0 (MPa)	τ_1 (MPa)	θ_0 (MPa)	θ_1 (MPa)
Prism	110	10	10	10
Basal	200	30	10	10
Pyramidal<a>	110	40	2,250	0
Pyramidal<c+a>	250	10	310	10
Twinning 2%	220	10	310	310

It is worth noting that the calculation treats the twins, once formed, as separate grains. However, in reality, the stress relaxation that takes place in the parent grain, due to the twin shear, can affect the stress state in the twin.

The texture predicted by Case 2 calculations is shown in Fig. 3.8(f), and it is solely attributed to the twinning activity. From the comparison of the calculated texture with the measured ones, i.e., before the tensile test (Fig. 3.2) and after the test (Fig. 3.6), one can notice that the modeled texture is similar with the texture before the tensile testing, with the exception of the depletion at the center of the basal plane. This suggests that the predicted 3 % final volume fraction of twinning does not play an essential role on the plastic deformation of this Zircaloy-4 alloy.

Finally, for the Case 3 simulation, the twinning final volume fraction was further increased, in an attempt to amplify its effect on the texture development. This was accomplished by giving the zero values to the hardening coefficients of tensile twining. The activated systems are similar to the Case 2 calculation: the prism slip $<\bar{1}2\bar{1}0>\{10\bar{1}0\}$, the basal slip $<2\bar{1}\bar{1}0>\{0001\}$, the <a> pyramidal slip $<\bar{1}2\bar{1}0>\{10\bar{1}1\}$, the <c+a> first order pyramidal slip $<\bar{1}\bar{1}23>\{10\bar{1}1\}$, and tensile twinning $<\bar{1}011>\{10\bar{1}2\}$. The CRSS values and the hardening coefficient are shown in Table 3.3. The obtained profiles are presented in Figs. 3.9(a-c), showing a similar agreement with Case 2 for most of the grain sets.

Table 3.3 Case 3: The deformation systems (slip and 12% tensile twinning), and the corresponding CRSS and hardening coefficients used for the Case 3 - EPSC calculation, Fig. 3.9.

Deformation system	τ_0 (MPa)	τ_1 (MPa)	θ_0 (MPa)	θ_1 (MPa)
Prism	110	10	10	10
Basal	210	30	10	10
Pyramidal<a>	120	40	750	0
Pyramidal<c+a>	260	10	310	10
Twinning 2%	220	0	0	0

However, there is a poor agreement for longitudinal Zr (00.2) above 380 MPa. This deviation from the experiment coincides with the activation of slip systems in twin (child) grains, Fig. 3.9(d). We observed that in order to improve this misfit, the twinning volume fraction needed to be reduced, which would transform the Case 3 into the Case 2. The final twin volume fraction is about 12% for Case 3 calculation, Fig 3.9(e). The predicted texture due to twinning, Fig 3.9(f), is similar to the measured one after the tensile test, Fig. 3.6, for the prism and the basal poles. However, the calculation exhibits few differences, such as the presence of the depleted area at the center of basal pole, and the features at the center of prism poles. While the measured [10.1] pole has the maximum density at its center, the predicted pole has the center depleted and the high density around it. A similar trend is exhibited by the [11.0] pole as well. The deformation systems considered in Case 3, i.e., slip and significant tensile twinning activity, predict a

texture quite similar to the experimentally measured texture after loading, with a significant detriment to the lattice strain evolution.

Based on the three cases discussed here, it can be concluded that the tensile twinning does not play a significant role on the plastic deformation of this alloy under the current experimental conditions. When the model uses a combination of slip systems, the macroscopic behavior and the lattice strain evolution exhibit good agreement with the experimental data. However, the texture development due to slip is not possible to model with the current EPSC scheme.

3.2 Hydride Phase Formation, Its Influence on Fatigue Crack Propagation, and In-Situ Evolution of Lattice Strains at the Fatigue Crack Tip

3.2.1 Compact-tension specimens

Three different cases (CT 1, 2, and 3) were studied using compact-tension specimens. Specimen drawing and dimensions are shown in Fig. 3.10(a), and the specimen preparation and fatigue testing steps are illustrated in Figs. 3.10(b-d). The CT specimens were machined in accordance with the ASTM Standard E647–86 [18]**,** with a width (W) of 50.80 mm, length of 63.5 mm, and a thickness (B) of 6.35 mm. For the CT 1 case, an as-received specimen was fatigued to failure following the steps illustrated in Fig. 3.10(b). This specimen is considered the reference sample. The CT 2 specimen was charged with hydrogen prior to fatigue testing to investigate the effect of homogenously distributed hydrides on the fatigue crack growth, Fig. 3.10(c). On the other hand, for the CT 3 condition, the specimen was fatigued to a crack length of 22.86 mm and, then,

charged with hydrogen, as illustrated in Fig. 3.10(d). After the charging, the specimen was fatigued to failure, in an attempt to investigate the impact of the pre-existing crack (and the residual stresses associated with the crack tip) on the hydride formation, and, in turn, its subsequent influence on the crack propagation rate.

3.2.2 Hydrogen charging

The CT 2 and CT 3 specimens were charged with hydrogen (H) at an elevated temperature to form zirconium hydrides. First, to promote the hydrogenation process, an area of 20 x 30 mm^2 around the crack on both sides of the specimen, indicated in Fig. 3.10(a) by the shaded area, was coated with a Ni layer with a thickness of 0.20 μm. Nickel dissociates the molecular H_2 to atomic H by chemisorption, which excites the *d* electrons in Ni [19]. As a result, the *s* electrons from H fill the *d* orbitals of Ni, resulting in Ni-H bonds with a moderate weakening of the Ni-Ni bond. The Ni thin film was deposited on the zirconium CT specimens using an AJA ATC2000 RF magnetron sputtering system. The deposition was performed at room temperature and total pressure of 5 mTorr. A RF power of 200 Watts was applied.

In order to remove the protective oxide layer on the specimen surface before the Ni coating, each specimen was mechanically polished up to an 800 grit size, and then, chemically polished by immersion in a solution of 45 ml hydrogen peroxide (H_2O_2), 45 ml nitric acid (HNO_3), and 10 ml hydrofluoric acid (HF) [2]. After the Ni coating, the specimens were hydrogen charged using a 12.5 vol. % hydrogen in argon mixture in a tube furnace at a temperature of 414 °C, under a pressure of 13.8 kPa, for 50 minutes. The setup employed for the H charging is shown in the picture, Fig. 3.11(a) and in the

schematic, Fig. 3.11(b). Subsequently, the specimens were annealed at 385 °C for 5 hours in the hydrogen-argon atmosphere. After annealing, the samples were left in the furnace to cool down to room temperature at a rate of 3-5 deg/min [20].

3.2.3 Fatigue crack growth testing

For this study, the macroscopic mode I of fracture was chosen, also known as the tensile opening mode, in which the crack faces separate in a direction normal to the plane of the crack. The CT specimens were pre-cracked and fatigued using a servo-hydraulic Material Test System (MTS) testing machine, which is interfaced with a Teststar IIs controller. The details of pre-cracking, fatigue cracking (fatigue crack growth - FCG), and hydrogen charging steps are illustrated in Figs. 3.10(b-d). Each specimen was pre-cracked under a constant stress-intensity-factor range (ΔK) to the crack length, *a*, of 11.43 mm. The fatigue crack growth (FCG) tests were performed under an increasing ΔK control mode, constant load, with a frequency of 10 Hz and a constant load ratio, R = P_{min}/P_{max} = 0.1 at ambient temperature. The maximum stress intensity, K_{max}, can be calculated using [21]:

$$K_{\max} = \frac{P_{\max}(2+\alpha)}{B\sqrt{W}(1-\alpha)^{3/2}}(0.886 + 4.64\alpha - 13.32\alpha^2 + 14.72\alpha^3 - 5.6\alpha^4) \qquad (3.3)$$

where P_{max} is the maximum load applied, and α is the ratio between the crack length and specimen width, α = a/W. Crack length was measured by the crack-opening-displacement (COD) gauge using the unloading-compliance method [22]. In a fatigue crack growth test, data is recorded using a computer data-acquisition system, and, then, plotted as the

crack length *a* versus the number of cycles to fatigue failure, *N*. The crack growth rate, da/dN, is taken as the slope at some point of the curve, and it is a function of the stress level, crack size, and material properties. Mathematically, this crack propagation rate, da/dN, may be expressed in terms of the stress intensity factor range, ΔK [23]:

$$\frac{da}{dN} = C(\Delta K)^m \tag{3.4}$$

where *C* and *m* are scaling constants and depend on the material microstructure, fatigue frequency, load ratio, environment, and test temperature. In our case (tensile fatigue), the ΔK is the mode I stress intensity factor range during the stress cycle at the crack tip, and it is defined as:

$$\Delta K = K_{\max} - K_{\min} \tag{3.5}$$

While the pre-cracking part is performed with variable loads (constant ΔK) , the P_{max} value must be carefully chosen for the fatigue crack growth tests such that the fatigue experiments could be continued after the hydrogen charging, which was expected to embrittle the sample significantly. The P_{max} employed in this study was 4,000 N, and the fatigue crack growth tests were conducted to the failure of the specimens. However, in the case of CT 3, we used two specimens, namely CT 3a and CT3b. Both specimens were first fatigued with P_{max} = 4,000 N to the crack length of 22.86 mm (FCG 1), Fig. 3.10(d). At that point, the specimen were taken out from the MTS machine and charged with hydrogen for 50 minutes as described in the previous section. After hydrogen charging, the fatigue test was continued, for CT3a, using a P_{max} = 4,000 N, which failed the specimen immediately during the first cycle. Therefore, the maximum load applied was

lowered to P_{max} = 1,300 N, which was used for the fatigue crack growth to the failure of CT 3b after the hydrogen charging, (FCG 2 in Fig. 3.10(d)), keeping the same load ratio, R = 0.1.

3.2.4 Metallography and x-ray diffraction

The specimens for the optical microscopy investigation were mechanically polished up to an 800 grit size. To reveal the zirconium hydrides, each specimen was etched by immersion in a solution of 46 ml nitric acid (HNO_3), 4 ml hydrofluoric acid (HF), and 50 ml lactic acid ($C_3H_6O_3$) [2]. Using an image plot profile software, Image J (Image Processing and Analysis in Java), the hydride distribution was visualized using the contrast variation on each micrograph. Using the same software and the point counting method, the volume fraction of hydrides was determined [24, 25]. X-ray diffraction was used to identify the phases on the polished surfaces of the hydrogen-charged samples. The scans were performed using CuKα radiation (λ = 1.542 Å), 2 x 2 mm^2 incident beam, 0.01° step size, and 5 sec/step scan rate.

Each specimen fatigued to failure was analyzed by scanning electron microscopy (SEM), using a Leo 1526 SEM. The fracture surfaces of as-received and hydrogen-charged conditions were investigated at specific values of the stress intensity factor range (ΔK) to study the fatigue and the fracture behaviors.

3.2.5 Observed microstructures

The phases present after hydrogen charging were studied by x-ray diffraction at approximately 1.4 mm below the surface of the CT specimens. A typical x-ray diffraction

pattern, intensity vs. 2 theta, is presented in Fig. 3.12. Three reflections corresponding to the hcp α-Zr phase, Zr $(10\bar{1}0)$, Zr (0002), and Zr $(10\bar{1}1)$, and two peaks ZrH_2 (111) and ZrH_2 (200), corresponding to fcc Zirconium hydride, δ-ZrH_2, are identified by peak indexing.

Figure 3.13(a) shows a schematic of the upper half of the CT specimen. The green square at the crack tip indicates the location of the micrographs taken at low magnification, Figs. 3.13(b-d-f), and higher magnification, Figs. 3.13(c-e-g). These micrographs indicate the microstructure of Zircaloy and the formation of Zirconium hydrides. (Note that the images were taken after approximately 1.4 mm from the surface of each specimen was removed, where ~ 6 mm is the original specimen thickness). The microstructure for the Zircaloy-4 in the as-received condition, CT 1 specimen, is presented in Figs. 3.13(b-c). It shows the α-Zr Basketweave Widmanstätten type structure, which contains the α-Zr plates with different orientation, as indicated in Fig.3.1. The white spheroids that appear under the polarized light, Fig. 3.13(c), represent the second phase precipitates present in the grain body. In our case, the second phase precipitates are Fe-Cr with an initial reported content of 0.33 wt. % Fe-Cr [1]. The microstructure for the CT 2 (H charged and fatigued) specimen is shown in Figs. 3.13(d-e) at lower and higher magnifications, respectively. By comparison with Fig. 3.13(b), one can observe the presence of the hydride phase in the Zircaloy microstructure at the boundaries of α-Zr plates. During the 50 minute hydrogen charging at 414 ˚C, H_2 dissociates on the area coated with Ni and in turn, forms a thin layer of Zirconium hydrides at the surface of the specimen. This is followed, during the 5 hours annealing, by the diffusion of hydrogen into the specimen bulk, and subsequently, by the

precipitation of δ-ZrH_2 during cooling. It should be pointed out that the typical room-temperature hydride phase for Zircaloy alloys is the δ-ZrH_2 plates [26]. The microstructure for the CT 3 (fatigued and H charged) specimen at the crack tip is shown in Figs. 3.13(f-g), indicating a higher concentration of hydrides than CT 2. Also presented in Figs. 3.13(h-j) is the distribution of hydrides from the gray-shaded area of 30.4 x 14.8 mm^2, marked in Fig. 3.13(a) for each of the three specimens. The horizontal red dotted line denotes the outer edge of the Ni coated area. The as-received condition, the reference for this comparison, is shown in Fig. 3.13(h). CT 2 specimen exhibits a reasonable uniform but darker image than CT 1, Fig. 3.13(i). The distribution of hydrides through the width of the CT 3 specimen is presented in Fig. 3.13(j), which exhibits a significantly darker localization by the crack. The contrast on these images is graphically represented in Fig. 3.134(k), by plotting the color contrast integrated over the whole area of 30.4 x 14.8 mm^2. The high values at the beginning and the end of each graph represent the edges of the specimens (the black areas in Figs. 3.13(h-j)). While CT 1 is the based line, the hydrides in CT 2 specimen are reasonably uniformly distributed through its width, with a slightly higher concentration on the Ni coated area. In the case of CT 3, hydrides are more localized around the crack and, interestingly, further away from the crack, the contrast becomes similar with the as-received condition. Note that the vertical black dash-dot lines along the width of the half-specimen indicate the position of the crack tip for CT 3 during H charging. It also represents scan lines along which the hydride volume fractions were obtained for both specimens, CT 2 and CT 3. Figure 3.13(l) shows the evolution of the hydride volume fraction, at 1.4 mm from the surface, which exhibit similar profiles with those observed in Fig. 3.13(k). In addition, the hydride

volume fractions, along the specimens' width, were investigated at the middle of the specimen thickness, for both cases, Fig. 3.13(m). Both specimens exhibit similar hydride content at the middle of the thickness, which can be related to the amount of hydrogen that penetrated into the bulk during the charging and annealing time.

3.2.6 Fatigue-crack-propagation behavior

The fatigue crack propagation rate, da/dN, versus stress intensity factor range, ΔK, is shown in Figs. 3.14(a-c). The as-received specimen, CT 1 (P_{max} = 4,000 N), exhibits only two stages (I and II) of the crack growth and the crack grew stable until failure at ΔK_f = 36.6 MPa$\sqrt{m}$. The slope of the regime II (also know as Paris regime) represents *m* from Equation (3.4) and is about 2.8, a value typical for ductile materials. The *C* parameter, from Equation (3.4), obtained by extending the slope line to ΔK = 1 MPa$\sqrt{m}$ is about $1.6 \times 10^{-7} \frac{\text{mm/cycle}}{\left(\text{MPa}\sqrt{\text{m}}\right)^{m}}$.

The presence of Zirconium hydrides influences the fatigue behavior for CT 2, which is shown in comparisons to CT 1 in Fig. 3.14(a). Unlike CT 1, the CT 2 specimen exhibits the typical three stages for crack growth behavior. During stage I the crack grows at slightly larger ΔK and slower crack propagation rates. For example, at ΔK = 13 MPa$\sqrt{m}$, da/dN for CT 2 is 3.3×10^{-5} mm/cycle while for CT 1 it is 7.9×10^{-5} mm/cycle. CT 2 has a shorter stage II crack growth behavior and the crack propagation rate is increased at the end of this stage. The failure occurred after the crack became unstable, during the stage III crack growth. The stress intensity factor range at failure is ΔK_f = 21.9 MPa$\sqrt{m}$, indicating that CT 2 exhibits a reduction in toughness. The slope for the Paris

regime gives m = 4.6 and C = 9.5 x 10^{-10} $\frac{\text{mm/cycle}}{\left(\text{MPa}\sqrt{\text{m}}\right)^{\text{m}}}$. A summary of the fracture toughness, m, and C values is shown in Table 3.4.

The fatigue crack growth behavior for CT 3 condition is presented in Figs. 3.14(b-c) in comparison to CT 1 and CT 2. These specimens, CT 3a and CT 3b, have a similar behavior with the as-received condition until the crack length reaches 22.86 mm, which is prior to the hydrogen charging. After the charging and under an applied load of 4,000 N, CT 3a breaks abruptly in one cycle, Fig. 3.14(b). Therefore, the test was continued on the second sample, CT 3b, with P_{max} = 1,300 N and the fatigue profile is shown in Fig. 3.14(b). It indicates the presence of only two stages, II and III, of the crack growth. It is worth noting the very small values for ΔK, about 7 MPa√m at the beginning of the Paris regime, which is close to the threshold value reported in Ref. [27].

Table 3.4 Summary of fatigue behavior: stress intensity factor range at failure, ΔK_f, m, and C for the three different cases studied, CT 1-3 specimens.

Specimen / Fatigue Behavior	CT 1	CT 2	CT 3
ΔK_f [MPa√m]	36.6	21.9	17.4
m	2.8	4.6	5.9
$C\left[\frac{mm/cycle}{\left(MPa\sqrt{m}\right)^{m}}\right]$	1.6 x 10^{-7}	9.5 x 10^{-10}	7.1 x 10^{-11}

The failure of the specimen occurs at $\Delta K_f = 17.4$ MPa$\sqrt{m}$, which indicates that CT 3 has the lowest toughness. The observed fatigue behavior for the CT 3 case after hydrogen charging, combined with the microscopic investigation, Fig. 3.13, suggests that the presence of hydrides plays a significant role on the mechanical behavior. Another possible influence on the fatigue curve profile could be an overloading effect due to the reduction in the applied load from 4,000 N to 1,300 N. However, calculations of ΔK, using Equation (1), a = 22.86 mm (the crack length when the hydrogen charging was employed), and P_{max} = 1,300 N, yields a ΔK = 7.78 MPa$\sqrt{m}$. Previous tests have showed that near threshold ΔK value is about 10.7 MPa$\sqrt{m}$. Therefore, under the current conditions, the crack would not propagate in the absence of the Zirconium hydrides. The obtained values for *m* and *C* are 5.9 and 7.1 x 10^{-11} $\frac{\text{mm/cycle}}{\left(\text{MPa}\sqrt{\text{m}}\right)^{m}}$, respectively. The observed variation of *m* and *C* values for the three cases, Table 3.4, is due to the reduction of toughness with the hydrogen content and the increase in the crack propagation rates. Thus, the slope for the Paris regime becomes steeper from CT 1 to CT 3.

The crack propagation rates for all the three cases are interesting to compare. First, at ΔK = 13 MPa$\sqrt{m}$, as discussed above for CT 1 and CT 2, the da/dN is on the order of 10^{-4} mm/cycle, whereas da/dN for CT 3 is about 2.9 x 10^{-4} mm/cycle. Another representative location is at ΔK = 16.5 MPa$\sqrt{m}$, which is the end of the Paris regime for CT 2. The crack growth rates increase from 3.2 x $10^{-4\ 3}$ mm/cycle for CT 1, to 5.6 x $10^{-4\ 3}$ mm/cycle for CT 2, and to 2.5 x 10^{-3} mm/cycle for CT 3. Thus, one can observe that at

both positions, CT 3 has one order of magnitude faster crack propagation rate even under the applied load of 1,300 N.

Finally, after failure, the fracture surfaces for each specimen were investigated by SEM. Figure 3.15(a) shows the fatigue curves, indicating the ΔK values at which SEM fractographs were taken in order to study the fatigue behavior and fracture surfaces. The fatigue striations spacing observed by SEM were compared at the given ΔK with the crack propagation rate, da/dN, obtained during the fatigue tests, Fig. 3.15(b). In the case of CT 1, the striation spacing values, represented by black rhombs, are very similar to the crack growth rates. For CT 2 and 3, fatigue striations could be found only in the localized area. The spacing for CT 2 is indicated by the magenta dot in Fig. 3.15(b), and for CT 3 by the blue square. Note that, for CT 3 specimen, the FCG 2, Fig. 3.10(d), fracture surfaces were investigated. A comparison of the fatigue striation spacing with the crack growth rate, Fig. 3.15(b), indicates the similarity for the CT 1 (as-received) condition, while the specimens containing hydrogen, CT 2 and 3, exhibit larger striation spacings.

Further, the fracture surfaces for the three specimens were investigated at the ΔK values shown in Fig. 3.15(a). For the CT 1 specimen, SEM fractographs are presented in Figs. 3.16(a-f) for stage I, II, and fast fracture, respectively. In addition, an example of the fatigue striations is shown in the inset of Fig. 3.16(b). This specimen exhibits a ductile behavior represented by the flat, featureless surface during the stage I crack growth and fatigue striations with spacings similar to the crack propagation rates, as shown in Fig. 3.15(b). The fast fracture shows the void coalescence, which is indicative of the ductile behavior as well. For the CT 2 case, the SEM images, Figs. 3.17(a-f), were taken at ΔK values similar to CT 1. It is worth noting that both Figs. 3.17(a) and (b)

correspond to the stage I crack propagation. The fatigue striations observed are presented as the inset for Fig. 3.17(c). The CT 2 specimen exhibits a brittle behavior with the interfacial fracture, dimples, cleavage-like facets, and secondary cracking. The fast fracture surface, Fig. 3.17(f), indicates a combination of voids and transgranular fracture, and, thus, brittle and ductile behavior. The SEM images for the CT 3 specimen are shown in Figs. 3.18(a-f) for stage II and III crack growth, and fast fracture, respectively. The inset of Fig. 3.18(b) represents the observed fatigue striations. This specimen also exhibits a brittle behavior with cleavage-like facets and secondary cracking. After failure, the fast fracture surface shows a transgranular fracture, indicating the brittle behavior, Fig. 3.18(f).

3.2.7 Effect of a homogenous hydrogen charging on fatigue behavior

The effects of hydride formation on Zircaloy microstructure, crack growth behavior, and fracture surfaces are discussed by comparing CT 1 and CT 2 specimens. When Zircaloy alloys transform from the β (bcc) to α (hcp) phase during the manufacturing processes, it develops a Basketweave Widmanstätten type structure [3]. The Basketweave structure is considered to be related to the presence of second phase precipitates and to their insolubility in the β-phase. In our case, the second phase precipitates are Fe-Cr [1]. These particles can act as nucleation sites for the Basketweave structure by initiating the formation of α-Zr plates [3, 28], and their location and density also serve as nucleation sites for the hydride phase [29]. Other possible trapping sites for hydrides to precipitate can be vacancies, dislocations, and micro-voids, as well. As it is visible in Fig. 3.13, the hydrides are precipitating at boundaries of the α-Zr plates within

the Zirconium grains. Moreover, the location of hydrides also coincides with the fracture path, as probed by SEM, influencing the fatigue behavior. This is consistent with what is observed in Ti alloys with Widmanstatten type structures, which exhibit a crack path very dependent on the microstructure [30]. As a result, a crack propagates along the α-plate boundaries through hydrides, leading to accelerated crack growth rates. Further, comparing the beginning of the fatigue life, stage I, for both specimens, Fig. 3.14(a), shows that in the case of CT 2 the crack propagates slower and at larger ΔK values. On the other hand, the SEM images taken at ΔK within stage I, Fig. 3.16(a) and Figs. 3.17(a-b), indicate that CT 1 has a flat, featureless fracture surface, typical of ductile alloys [23]. Contrary, CT 2 exhibits a rougher fracture surface. This behavior for CT 2 is caused by the presence of hydrides combined with the crack tip plasticity. At small ΔK values, such as ΔK = 13.26 MPa√m, and for large grains, 700 μm mean diameter, the plastic zone in front of the crack tip acts within the grain [31], affecting the zirconium plates, which are lifted out from the matrix, resulting in the observed rough brittle fracture surface. Consequently, the fracture surface roughness can be associated with an increase in the crack closure effect, which requires larger ΔK values for the crack to grow and slower propagation rates. The information about crack closure phenomena can be obtained by a linear fit of the load versus displacement curve, acquired for each cycle during the fatigue test. One can also calculate $\Delta K_{effective}$, as the difference between K_{max} and $K_{closure}$. Figure 3.19 shows the crack propagation rates as a function of the $\Delta K_{effective}$ for both specimens. It is clear that at the beginning of the fatigue life and in the absence of the crack closure effect, the CT 2 specimen exhibits crack propagation at smaller ΔK values and faster rates.

However, at greater ΔK values, in stage II, the fracture surfaces of CT 2 is smoother, Figs. 3.17(c) and (d). Subsequently, the crack propagates faster leading to the interfacial fracture and cleavage, as observed on the SEM images. This trend is due to the increase of the plastic zone size in front of the crack tip, which becomes larger than the grain size. The effect of brittle behavior for CT 2 specimen was also observed by studying the fatigue striation spacing for both specimens. The spacing between the fatigue striations is related to the blunting-sharpening sequence that a crack follows during the cyclic fatigue tests. For the as-received case, CT 1, the fatigue striation spacing is consistent with the fatigue crack propagation rates, while in the presence of zirconium hydrides, the crack propagates faster. Thus, there is not enough time for a complete blunting-sharpening sequence per fatigue cycle, leading to the observed difference between the crack propagation rate and striation spacing, Fig 3.15(b).

At even larger ΔK values, the crack propagation for CT 2 case becomes unstable, and the stage III crack growth is entered. The propagation rate of the crack is too fast to be significantly affected by the environment.

Therefore, the presence and location of the hydride phase in the bulk of Zircaloy plays a critical role on the fatigue behavior, by enhancing the crack propagation, leading to the interfacial fracture and reduced toughness.

3.2.8 Neutron diffraction residual strain measurements around the fatigue crack

Spatially-resolved strain measurements were performed on the as-received compact tension specimen, CT 1, using the Spectrometer for Materials Research at Temperature and Stress (SMARTS) instrument at the Los Alamos National Laboratory

[7]. The diffraction measurements were conducted around the fatigue crack tip, at crack length a = 22.86 mm for all three cases, as indicated schematically in Fig. 3.20. Note that CT 2 failed at the crack length of 23.98 mm under P_{max} = 4,000 N. Therefore, the magnitude of P_{max}, was reduced from 4,000 to 3,500 N to allow for the application of load during the in-situ neutron diffraction strain experiment. As a result, the fatigue tests were performed under P_{max} = 3,500 N, stopped when crack length *a* was 22.86 mm, and the area of interest in the crack tip region is indicated by "A" in Fig. 3.20. In addition, it is worth to be pointed out again that in the case of CT 3 specimen, the neutron diffraction measurement was performed after the specimen was fatigued crack growth to a = 22.86 mm and then charged with hydrogen, Fig. 3.20(d).

The elastic lattice strains were measured with neutron diffraction to determine the residual strain distribution around the crack tip. The measurement setup is indicated in Figs. 3.21(a) and (d) and a close up of the specimen in front of the neutron beam is shown in Fig. 3.21(b). The residual strain scanning was conducted along the crack, starting from 4 mm behind the crack tip to 20 mm in front of the crack tip, as indicated in Fig. 3.21(c, e). Figure 3.21(d) shows a schematic representation of the neutron-measurement setup. The two detector banks at the SMARTS instrument allow the measurements of two strain components, such as in-plane (IP, y direction, parallel to the fatigue loading direction) and through-thickness (TT, x direction, perpendicular to the fatigue loading direction) strain components, respectively. However, for brevity, in this dissertation only the IP residual strain component is presented. A cubic-shaped diffraction gauge volume was defined at the center of the specimen by using 2-mm radial collimators for the width of the diffracted beam, and 2-mm high and 2-mm wide incident beam. Note that within ± 2

mm from the crack tip, the incident beam height was reduced to 1 mm to achieve a finer spatial resolution along the crack length. The diffraction data were measured at a total of 21 positions along the crack as shown in Fig. 3.21(e). The lattice strains ε_a and ε_c along the a- and c-axes of the hexagonal-close-packed Zr-4 were obtained by Rietveld analyses [9] of the measured diffraction patterns, using General Structure Analysis System (GSAS) [8] and equation (4).

$$\varepsilon_a = \frac{a_i - a_0}{a_0} \quad \text{and} \quad \varepsilon_c = \frac{c_i - c_0}{c_0} \tag{3.6}$$

where a_i, c_i and a_0, c_0 are the lattice parameters *a* and *c* of the strained and unstrained conditions, respectively. The strained lattice parameters were measured from area around the fatigue crack tip. The strain-free lattice parameters, a_0 and c_0 were measured from a small Zr-4 piece of 20 x 30 x 6 mm^3 cut from the same ingot.

3.2.9 Effects of a pre-existing crack on the hydride distribution and subsequent fatigue behavior

Here we discuss the effects of a pre-existing crack and the associated residual strains on the fatigue behavior of Zircaloy by comparing the CT 3 specimen with CT 2 and CT 1 specimens. The residual strains develop around the fatigue cracks when the load is released, during the fatigue cyclic loading tests. Both CT 1 and 3 specimens were measured with neutron diffraction. Figure 3.22 presents the residual *a* and *c* lattice strain profiles for Zirconium in CT 1 condition, from 4 mm behind the crack tip to 20 mm in front of the crack tip. Both *a* and *c* axes show compressive (negative) strains at positions near the crack tip (- 4 to 1 mm) with balancing tensile (positive) strains, which reach a

maximum of 200 με at 2 mm in front of the crack tip. It should be noted the mostly compressive trend of the *c* lattice strain and the tensile tendency for the *a* lattice strain. The observed profiles for the residual lattice strain developed in the as-received specimen are consistent with that reported on stainless steel [32]. Further, the observed strain gradient at crack tip is expected to enhance the hydrogen diffusion, during the charging, towards the crack tip. This effect may be due to the tensile stress in front of the crack tip, which reduces the chemical potential of the hydrogen [33, 34]. In addition, when the lattice strain gradient and hydrogen diffusion is accompanied by lattice dilation, there is a mechanical relaxation associated with it, also known as the Gorsky effect [35, 36]. Consequently, the Zr lattice strain gradient is deriving a proportional hydrogen concentration at the crack tip. Therefore a higher hydride concentration upon precipitation takes place. As visible in Fig. 3.13, the concentration of hydrides in CT 3 specimen at the crack is greater than CT 2. The derived hydrogen at the crack during charging enhances the hydride effect on the fatigue behavior in the case of CT 3 specimen, which became more severe than for CT 2 case. Therefore, the localization of hydrides at the crack tip leads to an increase of the crack propagation rates and much reduced toughness. This effect is due to the circulation of the main crack through many more hydrides, reducing the time spent by the crack in the metal matrix, which has a higher toughness. The hydrides have very small fracture toughness of the order of 1 MPa√m [27]. Therefore, any load greater than this value will lead to the fracture of hydrides. The fatigue behavior curve, Fig. 3.13(d) showed that after H charging, CT 3 exhibits crack propagation even at $\Delta K = 7$ MPa√m under the applied load of 1,300 N.

Further, neutron diffraction measurements of residual lattice strain were also conducted on the CT 3 specimen to understand at the lattice level the mechanisms for the severe fatigue behavior of this specimen. In the presence of hydrides, the residual *a* and *c* lattice strains have a different profile, Fig. 3.23(a) and (b), respectively. The tensile trend of a-axis is enhanced reaching a maximum of about 500 με in front of the crack tip. Another observation is that the maximum tensile is extending to 4 mm in front of the tip. An opposite profile can be observed for the *c* lattice strain, Fig. 3.23(b). In the presence of hydrides, the c-axis of Zr does not show any strain gradient, exhibiting a relatively compressive trend. This behavior may be related to the location of hydrides on the zirconium lattice. The habit plane for zirconium hydrides is on the basal (*a*-*b*) plane of the hcp- Zr, which can produce extension of a-axis and compression of c–axis, similar with the experimental observation. However, to verify this behavior, development of a finite element model is required, which will be further explored in the future.

3.2.10 In-situ neutron diffraction measurements of the lattice strain evolution at the fatigue crack tip, under applied loads

A baseline had been established first, from the residual lattice strain evolution. Following that, in-situ spatially-resolved lattice strain measurements along the crack length were performed on CT specimens, at three different applied loads of 900 N, 1,800 N, and 2,700 N, using the load frame available on the SMARTS instrument. The setup of the specimen in the load frame, in front of the beam, is shown in Fig. 3.21. A crack opening displacement (COD) gage, Fig. 3.21(b) was used to monitor the bulk strain on the samples. The beam size of 2 x 2 x 2 mm^3 was employed. The in-situ lattice strain

measurement was conducted from 3 mm behind the crack tip to 14 mm in front of the tip, at a total of 13 positions, as indicated in Fig. 3.21(f). The lattice parameters of the hexagonal-close-packed Zr-4 were obtained by Rietveld analysis of the measured diffraction patterns, using GSAS.

A series of tensile loads of 900, 1,800, and 2,700 N were applied. In-situ lattice strain evolution around the fatigue crack was measured using neutron diffraction, for the three cases studied, CT 1, CT 2, and CT 3. The in-situ Zr *a* and *c* lattice strains development around the crack tip, under the applied loads, are presented in Fig. 3.24. For the as-received specimen, CT 1, the in-situ lattice strain evolution is plotted together with the residual lattice strain profile, Figs. 3.24(a-b), exhibiting strain gradients with maximum tensile in front of the crack tip. It is worth noting the systematic increase in the strain accumulated by both *a* and *c* axes in front of the crack tip, as the applied load is increased from 0 (residual strain) to 2,700 N. A qualitative evaluation of the two lattice strains shows that they have similar trends in front of the crack tip, reaching maximum of about 1,000 με under 2,700 N, at approximate 2 mm for *a* and 3 mm for *c*, ahead of the crack tip. However, the compressive strains in the awake of the crack are more severe for c-axis. In the case of CT 3 specimen (fatigued and H charged), lattice strain profiles have a different behavior, Figs. 3.24(c-d). The in-situ *a* lattice strain, under the applied load of 900 N, has a very similar trend with the residual *a* lattice strain, whereas when the load is increased to 1,800 N, and then to 2,700 N, there is a significant accumulation of tensile strain in front of the crack tip. The a-axis reaches a maximum of 1,600 με at 2 mm ahead of the tip, exhibiting a 600 με increased comparative to the CT 1 specimen. On the other hand, the *c* lattice strain shows little accumulation of strain under the applied loads.

For the 1,800 and 2,700 N cases, c-axis shows some maximum tensile strains of about 300 με at 3 mm in front of the crack tip, which is compared to CT 1.

The lattice strain trend for CT 2, Fig. 3.24(e-f), is similar to CT 3. However, the *a* lattice strain shows less localization in front of the crack tip, whereas the *c* lattice strain exhibits a strain gradient for each load. Under the load of 2,700 N, a and c axes reach a maximum tensile of about 1,500 με at 2 mm and 500 με at 3 mm in front of the tip, respectively.

Now, let us compare the lattice strain behavior for the three specimens. In the presence of hydrides, for CT 2 and 3, in comparison to CT 1, the *a* lattice strain exhibits enhanced tensile behavior in front of the tip, while *c* lattice strain develops a more compressive trend, suggesting that some mechanical relaxation occurs along c axis. Note that this trend is more severe for CT 3. Subsequently, the observed lattice strain evolution can be accompanied by a redistribution of stresses from zirconium matrix to zirconium hydrides. In the awake of the crack, c-axis is very similar for the three cases. However, the compressive strains exhibited by the a-axis in CT 1, became very close to zero strain for CT 2 and 3. In the case of CT 3, which was charged with hydrogen after the fatigue crack had been grown, this difference could be due to the effect of hydrogen on the crack's free surface available during charging. However, the CT 2, which was charged with hydrogen before the fatigue test, shows similar trends behind the crack tip.

To elaborate on the mechanisms responsible for the crack propagation in H-rich environments, one needs to make use of theoretical models. Based on the experimental observations of the fatigue crack propagation behavior and lattice strain evolution, and

the literature available on the subject, a discussion is offered regarding the crack propagation mechanism in the presence of hydrides.

Since the hydride phase is less dense (hydride density = 5600 kg x m^{-3}) than the matrix it replaces (zirconium density = 6511 kg x m^{-3}), the hydride can be under some form of constraint when it forms. In addition, the formation of hydrides is accompanied by a reported 17% increase in the volume, which leads to volumetric misfit. Due to the difference in the crystallographic structure, fcc for δ-ZrH_2 and hcp for Zr, there is an anisotropic volumetric misfit. Furthermore, it is known that the habit plane for hydrides is close to the basal plane, or within 20 degrees, of (0001) [27, 37], therefore the anisotropic misfit is causing the highest strain along any directions normal to (0001) [27, 38]. Subsequently, it produces expansion (tensile) effect on *a* lattice strain and compression on *c* lattice strain. The normal to basal plane (c–axis) should have the highest strain. However, *c* lattice strain shows strain relaxation under the applied loads, which could suggest that in fact, some of the strain was redistributed on the hydride phase existing along c axis. In turn, the hydrides, due to the very brittle nature at room temperature, with the reported fracture toughness of the order of 1 MPa√m [38], will break under any load greater than this value. Thus, the crack will propagate faster through the fractured hydride. The crack propagation is also favored by the behavior of a-axis, which accumulates significant tensile strains in front of the crack tip. Note that that strain in the hydride phase could not be measured using neutron diffraction. Therefore, a modeling scheme such as FEM is required to quantitatively investigate the loading partitioning between the Zr matrix and the hydride phase. A FEM study of plasticity deformation mechanisms can be inferred from the lattice strain measurements, which also incorporates

the effect of environment at the microstructure level. This is one of future research efforts that are suggested from the current dissertation.

Also, from the neutron diffraction pattern, one can obtain information regarding the presence and distribution of hydrogen/hydrides in the bulk. Examples of four neutron diffraction patterns, intensity versus d-spacing, are shown in Fig. 3.25(a). The patterns were collected at the center of specimens' thickness at 1 and 2 mm ahead of the crack tip, for CT 1 and CT 3. An increase in the background intensity for the sample charged with hydrogen is seen, due to the hydrogen incoherent scattering. The variation of background intensity, sum of counts, around the crack tip for the three cases, CT 1-3, is indicated in Fig. 3.25(b). It is observed that the background for CT 3 is the highest.

3.3 Neutron Scattering Measurements of Hydrogen Distribution in a Zircaloy-4 Alloy

3.3.1 Neutron incoherent scattering measurement of hydrogen

The studies were conducted on 50 mm long, 10 mm diameter round-bar specimens of Zr-4. The Zr-4 specimens were charged with hydrogen in a tube furnace at 703 K under 13.8 kPa pressure of 12.5 vol.% H-gas in argon mixture, for 30, 60, and 90 minutes. Neutron incoherent scattering measurements were conducted on the hydrogenated bars using the fixed-incident energy (E_i=14.6 meV) triple-axis spectrometer, HB1A instrument, Fig. 3.26(a), at High Flux Isotope Reactor (HFIR), at Oak Ridge National Laboratory [39]. The neutron beam size was defined by boron carbide masks placed in the front (30 mm height x 16 mm width), and behind the samples

(35 mm height x 21 mm width), Fig 3.26(b). To determine the total amount of hydrogen in the Zr-4 samples, the increase in the incoherent scattering with the hydrogen content was calibrated using samples with known hydrogen content. The significant and uniform increase in background of the diffraction spectra is due to the large incoherent cross-section of H (σ_H^{incoh} = 79.9 barn) compared to that of zirconium (σ_{Zr}^{incoh} = 0.02 barn) [40, 41]. A polypropylene film with a thickness of 0.02 mm was cut into 40 mm x 50 mm sheets. These sheets, in sets of three, from 0 to 27 sheets, were successively wrapped around the as-received Zr-4 specimen. Thus, by increasing the number of polypropylene sheets, an increase of hydrogen content in the Zr-4 specimen was simulated. The amount of the hydrogen in each sheet was calculated from its weight and chemical formula. Neutron energy scans were performed on calibration samples, within an energy transfer range from -1.5 meV to 1.5 meV, with a step of 0.2 meV, and a counting time of 60 seconds per point. These incoherent scans were taken at a fixed two-theta angle (2θ = 62 deg., λ = 2.367 Å) where no coherent scattering was present. Using an identical procedure, inelastic scans were carried out on the gas-hydrogenated Zr-4 specimens. The total hydrogen content, averaged over the bulk of each charged specimen, was then estimated.

3.3.2 Neutron incoherent scattering results

The cross-sectional fracture surface of a tensile tested Zr-4 specimen, charged with H gas for 60 minutes at 703 K, is shown in Fig. 3.27(a). A ring shaped layer, with a thickness of about 400 μm, is observed at the surface. Dotted lines mark the apparent outer and inner edges of this layer, shown below to be zirconium hydride. The micro-

Vickers hardness profile of the 60-min specimen is shown in comparison to that of the as-received specimen in Fig. 3.27(b). The results show a sharp increase in the hardness profile in the hydrogenated specimen, near the edge, due to the presence of the hydride layer. Neutron diffraction patterns of the as-received Zr-4 and the hydrogenated specimens measured at the HB1A instrument are presented in Fig. 3.28. A Rietveld structure refinement of the shown diffraction profiles revealed the presence of H in the sample in the form of face-centered-cubic delta zirconium hydride, δ-ZrH_2. This is consistent with Couvreur's report [42], which showed the diffraction peaks of δ-ZrH_2 when the hydrogen desorption from a cladding tube was studied in-situ. Fig. 3.28 clearly shows a systematic (volume-averaged) increase in the δ-ZrH_2 hydride peak intensities, and a corresponding decrease in the Zr peak intensities, with increasing hydrogenation time. In addition to the presence of δ-ZrH_2 peaks, the backgrounds of the diffraction patterns of the hydrogenated specimens exhibited a significant and systematic increase with the increase in the charging time, due to the effect of the large incoherent scattering from H. The increase in incoherent scattering also correlates with an increase in attenuation of the intensities of the ZrH_2 peaks.

In order to quantify the observed changes in the incoherent scattering with the H content, measurements were performed on the calibration specimens, and a systematic increase in the intensity with the number of the polypropylene sheets was observed. The sum of counts in the Zr-4 sample was I_0 = 7,569. For the sample plus propylene sheets (0 to 27), the intensities were used for calibration by fitting (R = 99%) to the functional form [43]:

$$I = I_0 + A[1 - \exp(-c/c_0)] \tag{3.7}$$

where c is the H mass fraction. A = 81,000±3,900, and c_0 = 2.71 ± 0.23 are the least squares fitting parameters. The calibration curve obtained from this fit is represented as a solid (red) curve, i.e., sum of neutron counts versus the number of polypropylene sheets (upper x-axis), in Fig. 3.29(a). Each polypropylene (C_3H_6) sheet exposed to the neutron beam contains m = 2.79 mg of hydrogen. Since the mass of the zirconium specimen irradiated was about M =15.85 g, it is estimated that for a specimen with one sheet of polypropylene, the hydrogen mass fraction, c = m/M, is approximately 176 ppm. As a result, the relationship between the number of polypropylene sheets (upper x-axis) and the hydrogen content (lower x-axis) is established for the calibration samples, as shown in Fig. 3.29(a). For small values of H mass fraction, c, where the total neutron attenuation (multiple scattering and absorption) is dominated by the matrix, the scattered intensity is expected to depend linearly on the H content. However, as Kvardakov *et al.* [43] showed, that at high H mass fractions (about 1,000 ppm), hydrogen attenuation gives rise to additional attenuation of the beam within the sample, and a saturation effect is expected to appear in the experimental curve. Indeed, the measured incoherent scattering starts to deviate from a linear behavior above 500 ppm.

Subsequently, measurements were performed on the hydrogenated Zr-4 bars using the same experimental condition. Fig. 3.29(b) shows the increase in the incoherent scattering intensities with the increase in the charging time (i.e., increase in the H content). The measured sums of counts for the hydrogenated specimens are shown as open circle in Fig. 3.29(a). The calibration curve (solid red line in Fig. 3.29(a) was used to determine the total hydrogen content in the hydrogen-charged samples by substituting the measured intensities into Equation (3.8):

$$c = -c_0 \ln\{1 - [(I - I_0)/A]\} \quad (3.8)$$

The specimen charged with H gas for 30 minutes at 703 K contains a total volume-averaged H of about 1,600 ppm, while the 60-minute and 90-minute specimens contain about 2,800 ppm and 5,200 ppm hydrogen, respectively.

3.3.3 Neutron radiography imaging measurements

The synergetic effect of applied stresses with formation and distribution of the hydrides around a crack-tip was explored using neutron imaging at the National Institute of Standards and Technology (NIST), using the Neutron Imaging Facility (NIF) [44]. In particular, neutron imaging, such as radiography and tomography, can take advantage of the significant difference in the total cross sections of Zr σ_{scatt} = 6.46 barn and H σ_{scatt} = 82.06 barn [40], which gives different effect on the beam attenuation, creating imaging contrast.

The three cases, CT 1, CT 2, and Ct 3, were measured by the neutron radiography in an attempt of reconstructing the 3-D neutron tomography image. This technique consists of a complete 3-dimensional imaging of the object's composition, by rotating it 180 degrees and taking neutron radiographs at defined angular positions. Each CT specimen was placed between the neutron beam and a low-resolution detector (200 μm resolution), and a radiograph image of the entire specimen was recorded every 0.2 degree to fully reconstruct the 180 degrees. The measurement setup is shown in Fig. 3.30(a). A total of 901 radiographic images were obtained for each specimen.

Using the high-resolution detector (10 μm resolution), Fig. 3.30(b), the radiography of the crack tip area is recorded. The imaged region is indicated by the shaded area in the schematic in Fig. 3.30(c).

The hydride distribution in Zircaloy-4 has been visualized using high-resolution neutron radiography. Figure 3.31 shows the radiographic images for the three situations studied. In the case of as-received condition, CT 1, there is not much visible contrast on the specimen, Fig. 3.31(a). Since this specimen is a single phase, Zirconium without any hydrogen, no contrast would be expected. The CT 2 shows a dark contrast at the bottom of the machine notch, which might be due to the formation of hydrides in this area prior fatigue testing, Fig. 3.31(b). Darker areas within the specimen can also be seen, which are indicative of rather homogenous distribution of hydrides. On the other hand, CT 3 shows a clear contrast at the bottom of the notch and along the crack, Fig. 3.31(c). This is the only specimen to show the crack profile, although all three specimens have a fatigue crack. This observation is due to the localization of hydrides along the crack for CT 3, which had a pre-existing fatigue crack during the hydrogen charging, while CT 2 has first charged and then fatigue tested. In the absence of hydrogen, there is no observable crack, within the instrument's resolution limit.

REFERENCES

1. www.wahchang.com, Wah Chang Company, *Technical Department.*

2. G. F. V. Voort, "*Metallography, Principles, and Practice*", (1984): pp. 701.

3. R. A. Holt, J. of Nucl. Mater., 35 (1970): pp. 322-334.

4. S. Matthies, J. Pehl, H. –R. Wenk, L. Lutterotti, and S. C. Vogel, J. Appl. Cryst. Vol. 38, no. 3, (2005): pp. 462-475.

5. H.-R. Wenk, L. Lutterotti, and S. Vogel, "*Texture analysis with the new HIPPO TOF diffractometer"*, Nuclear Instruments and Methods in Physics Research A 515 (2003): pp. 575–588.

6. S. C. Vogel, C. Hartig, L. Lutterotti, R. B. Von Dreele, H –R Wenk, and D. J. Williams, "*Texture measurements using the new neutron diffractometer HIPPO and their analysis using the Rietveld method"*, Powder Diffraction, 19 no.1 (2004): pp. 65-68.

7. M.A.M. Bourke, D.C. Dunand, and E Üstündag, "*SMARTS - A Spectrometer for Strain Measurement in Engineering Materials"*, Applied Physics A, vol. 74 (SUPPL.II), (2002): pp. S1707-S1709.

8. A. C. Larson and R. B. Von Dreele, "*General Structure Analysis System (GSAS)"*, Los Alamos National Laboratory Report LAUR, (2004): pp. 86-748.

9. H. M. Rietveld, J. Appl. Cryst., 2, (1969): pp. 65-71.

10. R. B. Von Dreele, J. Appl. Cryst., 30, (1997): pp. 517-525.

11. B. Clausen, C. N. Tomé, D. W. Brown, and S. R. Agnew, "*Reorientation and Stress Relaxation due to Twinning: Modeling and Experimental Characterization for Mg"*, submitted to Acta Mater., (2007).

12. J. W. L. Pang, T. M. Holden, P. A. Turner, and T. E. Mason, Acta Mater., 47, no. 2 (1999): pp. 373-383.

13. S. R. Agnew, C. N. Tomé, D. W. Brown, T. M. Holden, and S.C. Vogel, Scripta Mater., 48, (2003): pp. 1003–1008.

14. F. Xu, R.A. Holt, and M.R. Daymond, J. of Nucl. Mater. 373 (2008): pp. 217–225.

15. P. A. Turner and C. N. Tomé, Acta Metall. Mater. 42, no. 12 (1994): pp. 4143-4153.

16. P. A. Turner, N. Christodoulou, and C. N. Tomé, International. J. of Plasticity, 11, no. 3 (1995): pp. 251-265.

17. E. Tenckhoff, "*Deformation Mechanisms, Texture, and Anisotropy in Zirconium and Zircaloy"*, (1988).

18. ASTM Standard E647-86, "*Annual Book of ASTM Standards",* Philadelphia, PA 3.01 (1986), pp. 714-36.

19. J. Harris and S. Andersson, Phys. Rev. Lett., 55 (1985): pp. 1583-1586.

20. ASTM Standard B 811, "*Standard Specification for Wrought Zirconium Alloy Seamless Tubes for Nuclear Reactor Fuel Cladding".*

21. H. Tada, P. C. Paris, and G. R. Irwin, "*The stress analysis of cracks handbook"*, (1985).

22. L. J. Chen, P. K. Liaw, R. L. McDaniels, and D. L. Klarstrom, Metal. and Mater. Trans. A, 34 A (2003): pp. 1451-1460.

23. S. Suresh, *"Fatigue of Materials",* 2nd Edition, (1998).

24. ASTM Standard E 562, "*Standard Test Method for Determining Volume Fraction by Systematic Manual Point Count"*, (2002).

25. http://www.mse.mtu.edu.

26. R. Dutton, K. Nuttall, M. P. Puls, and L. A. Simpson, Metal. Trans. A, 8A (1977): pp. 1553 - 1562.

27. L. A. Simpson, and M. P. Puls, Met Trans., 10A (1979): pp. 1093.

28. V. Quach and D. O. Northwood, Metalography, 17 (1984): pp. 191-201.

29. G. Bertolino, G. Meyer, and J. P. Ipina, J. of Nucl. Mater., 320 (2003): pp. 272-279.

30. A. W. Funkenbush and L. F. Coffin, Metal. Trans. A, 9A, (1978): pp. 1159- 1167

31. R. W. Hertzberg, "*Deformation and Fracture Mechanics of Engineering Materials"*, 4th Ed., (1996).

32. Y. Sun, H. Choo, P. K. Liaw, Y. Lu, B. Yang, D. W. Brown, and M. A. M. Bourke, Scripta Mater., 53 (2005): pp. 971-975.

33. H. K. Birnbaum and P. Sofronis, Mater. Sci. and Eng. A 176 (1994): pp. 191-202.

34. J. Lufrano, and P. Sofronis, Acta Mater., 46 no. 5 (1998): pp. 1519-1526.

35. W. S. Gorsky, Phys. Zeitschr. Sowjetunion 8 (1935): pp. 457.

36. H. Numakura, Solid State Phenomena, 89 (2003):pp. 93-114.

37. J. Lufrano, P. Sofronis, and H. K. Birnbaum, J. Mech. Phys. Solids, 46 (1998): pp. 1497-1520.

38. S. Sagat, S. Q. Shi, and M. P. Puls, Mater. Sci. and Eng. A, 176 (1994): pp. 237-247.

39. Details of HB1A are available at http://neutrons.ornl.gov.

40. "*Neutron Data Booklet*", Insitute Laue-Langevin, 2nd Ed.

41. A. D. Krawitz, "*Introduction to Diffraction in Materials Science and Engineering"*, (2001): pp. 389.

42. F. Couvreur and G. Andre, "*In-Situ Neutron Scattering Study of Hydrogen-Containing Zircaloy-4 Alloys*", in LLB Scientific Report (1997-1998): pp.723.

43. V. V. Kvardakov, H. H. Chen-Mayer, and D. F. R. Mildner, *J. Appl. Phys.*, 83, 7 (1998): pp. 3876-3879.

44. Details of NIF at http://physics.nist.gov/MajResFac/NIF/index.html.

APPENDIX

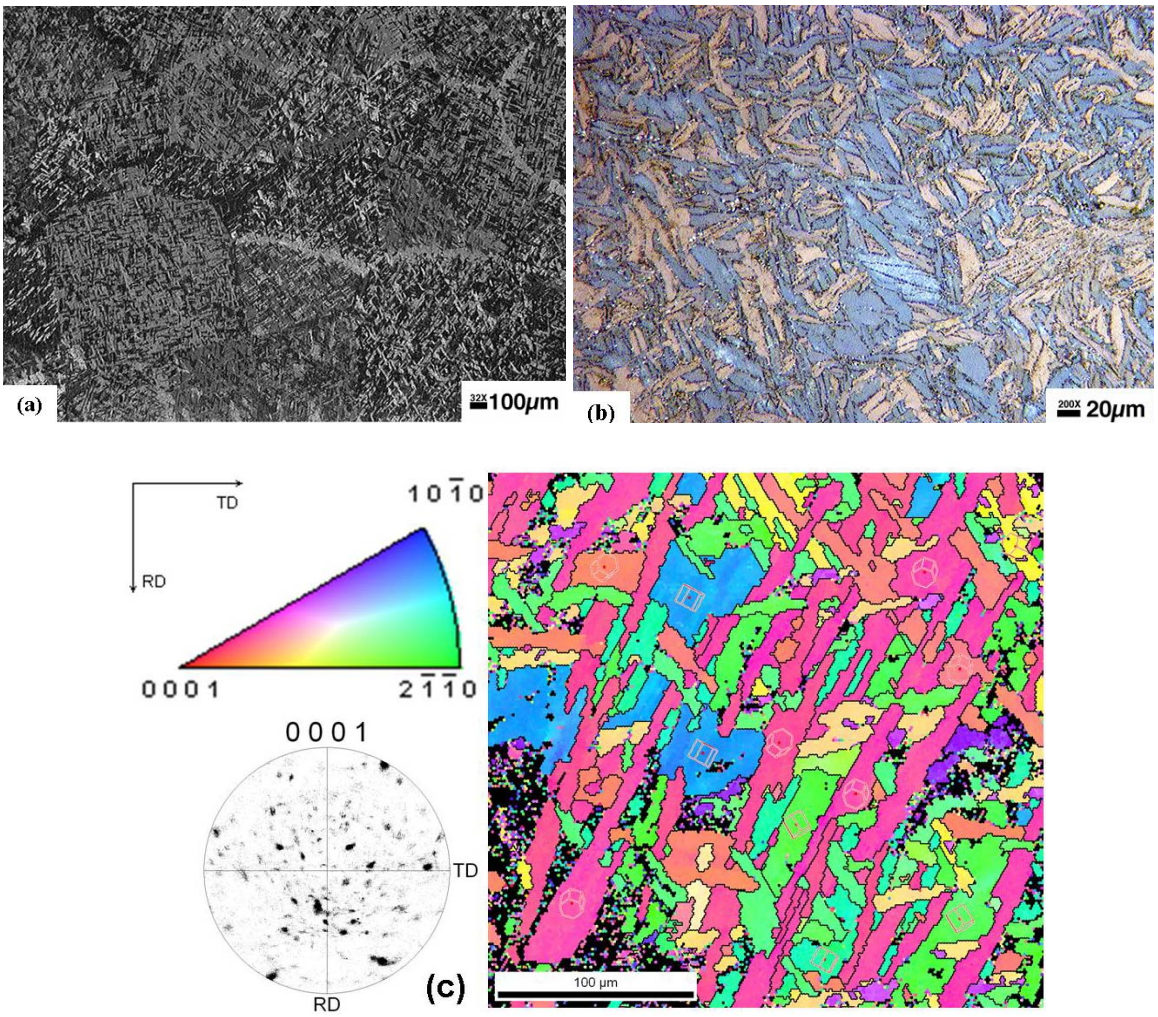

Figure 3.1 Polarized light optical microstructure of mechanically polished and etched Zircaloy-4 a) showing the Basketweave Widmanstätten type structure including the former β-Zr grains with a mean diameter of approximately 700 μm; b) magnified view of the Basketweave structure showing the α-Zr plates. (c) (right) electron backscatter diffraction (EBSD) image represents the [0001] inverse pole figure of the surface normal, via the color-coded stereographic triangle (left). It indicates the orientation of α-Zr plates and the [0001] pole figure relative to x-y axes of the specimen. Dark regions are due to distorted lattices.

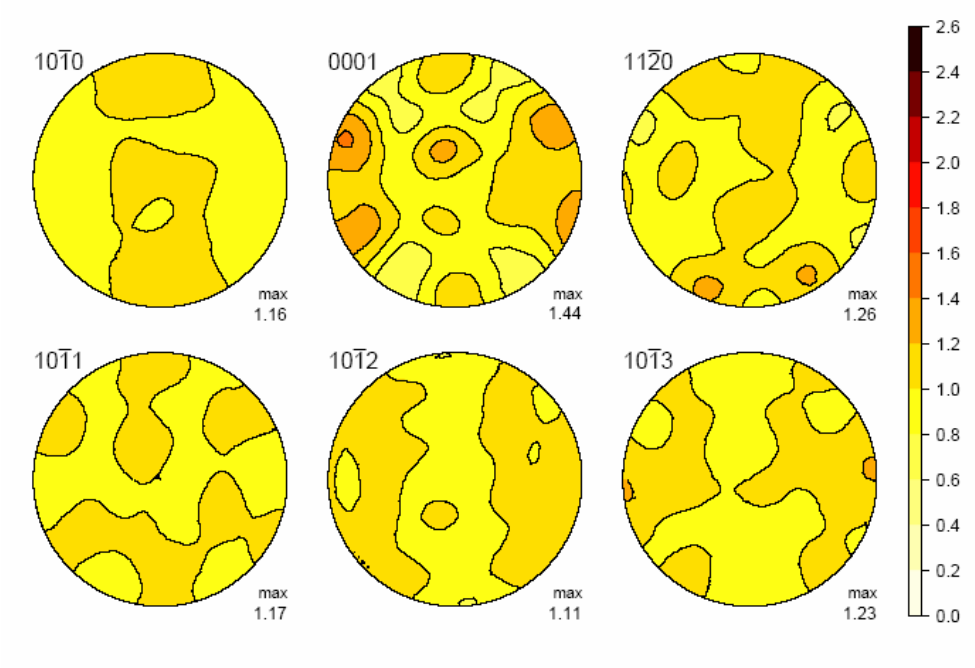

Figure 3.2 Initial texture of the as-received Zircaloy-4 measured with the HIPPO instrument, without any symmetry assumptions. The loading axis is at the center of pole figure.

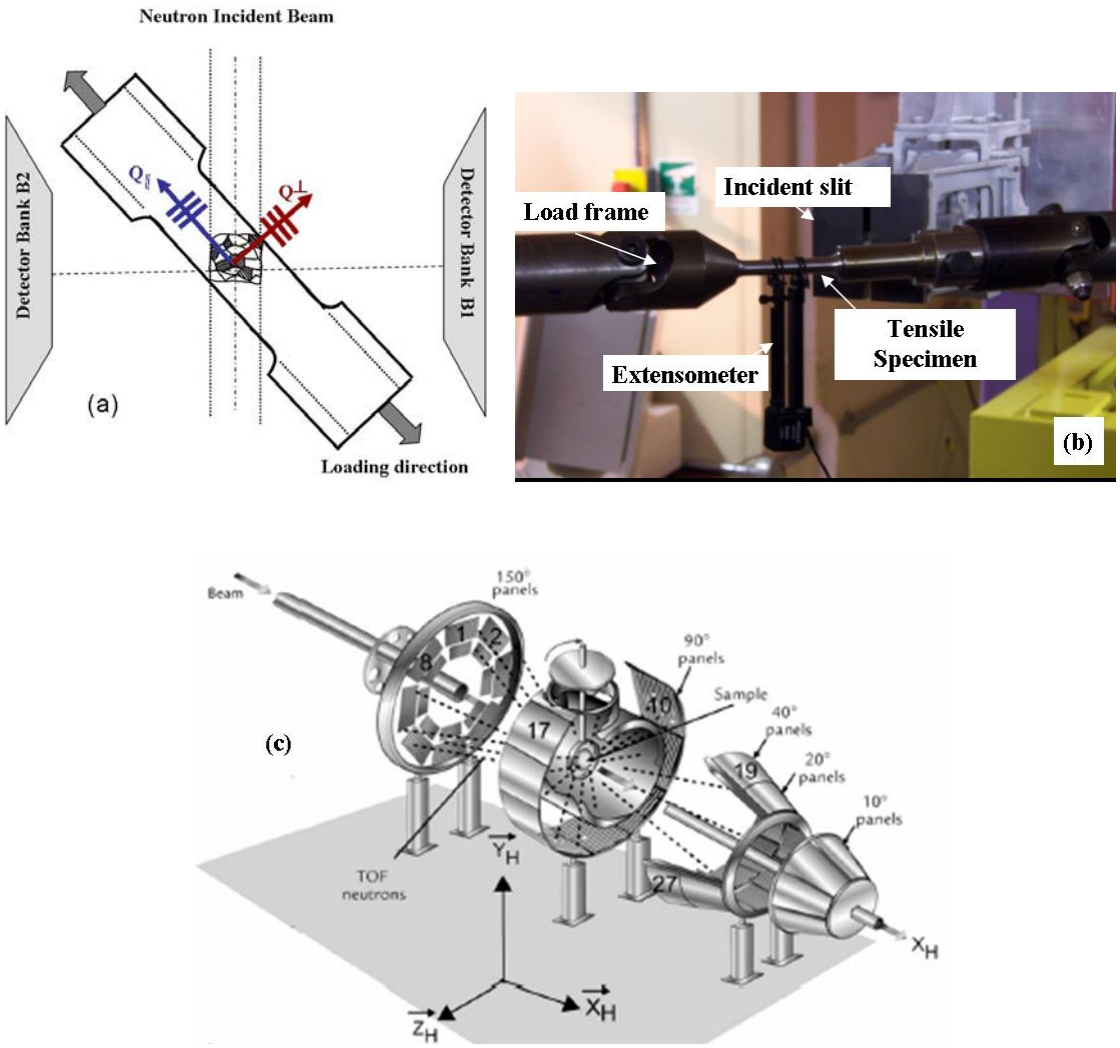

Figure 3.3 Schematic representation of the in-situ neutron diffraction experiment setup at the SMARTS instrument. The uniaxial tensile loading direction, and the detector banks positions, allow strain measurement in longitudinal (plane normal parallel to the loading direction, $Q_{\parallel}$) and transverse (plane normal perpendicular to the loading direction, $Q_{\perp}$) directions, (b) the picture shows the tensile specimen mounted in the load frame in front of the beam with an extensometer attached; (c) schematic of HIPPO instrument for texture measurement.

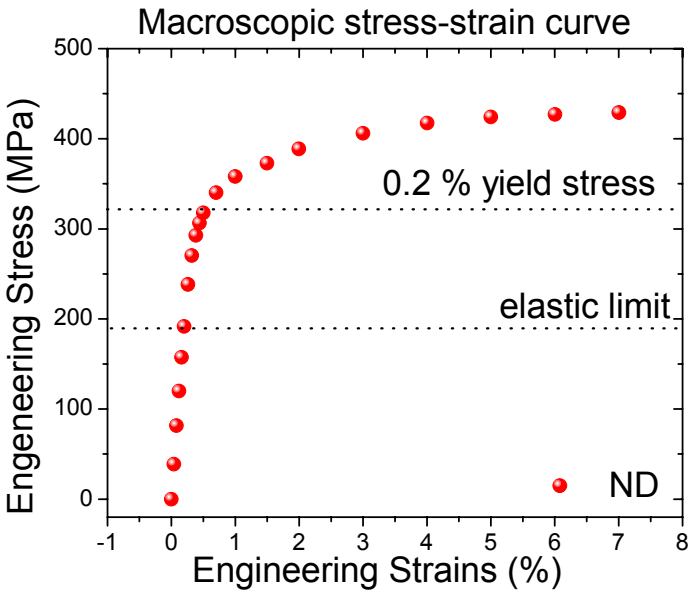

Figure 3.4 Macroscopic tensile stress-strain curve measured during the neutron diffraction (ND) experiment. The engineering stress on the y axis is obtained as time average stress.

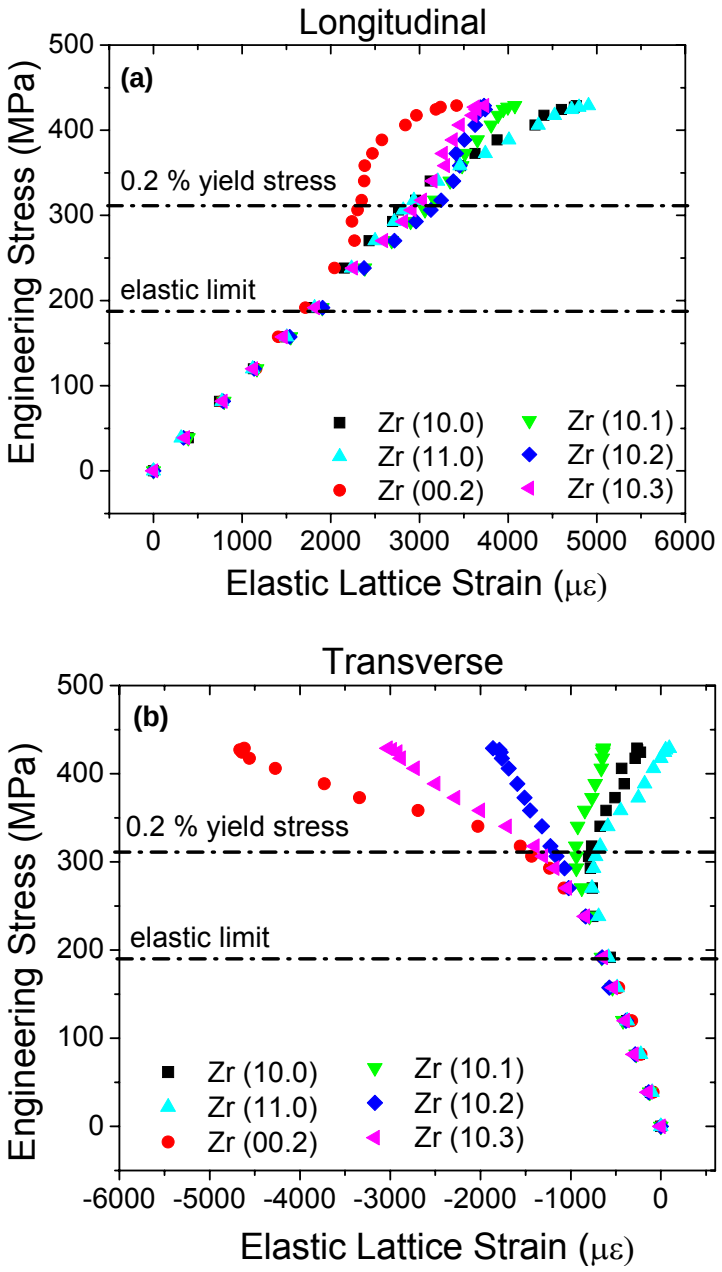

Figure 3.5 The neutron diffraction (ND) – measured - elastic lattice strain evolution under the applied tensile load for (a) longitudinal and (b) transverse directions, showing the elastic-plastic anisotropy.

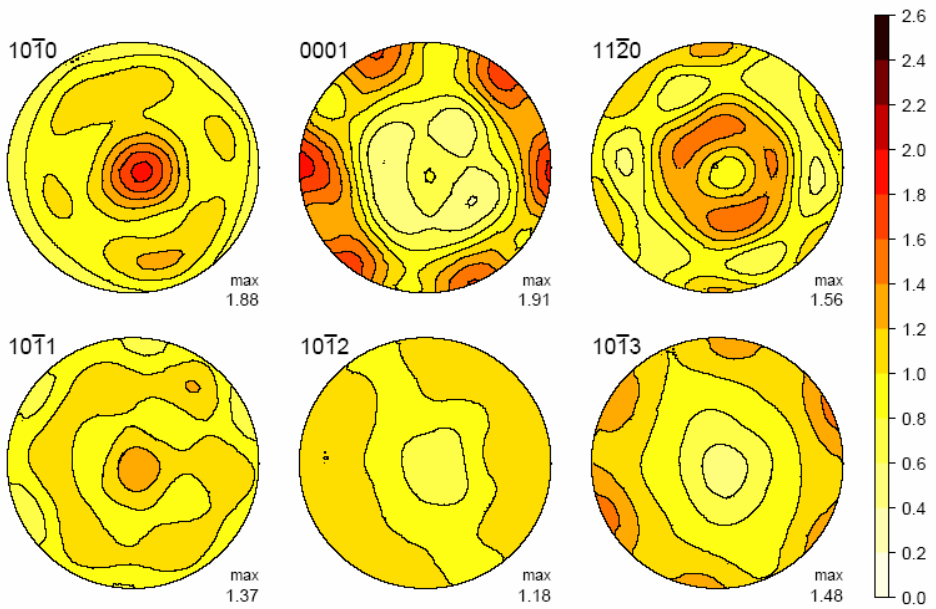

Figure 3.6 The texture developed under the applied load at the end of the tensile test (7 % total strain), measured using the HIPPO instrument.

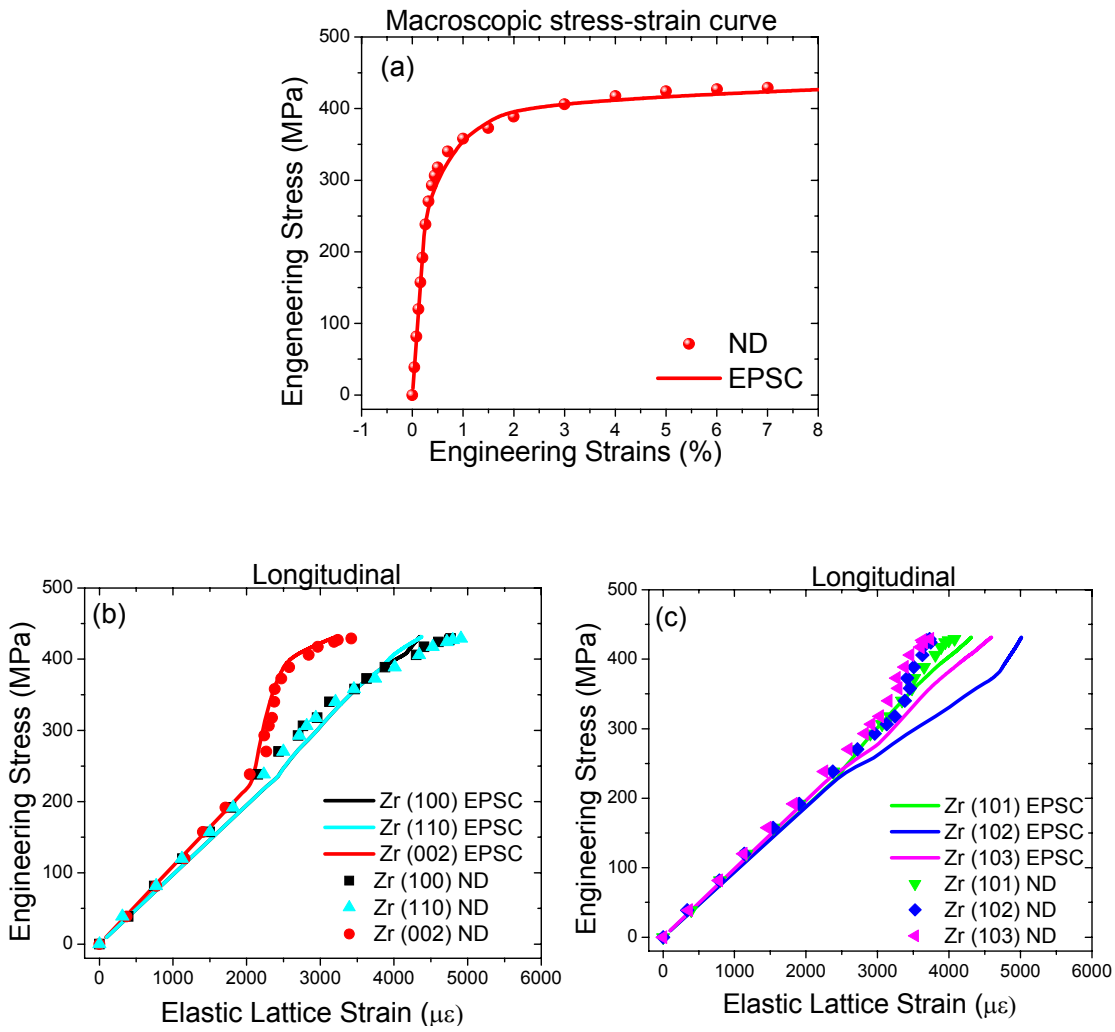

Figure 3.7 Case 1: Neutron diffraction (ND) data and the EPSC calculation, considering the combination of the slip systems listed in Table 3.1. (a) Macroscopic stress- strain curve. Lattice strain evolution under applied load in longitudinal direction (parallel to the loading axis) for (b) the basal and two prism planes, and (c) three pyramidal planes.

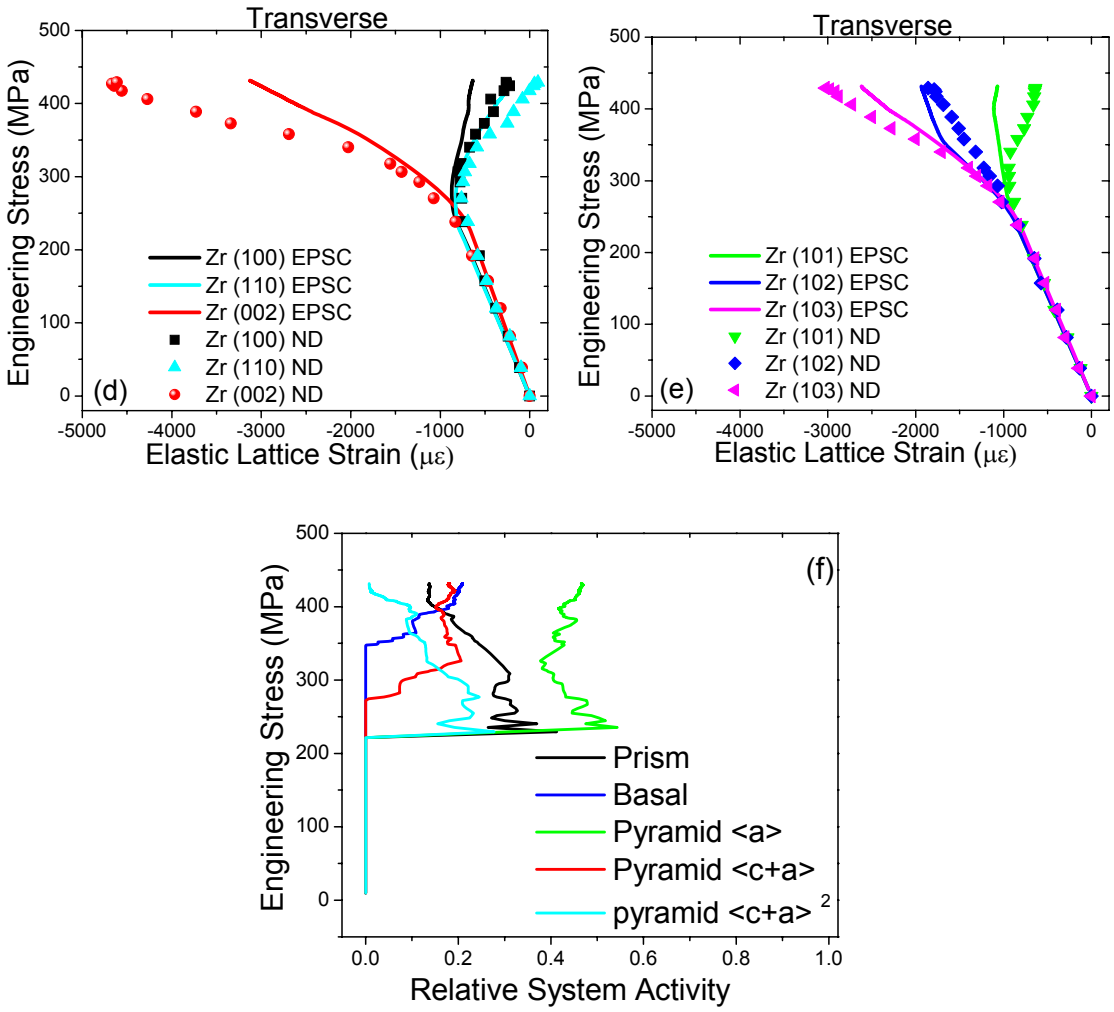

Figure 3.7 (continued) Lattice strain evolution under applied load in transverse direction (perpendicular to the load axis) for (d) the basal and two prism planes, and (e) three pyramidal planes. (f) Predicted relative system activity developed under the applied stress.

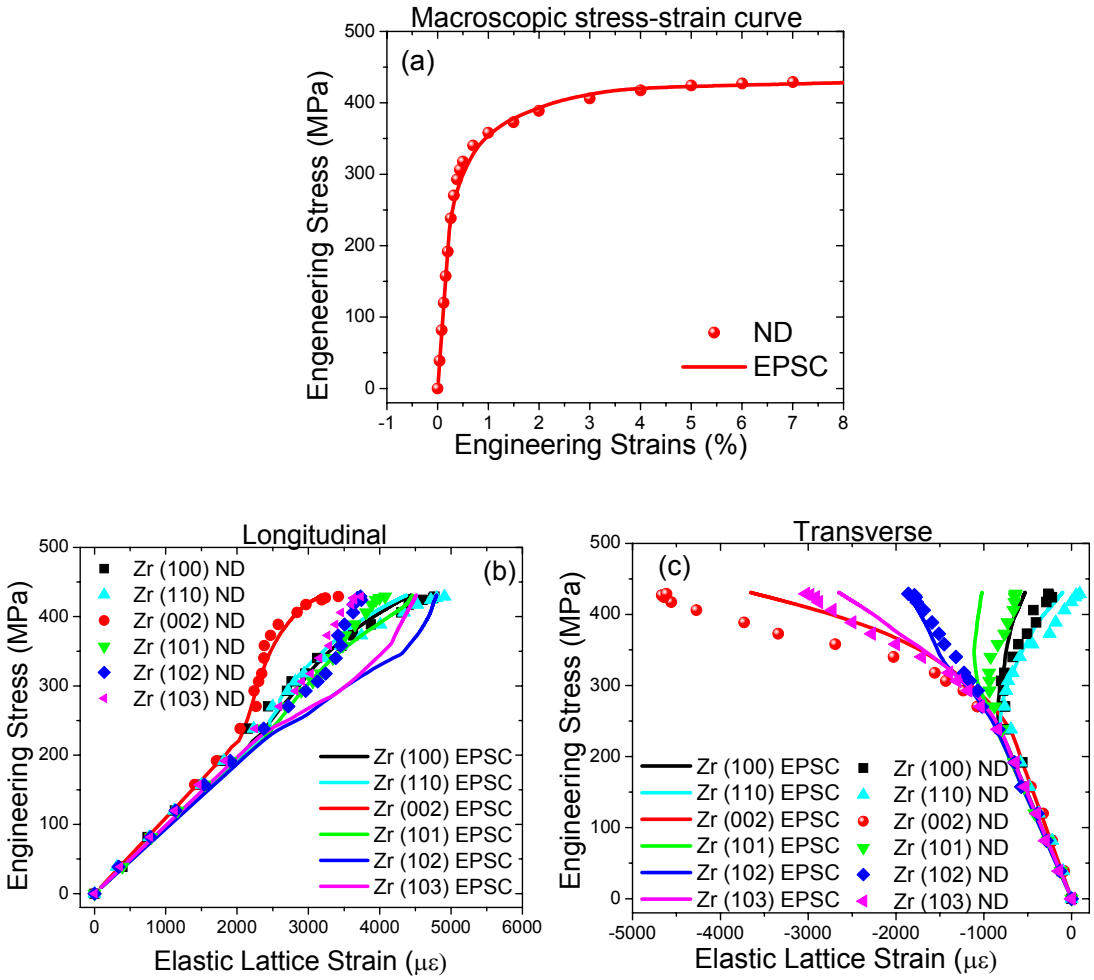

Figure 3.8 Case 2: Neutron diffraction (ND) data and the EPSC calculation considering active the combination of slip systems and tensile twinning listed in Table 3.2. (a) Macroscopic stress-strain curve. Lattice strain evolution under applied load in longitudinal direction (parallel to the loading axis) for the basal, prism, and pyramidal planes (b), and transverse direction (perpendicular to the load axis) for the basal, prism, and pyramidal planes(c).

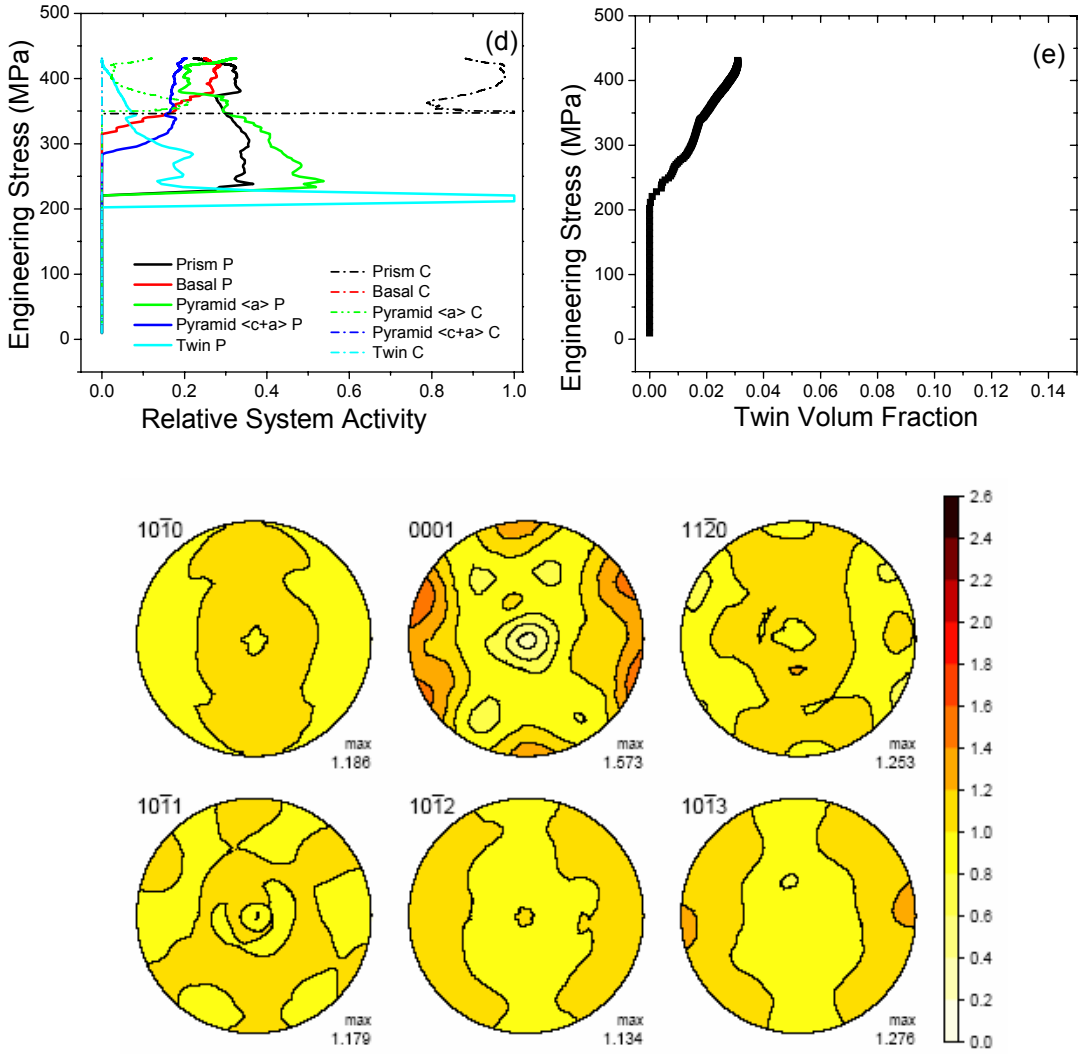

(f)

Figure 3.8 (continued) (d) Predicted relative system activity developed under the applied stress. The continuous lines are for the parent grains and the dashed lines are for the twin grains. (e) The calculated final twin volume fraction developed under the applied stress. (f) Predicted texture developed due to the 3% final twinning volume fraction at the end of tensile test.

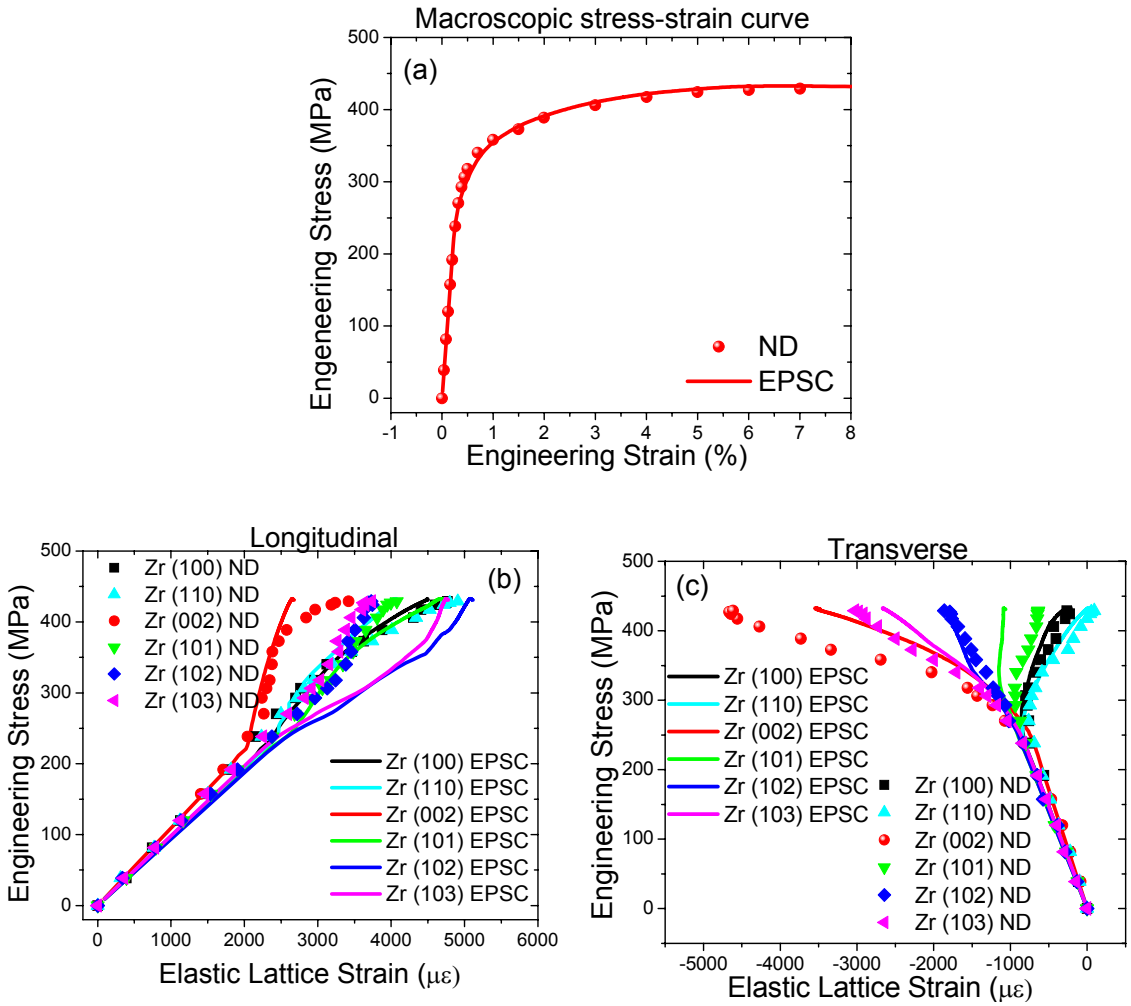

Figure 3.9 Case 3: Neutron diffraction (ND) data and the EPSC calculation considering the combination of the slip systems active and significant tensile twinning activity, listed in Table 3.3. (a) Macroscopic stress-strain curve; and the lattice strain evolution under applied load in (b) longitudinal direction (parallel to the loading axis) for the basal, prism, and pyramidal planes, and (c) transverse direction (perpendicular to the load axis) for the basal, prism, and pyramidal planes.

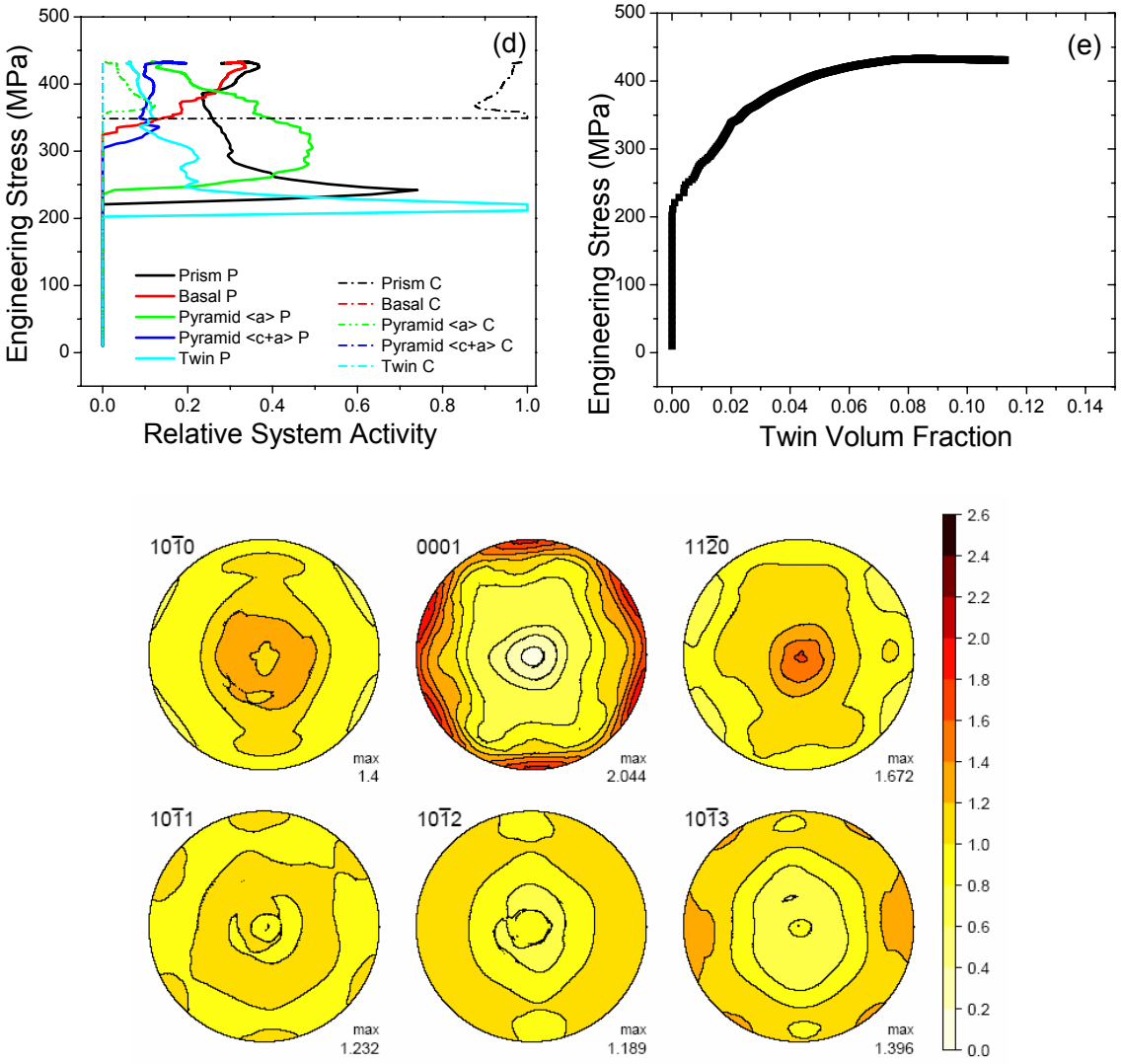

(f)

Figure 3.9 (continued) (d) Predicted relative system activity developed under the applied stress. The continuous lines are for the parent grains and the dashed lines are for the twin grains. (e) The calculated final twin volume fraction developed under the applied stress. (f) Predicted texture developed due to the 12% final twinning volume fraction at the end of tensile test.

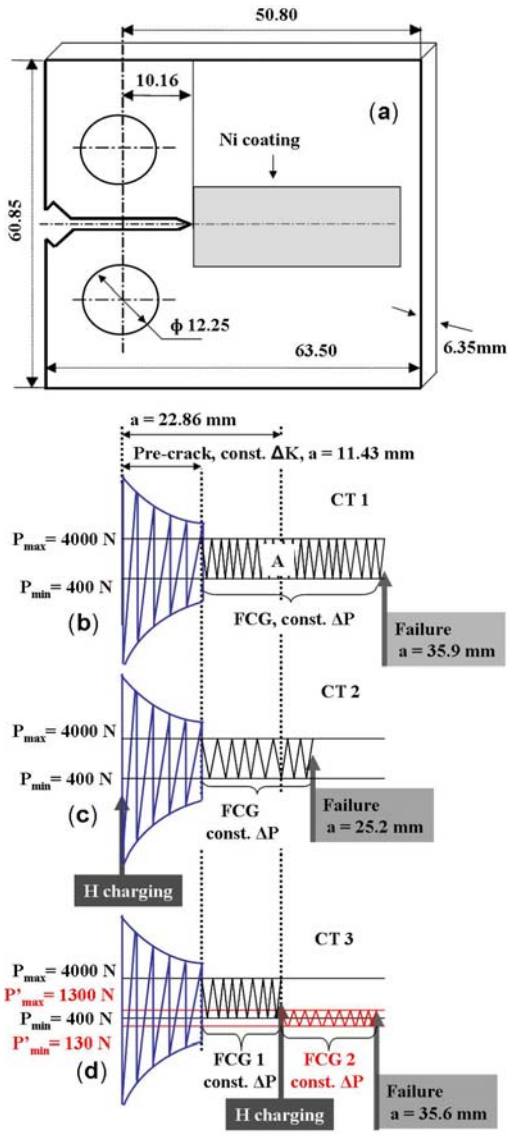

Figure 3.10 CT specimen dimensions and preparation steps: (a) Schematic of compact-tension (CT) specimen; (dimensions are in millimeters). The area coated with nickel for hydrogen (H) charging is also indicated. The fatigue pre-cracking, crack growth, and H charging steps for the 3 different cases are shown in: (b) CT 1: fatigue of the as-received specimen, FCG denotes fatigue crack growth; (c) CT 2: H charged and fatigued, and (d) CT 3: fatigued to a = 22.86 mm, P_{max} = 4,000 N, H charged, and continued to be fatigued (FCG2) with P_{max} = 1,300 N.

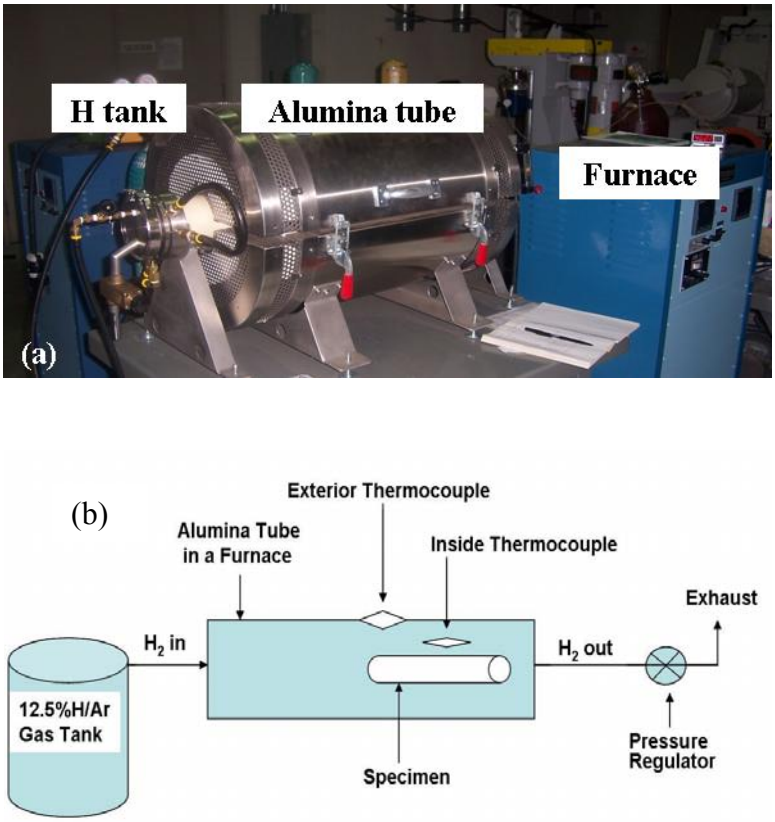

Figure 3.11 Hydrogen charging setup (a) picture and (b) schematic of the system.

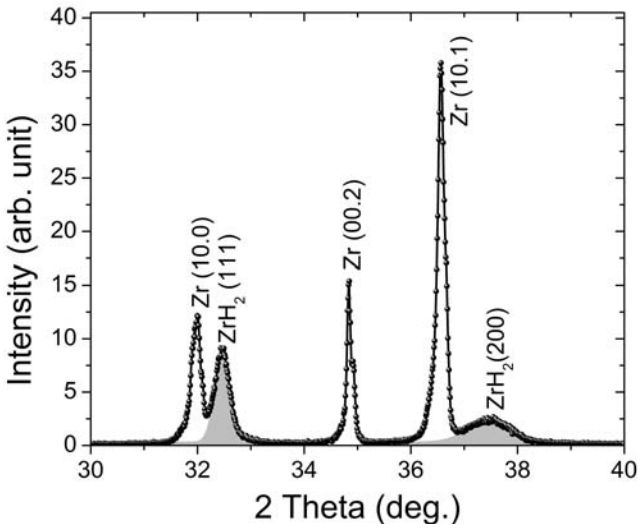

Figure 3.12 A typical x-ray diffraction pattern from the surface of an hydrogen charged specimen. Three zirconium reflections Zr $(10\bar{1}0)$, Zr (0002), and Zr $(10\bar{1}1)$ and two zirconium hydride peaks ZrH_2 (111) and ZrH_2 (200) were identified. The hydride peaks corresponds to δ-ZrH_2.

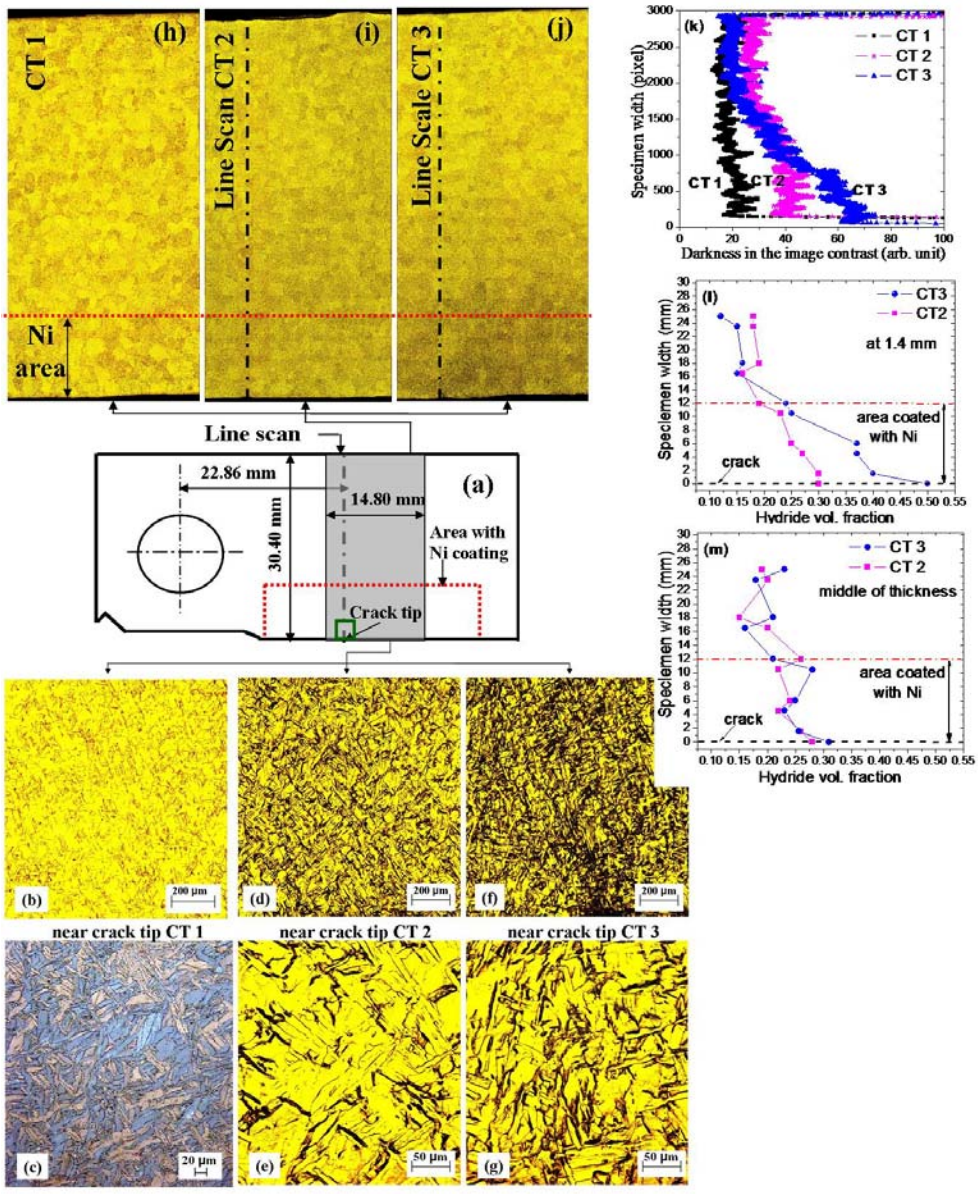

Figure 3.13 Optical microstructures of the 3 cases studied: CT 1, CT 2, and CT 3. a) Schematic of upper half of the CT specimen. The green square at the crack tip indicates the location for the low mag. micrographs in (b–d-f) and at higher mag. in (c–e-g). The gray shaded area of the 3 specimens is shown in (h–j). The image contrast result is shown in (k). Image in (c) is taken under polarized light. Variation in hydride volume fraction at (l) 1.4 mm from the surface and (m) middle of the thickness.

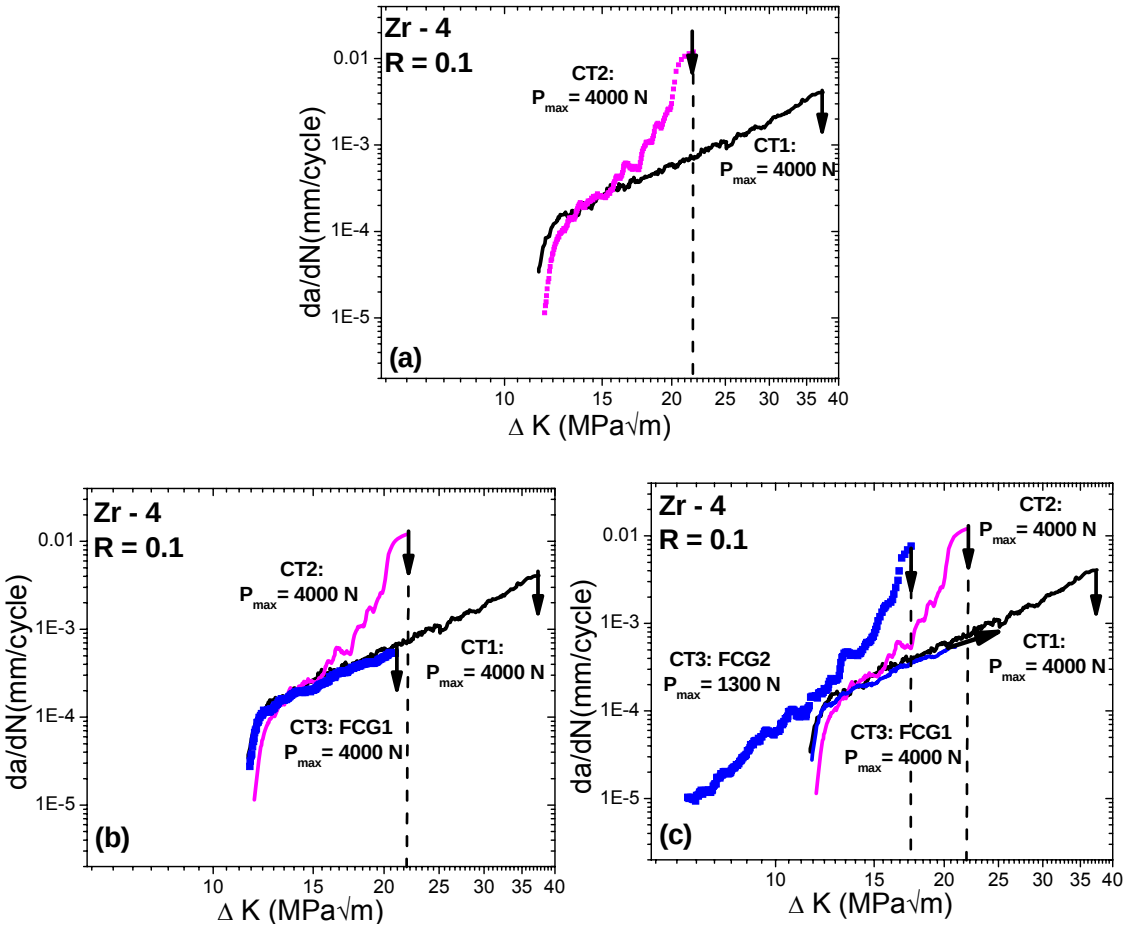

Figure 3.14 Fatigue behavior for the three cases CT 1 - 3: crack propagation rate (da/dN) vs. stress intensity factor range (ΔK) for (a) CT 1 and CT 2, (b) for CT 1, CT 2, and CT 3 FCG1. Note that at the end of FCG 1 and after H charging, CT 3 failed during the first cycle under P_{max} = 4,000 N and in (c) is shown the FCG 2 for CT 3 obtained after H charging with P_{max} = 1,300 N. The arrows in a – c) indicate the failure of the specimen.

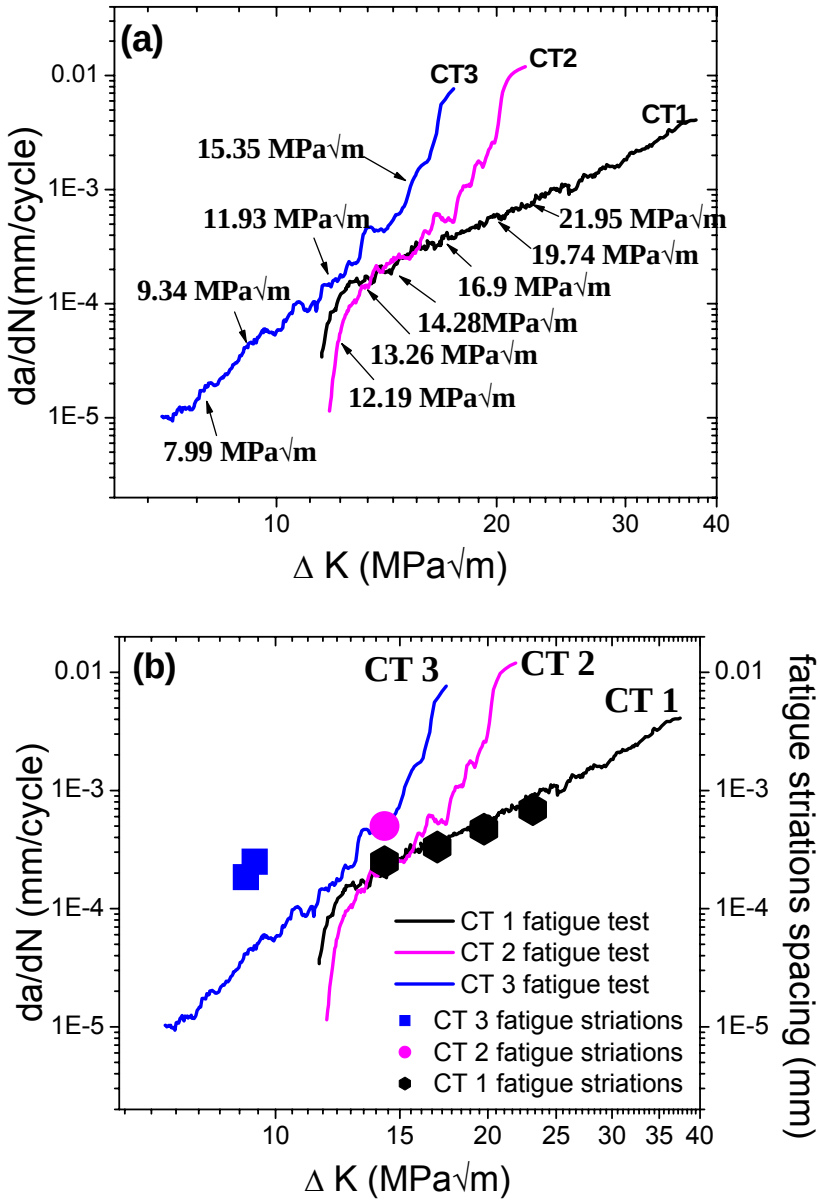

Figure 3.15 Fatigue behavior profiles for the three cases studied, CT 1-3 showing (a) the values for stress intensity factor range ΔK in MPa√m, at which SEM fractographs have been collected, and (b) comparison between the striations spacing observed with SEM (symbols) and crack propagation rate (da/dN) obtained during the fatigue crack growth test (lines). Note that black rhombs are used for CT 1 specimen, magenta dot for CT 2 specimen, and blue squares for CT 3 specimen.

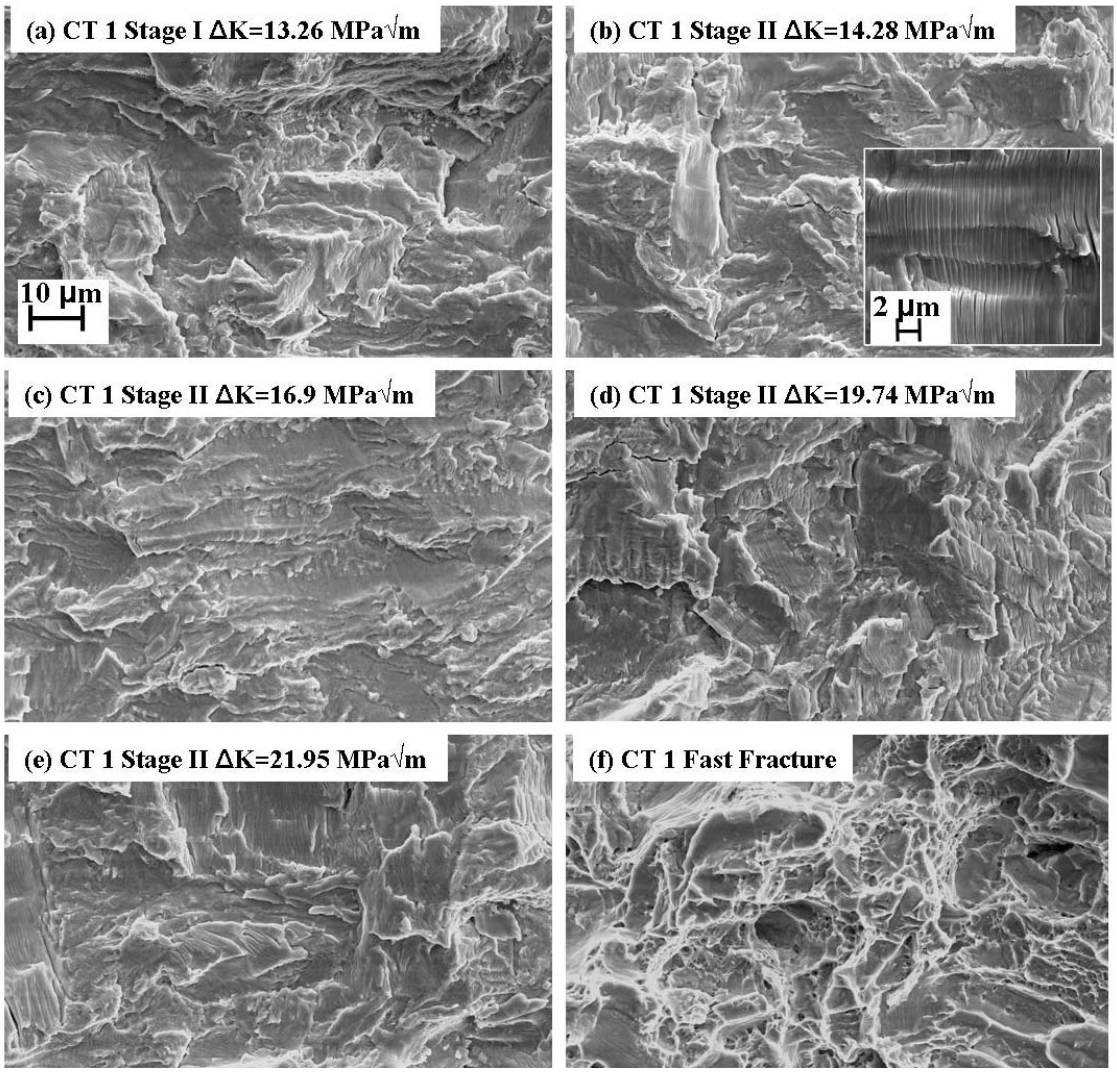

Figure 3.16 SEM fractographs for the CT 1 specimen. Images are taken at different ΔK values corresponding to different stages of the crack growth, as indicated in Fig. 6(a). (a) stage I, (b-e) stage II, and (f) fast fracture surface. An example of the fatigue striations is shown in the inset of (b).

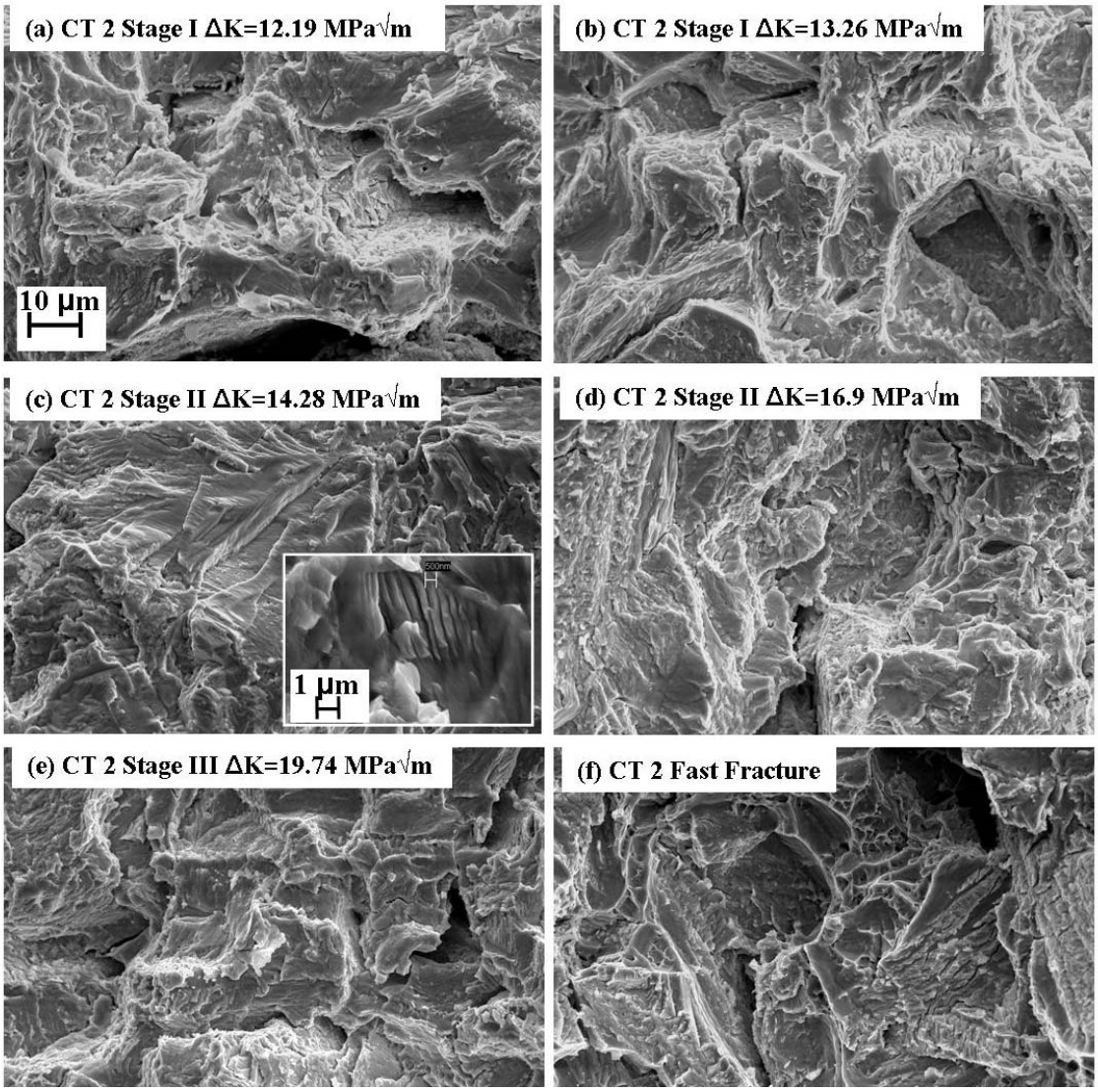

Figure 3.17 SEM fractographs for the CT 2 specimen. Images are taken at different ΔK values corresponding to different stages of the crack growth, as indicated in Fig. 6(a). (a) and (b) stage I, (c) and (d) stage II, (e) stage III, and (f) fast fracture surface. An example of the fatigue striations is shown in the inset of (c).

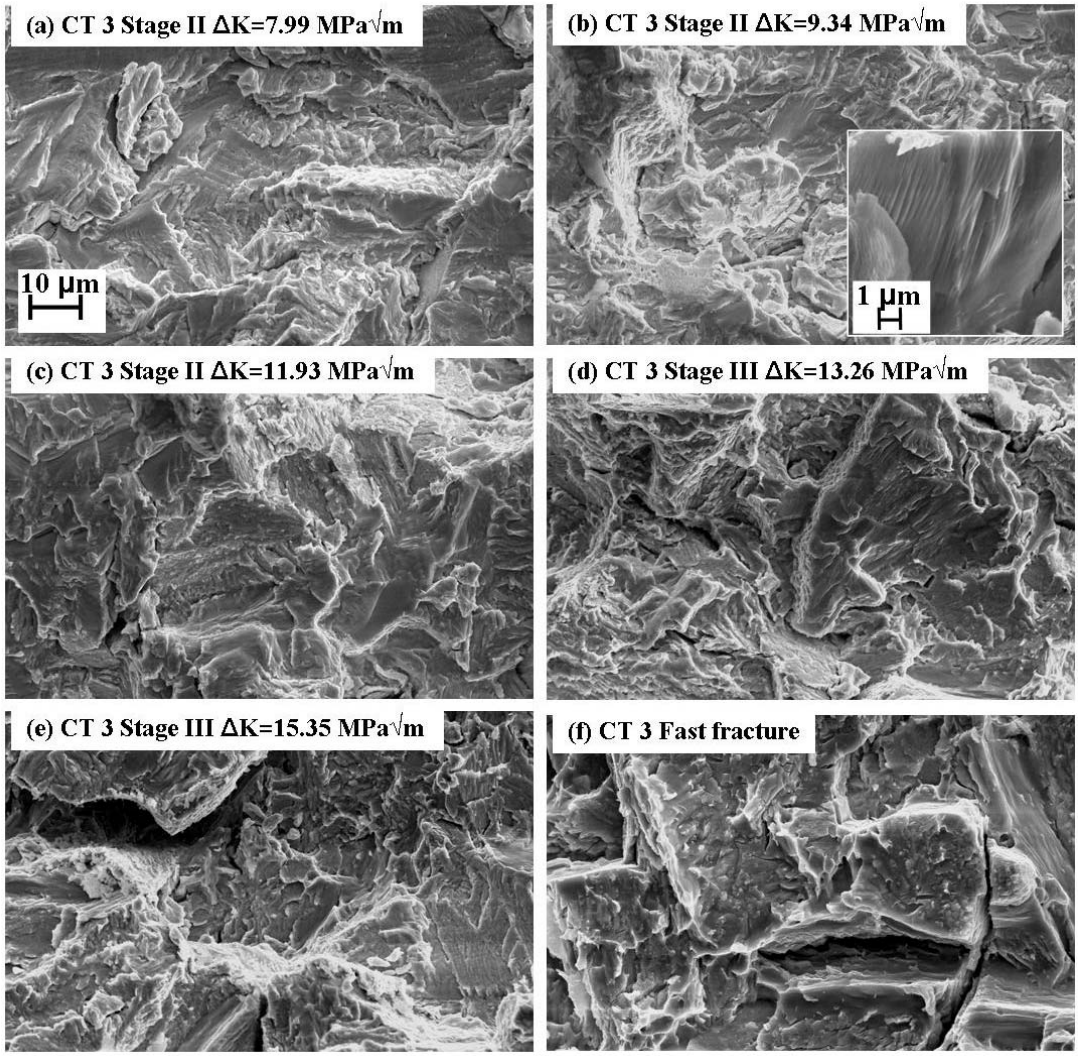

Figure 3.18 SEM fractographs for the CT 3 specimen after the H charging (FCG 2 in Fig. 1 (d)). Images are taken at different ΔK values corresponding to different stages of the crack growth, as indicated in Fig. 6(a). (a-c) stage II, (d) and (e) stage III, and (f) fast fracture surface. An example of the fatigue striations is shown in the inset of (b).

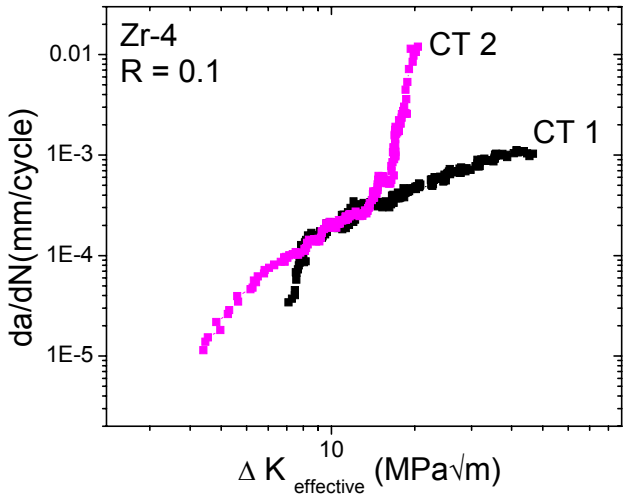

Figure 3.19 Crack propagation rates, da/dN as a function of the stress intensity factor effective, $\Delta K_{effective}$, $\Delta K_{effective} = K_{max} - K_{closure}$ for both specimens CT 1 and CT 2, showing the crack closure effect.

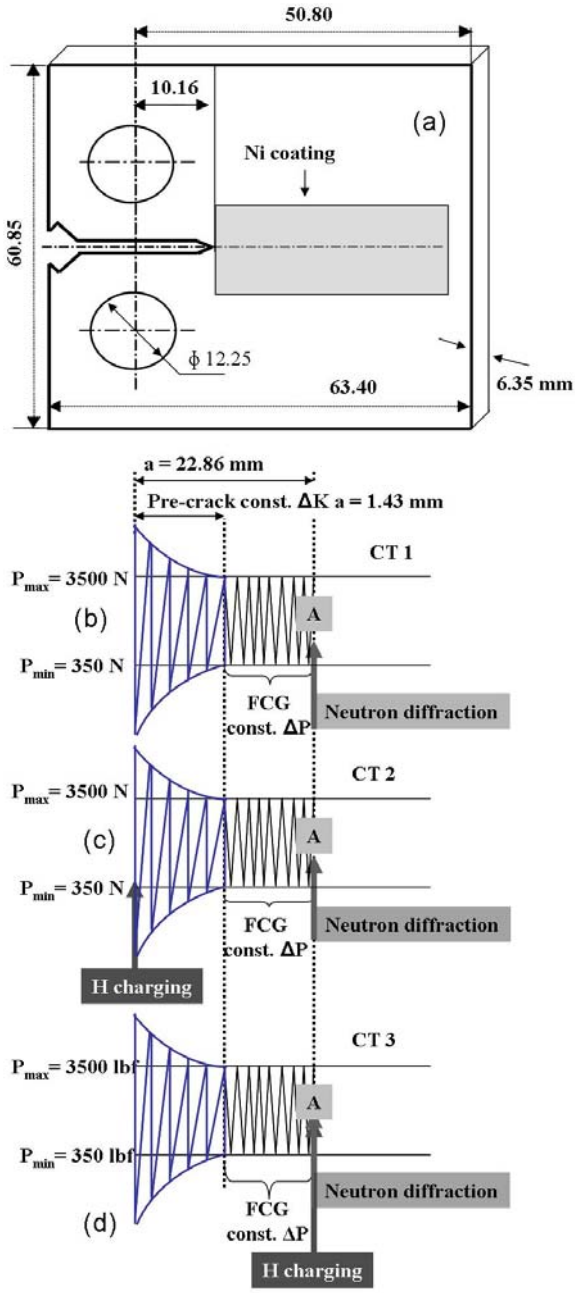

Figure 3.20 The fatigue pre-cracking, crack growth, and hydrogen charging steps before the neutron diffraction experiment, for the three cases studied, at a = 22.86 mm and P_{max} = 3,500 N. (a) Schematic of the CT specimen, dimensions in millimeters; (b) CT 1: fatigued of the as-received specimen. FCG denotes fatigue crack growth; (c) CT 2: hydrogen charged and fatigued, and (d) CT 3: fatigued and hydrogen charged.

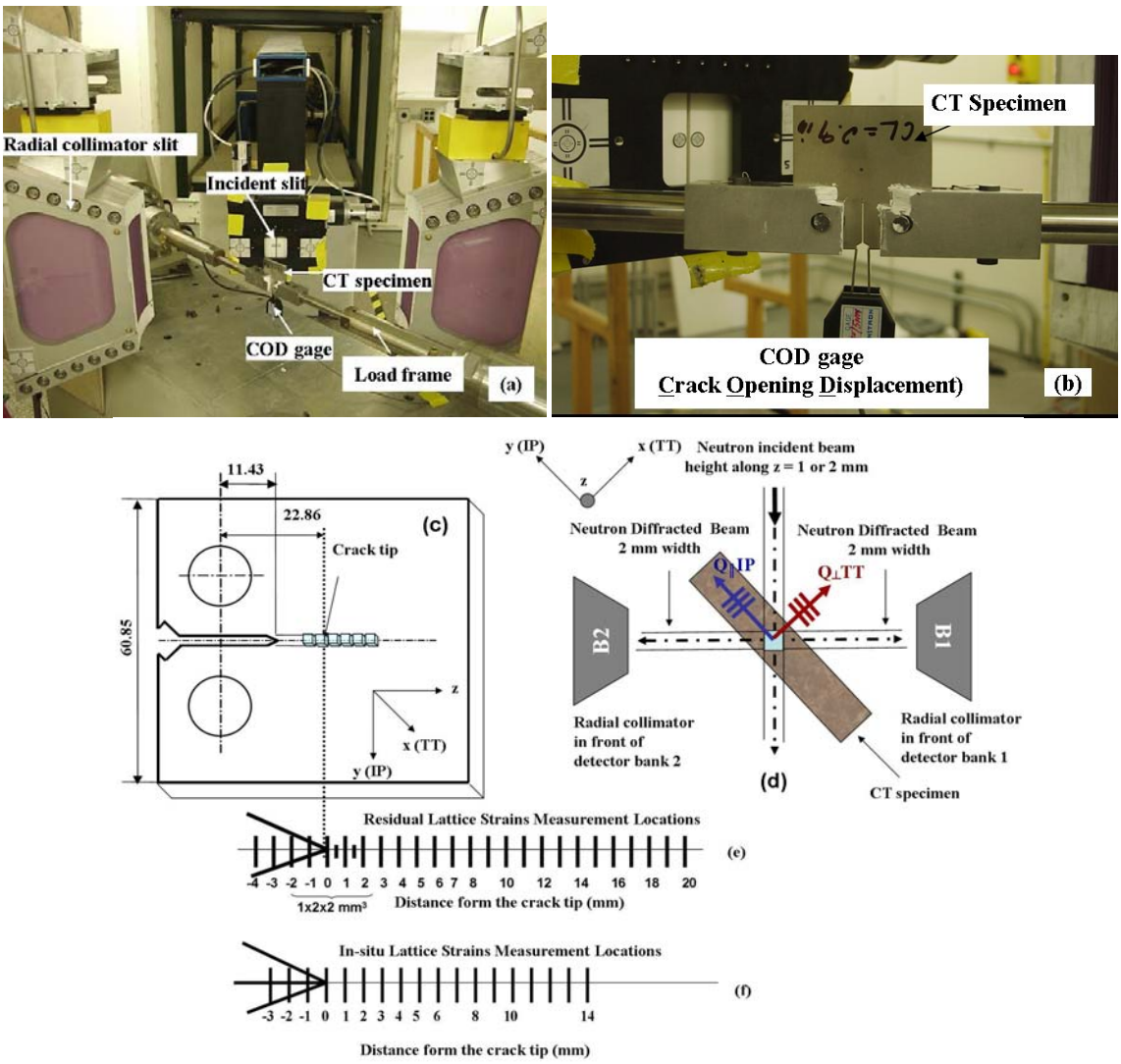

Figure 3.21 Strain measurement at SMARTS instrument, (a) picture of the specimen in front of the neutron beam; (b) picture of the CT specimen mounted in the load frame, (c) schematic of the CT and dimensions including the fatigue crack length a = 22.86 mm.(d) Top view of the neutron diffraction (ND) measurement setup. The 1 and 2 detector banks record the signal from the families of grains with their normals perpendicular (TT or x) and parallel (IP or y) to the loading direction. Scale indicates the positions where ND data were collected for spatially-resolved (e) residual strain measurements and (f) in-situ lattice strain measurements.

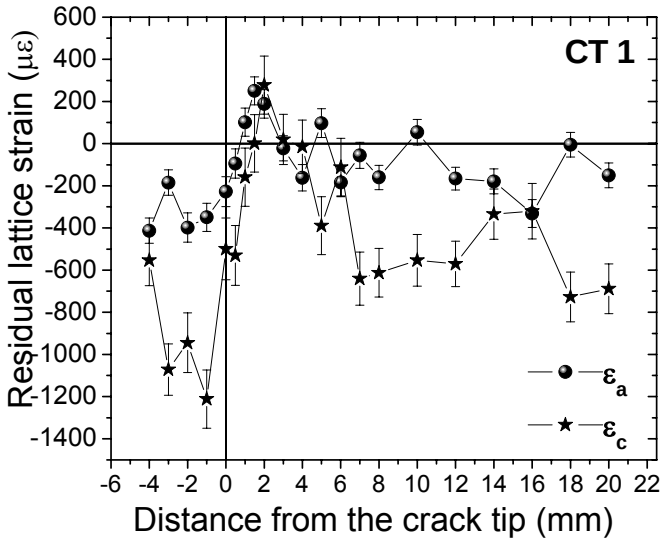

Figure 3.22 Zirconium residual lattice strain, ε_a ε_c, in the as-received condition, CT 1, with a = 22.86 mm. Both *a* and *c* axes exhibit a maximum tensile in front of the tip. The neutron diffraction lattice strain measurements were conducted from 4 mm behind the crack tip to 20 mm in front of the tip.

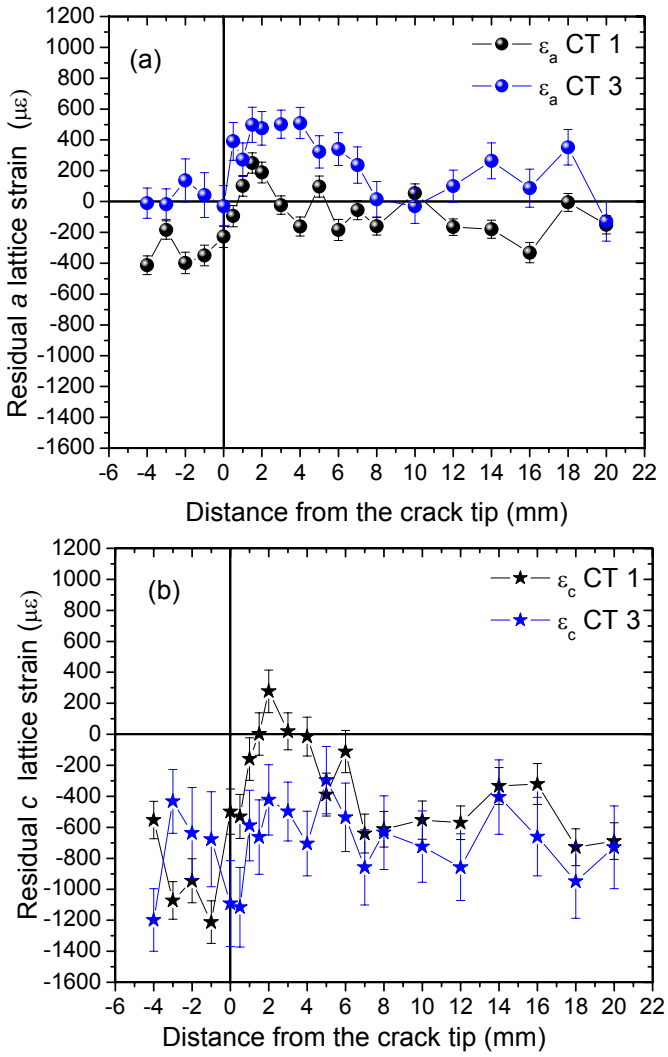

Figure 3.23 Zirconium residual lattice strain profiles, ε_a and ε_c, around the fatigue crack tip for CT 1 (as-fatigued) and CT 3 (fatigued and H charged) specimens.

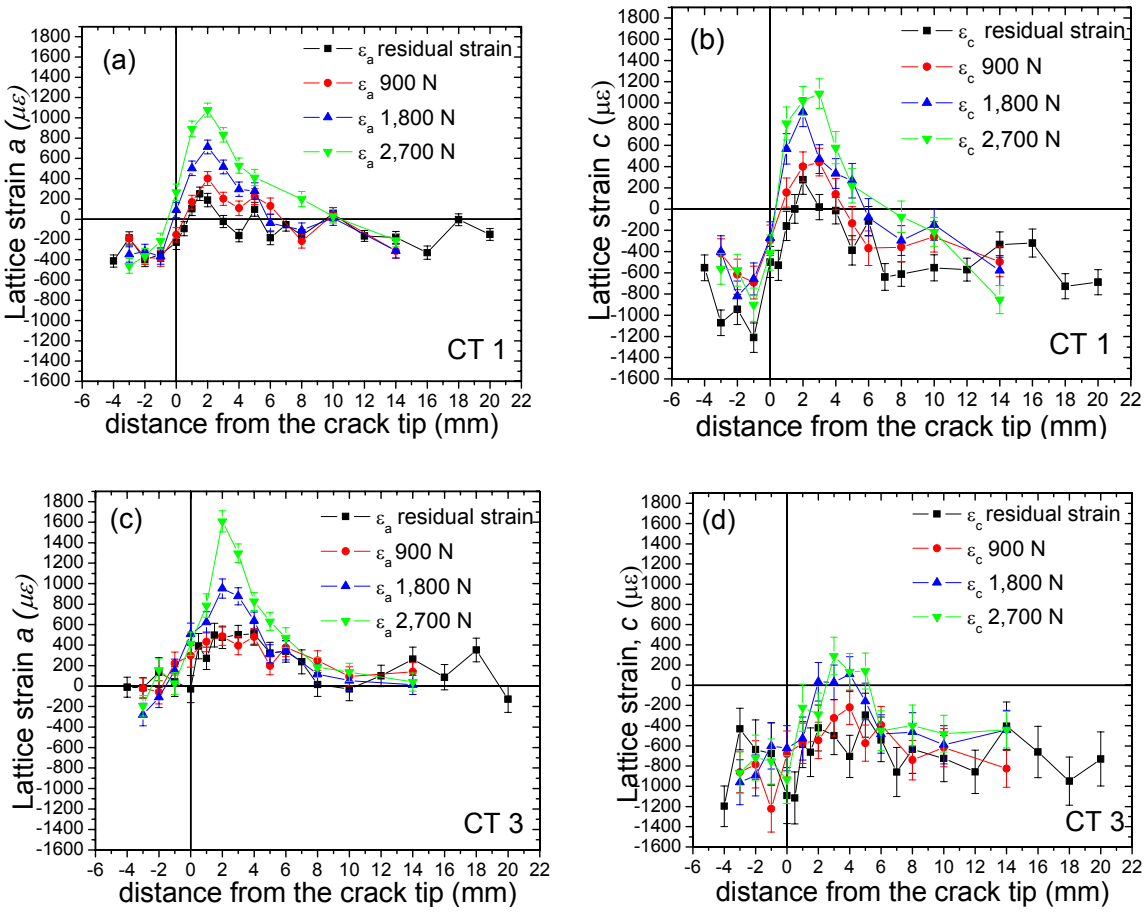

Figure 3.24 In-situ *a* and *c* lattice strains evolution around the fatigue crack under the applied loads of 900, 1,800, and 2,700 N, for the three cases CT1-3: (a-b) CT 1, (c-d) CT 3; and

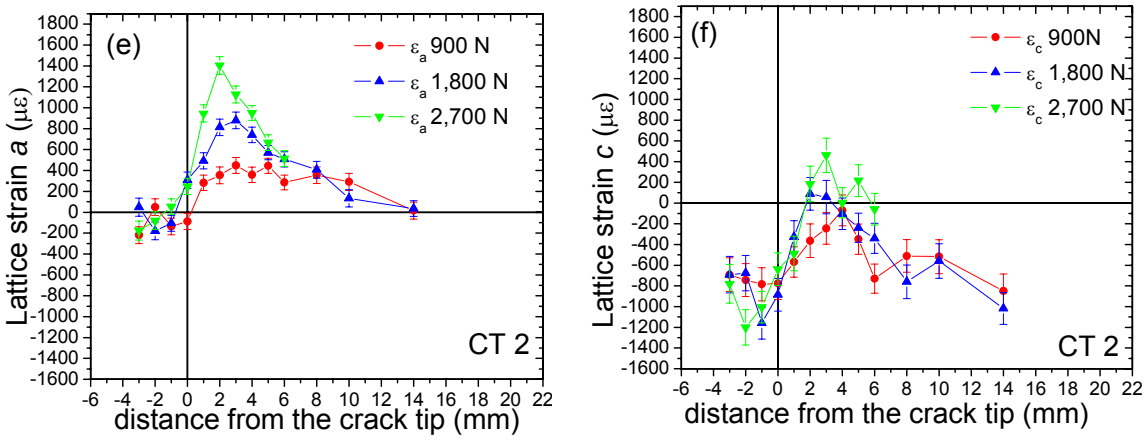

Figure 3.24 (Continued) (e-f) In-situ *a* and *c* lattice strains evolution around the fatigue crack under the applied loads of 900, 1,800, and 2,700 N, for the CT 2. Note that there is no residual strain data available for CT 2, due to the limitation in the neutron beam time allocated through the SMARTS user program.

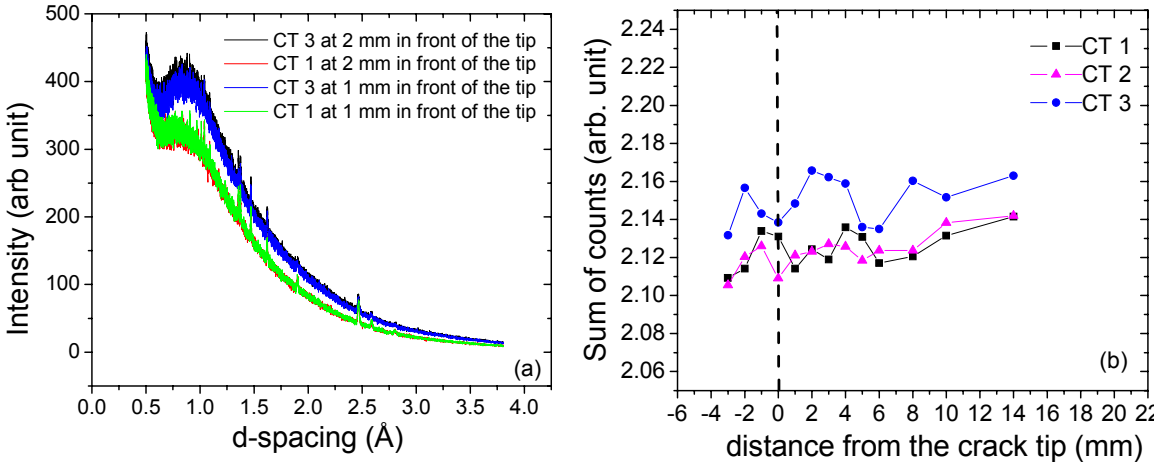

Figure 3.25 Background intensity variations from incoherent scattering (a) examples of neutron diffraction patterns obtained at the middle of the specimens' thickness of CT 1 and CT 3. These patterns were measured at 1 and 2 mm in front of the crack tip. b) Variation in background intensity along the crack, obtained by normalized sum of counts of the diffraction pattern at each measurement position. All the three cases, CT 1-3, are shown.

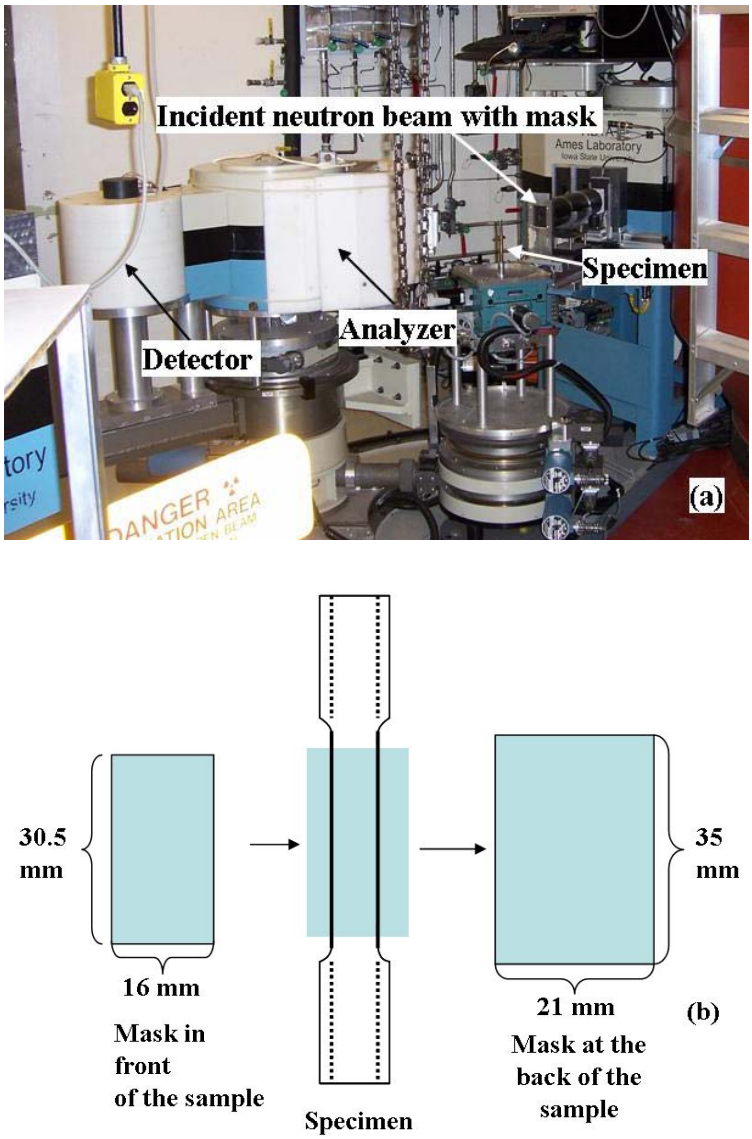

Figure 3.26 Setup of the incoherent neutron scattering measurements using HB1A instrument (a) picture of the specimen with polypropylene film in front of the beam and (b) schematic indicating the masks used in front and back of to sample to define the sampling volume.

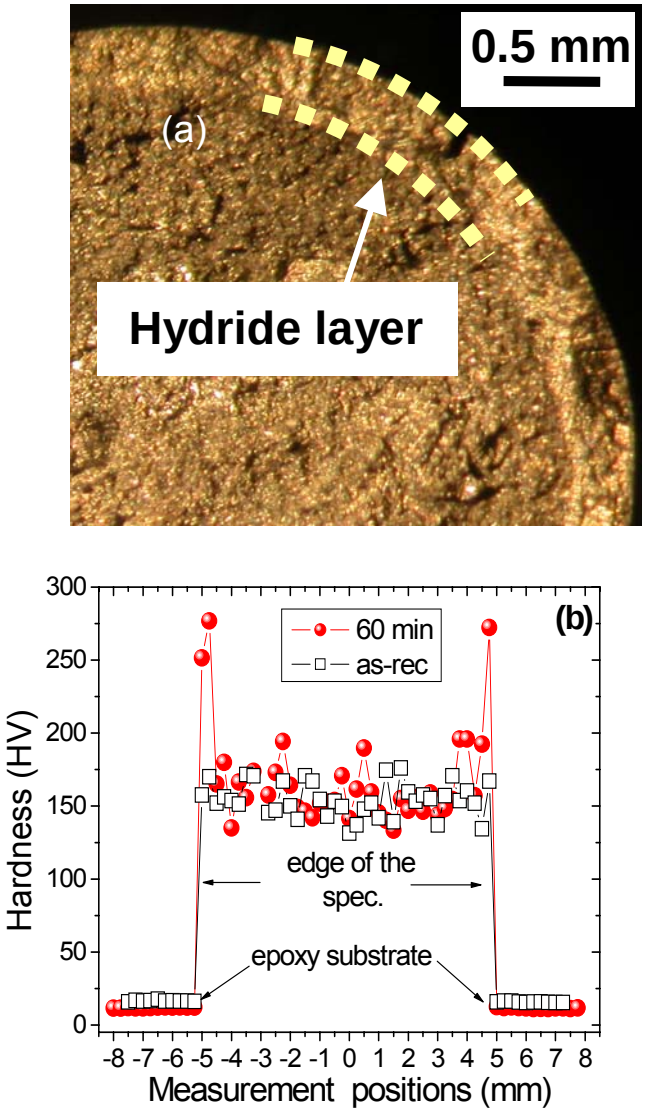

Figure 3.27 Zr-4 specimen, charged with H gas for 60 minutes at 703 K. (a) A cross-sectional fracture surface (quadrant) showing a "hydride" layer. (b) Hardness profile measured along the diameter of the hydrogenated sample in comparison to the as-received condition (no hydrogen), showing a sharp increase near its edge, due to the presence of the "hydride layer".

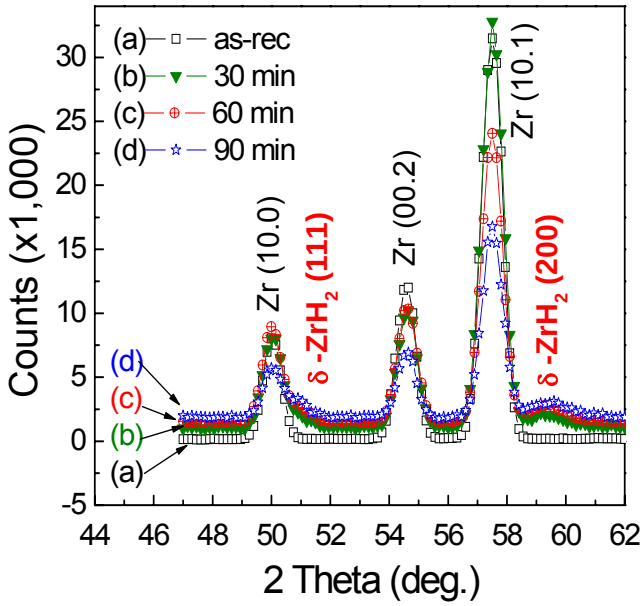

Figure 3.28 Neutron diffraction profiles of the as-received Zr-4 specimen and the specimens charged with H for 30, 60, and 90 min. at 703 K, showing a systematic increase in the overall background, increase in the δ-ZrH_2 peak intensities, and corresponding decrease in the Zr peak intensities with an increase in the charging time.

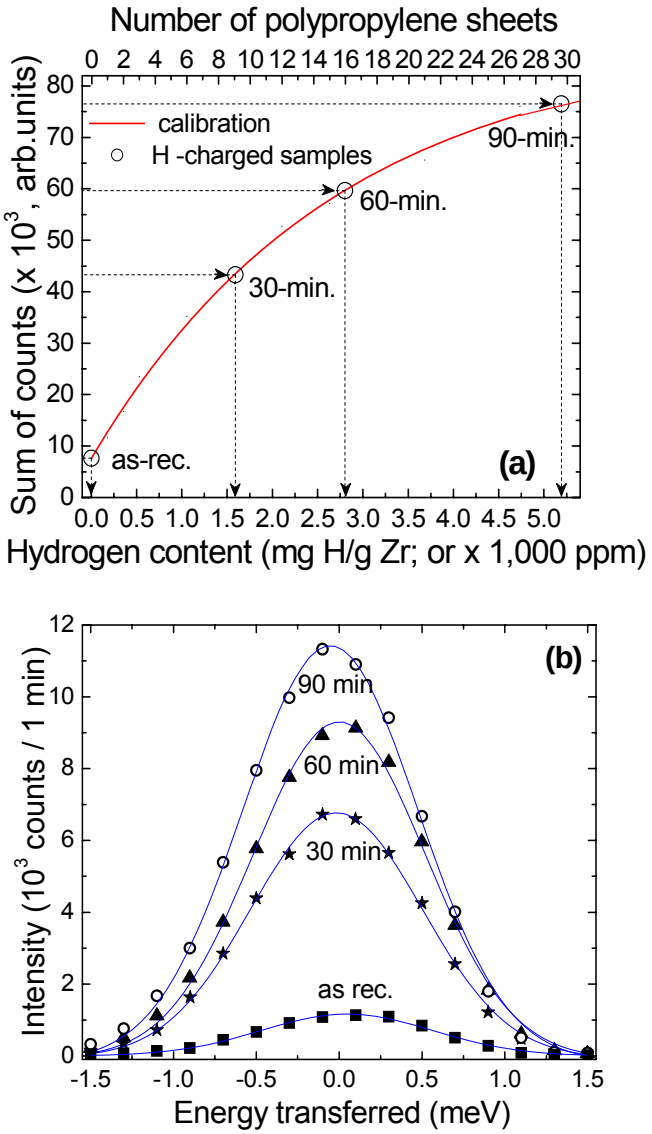

Figure 3.29 Neutron incoherent scattering of the calibration specimens and specimens charged with hydrogen gas for the estimation of total hydrogen content. (a) The solid (red) curve shows the fit to the measured sum of neutron counts from the calibration specimens. The data points (open circle) mark the sum of neutron counts measured from the Zr-4 specimens charged with hydrogen. (b) Energy scans around the zero-energy transfer showing the increase in the incoherent scattering from the hydrogenated specimens with the increase in the hydrogen gas-charging time.

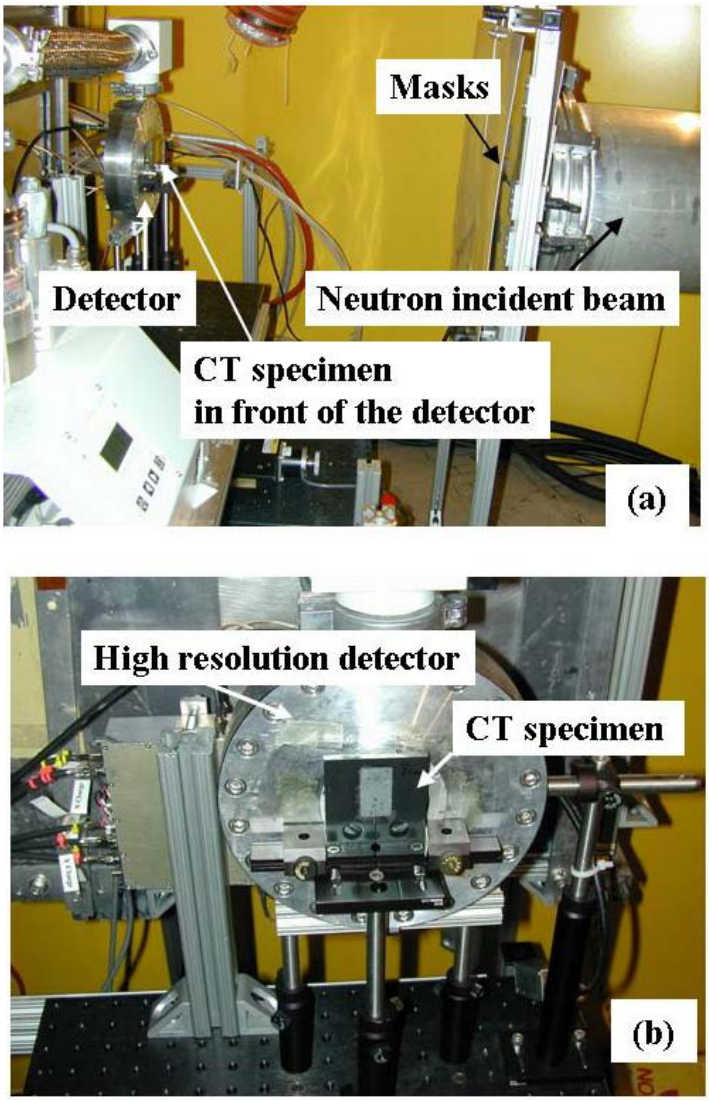

Figure 3.30 Neutron imaging experiment using Neutron Imaging Facility: (a) setup showing the CT specimen between the neutron incident beam and detector and (b) specimen in front of the high-resolution detector;

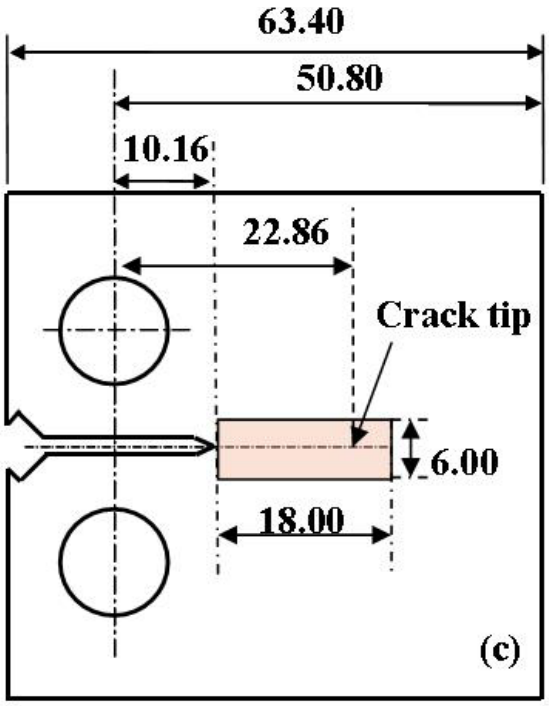

Figure 3.30 (Continued) (c) marked region indicates the area imaged by high-resolution detector. All dimensions are in millimeters.

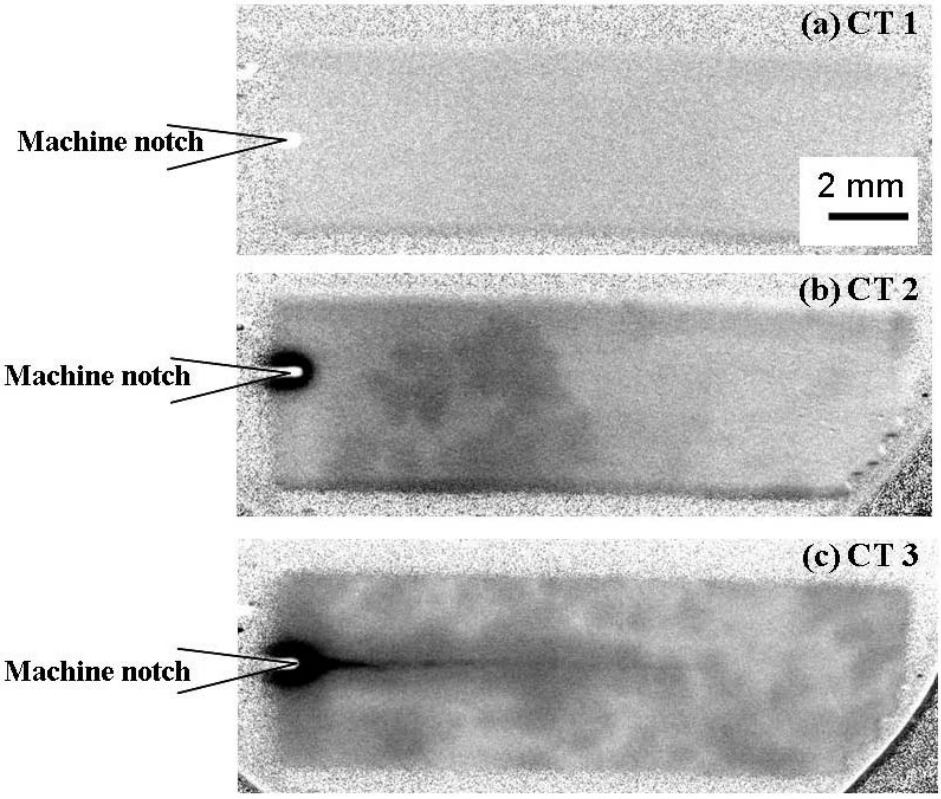

Figure 3.31 High-resolution neutron radiography for the three cases studied, CT 1-3. The area imaged is from the bottom of the notch along the fatigue crack, as indicated in Fig. 3. 30(c).

CHAPTER 4

SUMMARY AND CONCLUSIONS

4. SUMMARY AND CONCLUSIONS

There are several conclusions drawn from the present investigation.

The starting Zircaloy-4 (Zr-4) alloy, in as-received condition, has a Basketweave Widmanstätten type structure, which forms when the alloy is cooled from the β-phase (bcc, 998 ˚C) to α-phase (hcp, room temperature). The former β grains have a mean diameter of approximately 700 μm, and include α-Zr plates with different orientations. The alloy exhibits an initial random texture. Moreover, Zr-4 shows high elastic-plastic anisotropy, which leads to significant residual strains along different crystallographic orientations, in both axial and transverse directions.

A cylindrical tensile specimen of Zr-4 alloy, with coarse-grained and initial random texture, was employed in the study of deformation systems responsible for the polycrystalline plasticity at the grain level. In-situ neutron diffraction was used to measure the macroscopic behavior and the evolution of intergranular strains. Six hkil planes were shown, representing two prism, the basal, and three pyramidal planes. However, signals from many more families of grains were obtained. The experimental data was simulated using a new elasto-plastic self-consistent (EPSC) modeling scheme, which accounts for the anisotropic thermal, elastic-plastic properties of the constituent grains, and for the first time activation, reorientation, and the stress relaxation associated with twining and texture development. The model showed a good agreement with the experiment when a combination of slip systems, such as prism, basal, pyramidal <a>, and first and second order pyramidal <c+a> are activated.

However, the measured texture, developed after the tensile loading, suggested the occurrence of a lattice rotation of about 82 degrees, which in general is associated with tensile twinning. Therefore, we investigated the possibility of deformation by tensile twining, in addition to the slip systems. Two scenarios were considered in the model, and the combination of lattice strain evolution and texture developed were studied. In particular, if a 3% final volume fraction of twining was considered in the epsc calculation, a good agreement with the experiment was obtained for the lattice strain evolution. However, the predicted texture at the end of the test did not show any high-density localization of poles. Later, the contribution of twining was increased to 12 % final volume fraction, and the predicted texture was comparable to the measured texture after deformation with few exceptions. This agreement in texture, however, was significant detrimental to the lattice strain evolution. Therefore, it is concluded that twining does not play a major role on the plastic deformation of this Zr-4 under the current conditions. In addition, the corresponding critical resolve shear stresses and hardening coefficients were identified for each deformation system, and reported.

Furthermore, the hydride phase formation and its influence on microstructure and fatigue behavior of the Zr-4 alloy were investigated using compact tension specimens. Three different cases were studied, specifically the as-received condition (no hydrogen), CT 1, and two hydrogen-charged conditions, CT 2 and CT 3. It was observed that the specimen in the as-received condition, CT 1, which was fatigued to failure, has ductile behavior, and the crack propagation remains stable until failure occurred.

When charged with hydrogen gas at elevated temperature, the Zircaloy forms delta Zirconium hydrides, δ- ZrH_2, at the boundaries of α-Zr plates, which is also the path

of the fracture for the main crack. For CT 2 condition, the specimen charged with hydrogen and fatigued to failure exhibited a homogenous distribution of hydrides in the bulk, reduced toughness, reduced ductility, and increase in the crack propagation rates. In the case of CT 3, the specimen was first fatigued and then charged with hydrogen. It was observed that the presence of a gradient in the residual lattice strain evolution at the crack tip, prior to hydrogen charging, plays a critical role on the hydrogen diffusion, and thus on the hydride formation. The hydrides concentration is higher at the crack, leading to a more severe influence on the fatigue properties. The residual lattice strain profiles around the crack tip were measured using neutron diffraction. Then the compact tension specimens, in as-received condition and charged with hydrogen, were tested by in-situ monotonic loading and neutron diffraction strain measurement. The trends for the lattice strain evolution around the crack tip were observed when the applied load was increased from 900 N to 1,800 N and to 2,700 N.

In addition, during the strain measurement, an increase in the background of the neutron diffraction patterns was observed, which is due the incoherent scattering of hydrogen. This phenomenon allows the quantification of the hydrogen content in the specimen. Using incoherent neutron scattering, it was determined that a 30-minute round bar hydrogen charged specimen contains 1,600 ppm hydrogen and 1-hour charged specimen has 2,800 ppm hydrogen. The distribution of hydride around the crack could also be visualized using neutron imaging.

Therefore, the focus of this work relates to the combined effect of the applied stress, lattice strain, hydride formation and distribution around a crack tip, and fatigue

behavior. These are important issues in predicting the life of structural components operating in corrosive environments, in the fossil and the nuclear energy industry.

CHAPTER 5

ON-GOING / FUTURE WORK

5. ON-GOING / FUTURE WORK

5. 1 Kinetic Studies of Hydride Formation

Continued work on the Zr-4/Hydrogen system should be undertaken to further investigate the kinetics of hydride formation. Also, effort should be made to study the effect of the applied stress and hydrogen charging on the Zirconium lattice strain, and the resulting damage evolution. A set of in-situ neutron diffraction measurements were proposed, using the SMARTS instrument at Los Alamos National Laboratory, to understand the kinetics of hydride formation under applied loads. Table 5.1 shows the specimen matrix for each load and temperature proposed for the *in-situ* experiment. It is challenging to perform mapping on a Compact tension specimen with load frame and vacuum furnace simultaneously. Therefore, preliminary studies will be performed on cylindrical tensile or compression specimens, with a notch and controlled fatigue pre-crack in the middle of the gauge length for in-situ loading, under hydrogen charging. To produce the in-situ hydrogen charged sample, H_2 (or D_2) gas at 414°C will be run through the SMARTS furnace for 30 minute, followed by 5 hours annealing. During this process, using in-situ neutron diffraction, the formation of the hydride phase on pre-cracked region of the tensile bar will be monitored as a function of time. In more detail, the experiment will involve time-resolved neutron-diffraction measurements on each fatigue pre-cracked specimen (with no applied load or minimum load required to hold the specimen in place), while in-situ hydrogen charging is employed. A minimum of 22 measurements (every 15 min or less) will be made, with a sampling volume of 3x3x3 mm^3 in the middle of the specimen thickness. The 330 min. segment (charging plus

annealing) starts when the temperature had been reached, and the hydrogen flow is turned on. Moreover, a slow cooling rate is important for the shape and orientation of hydrides at the crack tip. Therefore a minimum of 10 measurements will be performed during the cooling segment. Then, a fresh specimen will be mechanically loaded utilizing the SMARTS load frame, under the hydrogen flow, and similar measurements will be performed. A minimum of four different loads will be applied for a given charging condition. The above mentioned measurements will be repeated at three different charging temperatures, to study the hydride formation kinetics as functions of the applied load and temperature. The diffraction patterns will be analyzed by Rietveld analysis, using GSAS. The new phase formed, the Zr-hydride, will be monitored and quantified.

Table 5.1 In-situ neutron diffraction measurements proposed for SMARTS instrument for the Zircaloy-4 alloy showing for each test condition the sample ID.

Sample condition	Load 1 = 445 N	Load 2 = 1,100 N	Load 3 = 2,400 N	Load 4 = 3,300 N
As received	As- rec.1	As-rec. 2	As-rec. 3	As-rec. 4
In-situ H, T_1= 414°C	ST11	ST12	ST13	ST14
In-situ H, T_2 = 404°C	ST21	ST22	ST23	ST24
In-situ H, T_3 = 394°C	ST31	ST32	ST33	ST34

5.2 Deformation Mechanisms of the As-Received Zr-4

Preliminary results were obtained by performing in-situ compression tests on two Zircaloy-4 specimens. The goal is to expand the deformation mechanisms studied (Chapter 3.1) to compression behavior as well as to investigate the effect of hydrides, on the strain and texture development. One specimen was kept as reference, in as-received condition, and the second specimen was charged ex-situ with hydrogen for 1 hour, followed by 5 hours annealing. The macroscopic behavior, the engineering stress-strain curve, is shown in Fig. 5.1, for both specimens. Note that the specimen containing hydrogen fractured at approximately 4 % total strain. The elastic modulus obtained for each specimen, $E_{as\text{-}received}$ = 88 GPa, and $E_{H\text{-}charged}$ = 71 GPa, indicate that, in the presence of hydrogen, the specimen becomes more compliant. Further, using Rietveld analysis, the lattice strain evolution under the applied load was obtained. Note that, in this report only the longitudinal direction (planes normal parallel to the loading axis) is presented. Figure 5.2(a) shows the *a* and *c* lattice strains for the hcp Zr in both conditions. For the fcc delta zirconium hydride phase, δ-ZrH_2, the lattice strain evolution is also shown in Fig. 5.2(b). From the lattice strain profiles, one can obtain the microscopic elastic modulus, Table 5.2. It can be observed that the c- axis is the most compliant in the presence of hydride precipitates. In addition, from the Rietveld analysis of the diffraction data, the average volume fraction for each phase can be estimated. The neutron diffraction compression data obtained can be further associated with self-consistent models, to understand the fundamental deformation mechanisms of Zircaloy-4 alloy in the as-received condition and in the presence of hydrides.

Table 5.2 Elastic modulus (GPa) for Zr and ZrH_2, obtained from Fig. 5.2

Specimen	E_{Zr}^{a} (GPa)	E_{Zr}^{c} (GPa)	E_{ZrH_2} (GPa)
As-received	101	107	--
H-charged	88	78	90

APPENDIX

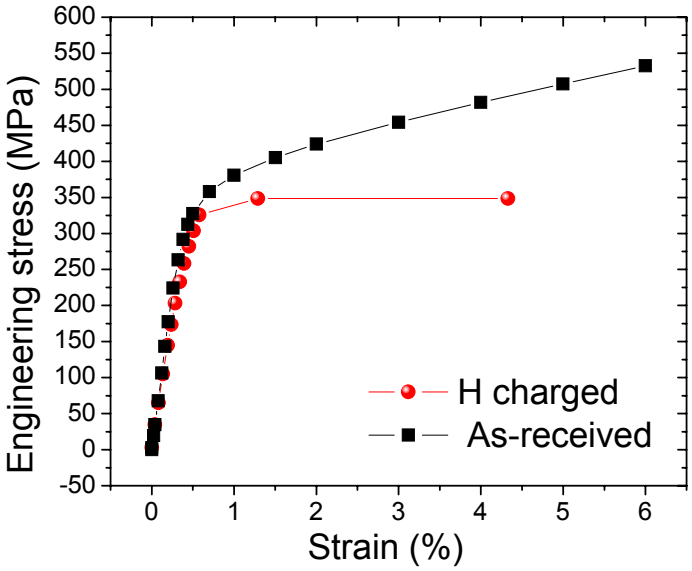

Figure 5.1 Macroscopic stress- strain curve obtained during the compression test for both cases, as-received and H charged conditions.

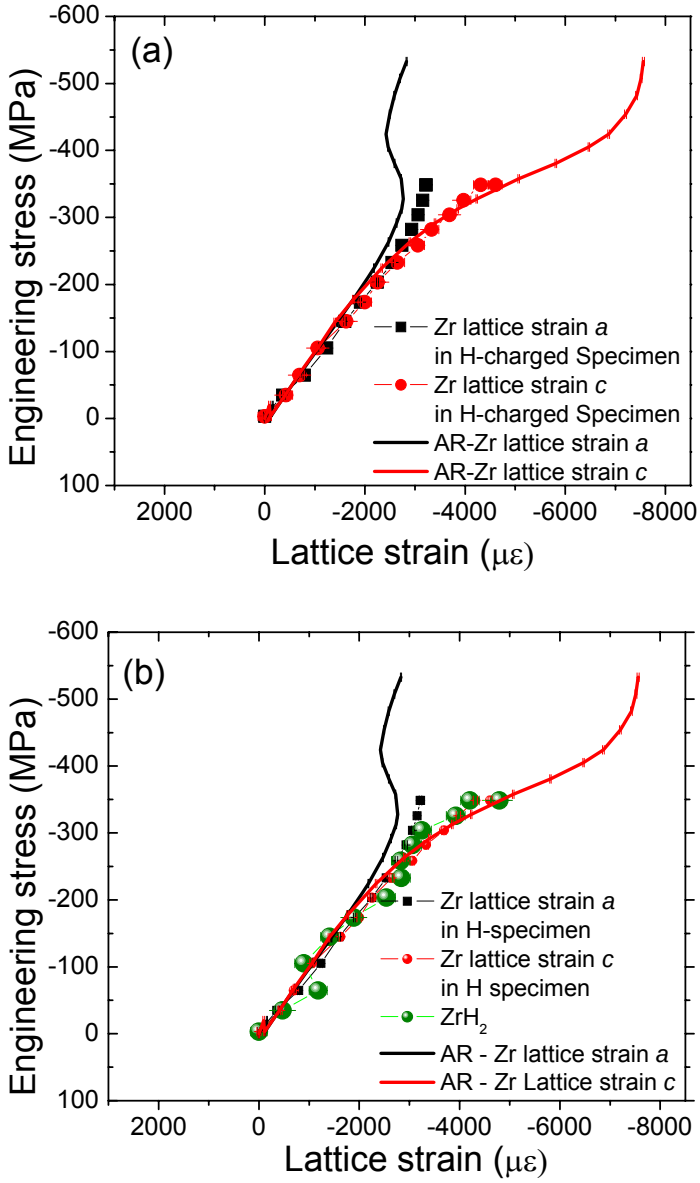

Figure 5.2 Lattice strain evolution under applied load during the compression test. (a) Lattice strain *a* and *c* for Zr in as-received condition, and hydrogen charged condition. (b) Similar with (a), also showing the lattice strain development of delta zirconium hydride, δ-ZrH_2.

VITA

Elena Garlea was born in Romania. She attended the Babes-Bolyai University, Cluj-Napoca, Romania, from July of 1993 to June of 1997, receiving a Bachelor of Science degree in Chemistry. Elena entered the Graduate Program in Materials Science and Engineering Department at The University of Tennessee in August of 2003. She received a Master of Science degree in Materials Science and Engineering in December 2005, with a GPA of 3.9/4. The Doctor of Philosophy degrees with a major in Material Science and Engineering was received in May 2008, with a GPA of 4/4.